STRUCTURAL PERFORMANCE OF LINK SLABS SUBJECTED TO MONOTONIC AND FATIGUE LOADING INCORPORATING ENGINEERED CEMENTITIOUS COMPOSITES

By:

Shirin Ghatreh Samani

Bachelor of Engineering in Civil Engineering,

Ryerson University, Toronto, Ontario, 2013

A Thesis

Presented to Ryerson University

In Partial Fulfillment of the Requirements for the

Masters of Applied Science in the Program of Civil Engineering

Toronto, Ontario, Canada, 2015

AUTHOR'S DECLARATION

I hereby declare that I am the sole author of this thesis. This is a true copy of the thesis, including any required final revisions, as accepted by my examiners.

I authorize Ryerson University to lend this thesis to other institutions or individuals for the purpose of scholarly research.

I further authorize Ryerson University to reproduce this thesis by photocopying or by other means, in total or in part, at the request of other institutions or individuals for the purpose of scholarly research.

I understand that my thesis may be made electronically available to the public.

STRUCTURAL PERFORMANCE OF LINK SLABS SUBJECTED TO MONOTONIC AND FATIGUE LOADING INCORPORATING ENGINEERED CEMENTITIOUS COMPOSITES

Shirin Ghatreh Samani, Masters of Applied Science, 2015

Department of Civil Engineering

Ryerson University, Toronto, Canada

ABSTRACT

This research presents the results of experimental investigation conducted on $1/4^{th}$ scale link slabs subjected to monotonic and fatigue loading incorporating different ECC mixtures and self-consolidating concrete (SCC). The structural performance for the link slabs are evaluated based on the load-deformation/moment-rotation responses, strain developments, cracking patterns, ductility index and energy absorption capacity. Test results of a $1/6^{th}$ scale full bridge with ECC link slab tested under monotonic loading up to service stage is also described. The experimental link slab moment resistance and its length are compared with those obtained from theoretical and design specifications. The ECC link slabs demonstrated superior performance exhibiting high residual strength and energy absorbing capacity and prolonged life (associated with enduring large number of fatigue cycles) compared to their SCC even though subjected to higher fatigue stress levels. This research confirmed the viability of ECC link slab to construct joint-free bridges satisfying serviceability and design specifications.

ACKNOWLEDGEMENTS

DEDICATIONS

To My Parents

That Sacrificed their Life for My Greatest Success

TABLE OF CONTENTS

LIST OF TABLES

LIST OF FIGURES

xiii

LIST OF SYMBOLS AND ABBREVIATIONS

A_{bar}- Steel Rebar Cross-Sectional Area

A_s –Steel Area

A_{sc} – Cross Sectional Area of one Stud

AASHTO- American Association of State Highway and Transportation Officials

B_{ls} -Width of Link Slab

CS: Crushed Sand

E_{ECC} -Modulus of Elasticity

ECC: Engineered Cementatious Composite

FA: Fly Ash

FRC-Fiber Reinforced Concrete

$f_{y\text{-steel}}$- Yielding Stress

GU- General Use

I_{ls} -Uncracked Moment of Inertia

ITZ: Interfacial Transition Zone

L_{dz}- Length of the Debond Zone

L_{ls}- Length of the Link Slab

LVDT: Linear Variable Differential Transformers

M_{ls} - Applied Moment

MAS: Maximum Aggregate Size

MOR-Modulus of Rupture

MS: Mortar Sand

PE-Polyethylene

PVA: Poly-Vinyl-Alcohol

RC-Reinforced Concrete

SS: Silica Sand

SCC: Self-Consolidating Concrete

SCM: Supplementary Cementing Material

t :Thickness

T_{steel}: Tensile Force

θ_{max} : Maximum End Rotations

$\Delta_{max-short}$:Maximum Allowable Deflection

n_ε :Yield Strain Ratio

ε_{y-ECC} :Yield Strain of ECC

$\varepsilon_{y-Steel}$:Yield Strain of Steel

ρ:Steel Reinforcing Ratio

CHAPTER ONE
INTRODUCTION

1.1 General

Many highway bridges are designed as multi-span simply supported (over piers or abutments) steel or pre-stressed concrete girders supporting concrete bridge deck. At the end of each simple span deck, a mechanical expansion joints are installed for allowing a free deformation caused by girder's deflection, shrinkage, temperature variation and creep effect (Figure 1.1a). Aside from a high installation cost of these expansion joints, constant maintenance is required due to their low durability performance. The leakage of chloride-containment water through these mechanical expansion joints leads to corrosion of the steels girders and deterioration of the substructures (Kim et al. 2004). The accumulative debris reduces the strength and functionality of the bridge structures and eventually leading to a catastrophic failure. In fact the mechanical expansion joints are a major source of bridge deterioration in Canada (Au et al. 2013).The possible approach for improving the durability performance of the bridge structures is the elimination of the mechanical expansion joints. Different design methodologies have been proposed by scholars and ministry of transportation authorities for substituting these mechanical expansion joints (Au et al. 2013; Alampalli & Yannotti, 1998; Gilani, 2001; Zia et al. 1995). The first approach is to use the haunched deck for developing a continuous deck system over the piers while keeping the girders as simply supported span. The second method is the construction of integral concept with continuity of the girders and the third approach is the implementation of the link slabs on the deck for developing a joint-free bridge deck with simply supporting spans (Figure 1.1b). The joint free-bridge deck is the most economical and efficient rehabilitation strategy in comparison to other proposed methods (Alampalli & Yannotti, 1998).

(a) Bridge deck with joint   (b) Bridge deck with link slab
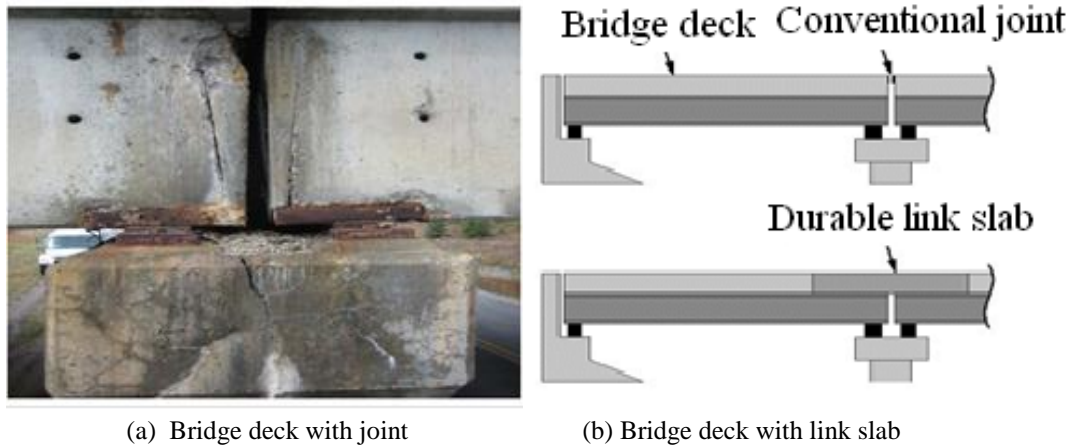
Figure 1.1: Joint Free Bridge Deck with Link Slab (Hossain & Anwar 2014)

The link slab is defined as a section of the deck connecting the two adjacent simple-span girders (Figure 1.2). The total length of the link slab consists of the debonding and transition zone. The length of the debonding zone (where all the shear connectors are removed and debonding mechanism is placed on top of the flange's girder) is limited to 5% of each adjacent bridge span. For reducing the stress concentration on the debonding zone, transition zone was introduced with additional design of 2.5% increase in length and 50% additional shear stud connectors than required by AASHTO design code (Caner & Zia, 1998; Qian et al. 2009). Caner and Zia (1998) experimentally analyzed the performance of the joint-free bridge decks and proposed a design method for the normal concrete link slab.
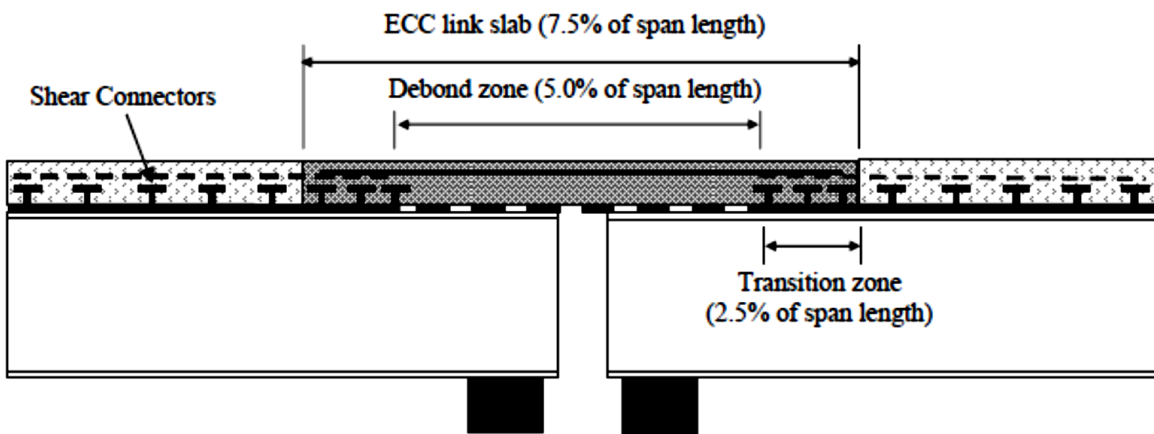
Figure 1.2: Schematic of Link Slab showing Components

Although the use of link slab improved the durability performance of the bridge deck to some extent, but development of large tensile cracks in link slab segment for normal concrete caused degradation of structural (Caner & Zia, 1998). These cracks, similarly to the expansion joints, allow salt water to contact the steel girder and rebar, causing corrosion and eventually leading to structural failure.

Engineered cementitious composite (ECC) is a special type of high performance fiber reinforced concrete that offers significant potential for resolving the durability performance of reinforced and pre-stressed concrete structures (Li & Kanda, 1998; Li et al. 2002; Li, 2003). The high strain hardening characteristic and multiple micro-cracking behavior under tension and flexure while minimizing the amount of the reinforcing fibers (less than 2% by volume) makes it an ideal material for the link slab application (Sahmaran et al. 2010; Fischer & Li, 2003). Comprehensive research studies have been conduct on material properties of the ECC by incorporating different supplementary cementitious material and sand aggregates (Sahmaran et al. 2010, Hossain & Anwar, 2014; Sherir, 2012). ECC mixtures have been developed by incorporating industrial by-products/natural pozzolans such as fly ash, slag and metakaolin as replacement of cement (up to 60%) as well as fibers of different types and configurations. Introduction of such supplementary cementitious materials has an inevitable influence on the microstructure of matrix and interface, and in turn on the micromechanical properties governing the fiber bridging behavior and cracking behavior of green ECCs. The presence of SCM, in fact, leads to improved strain-hardening behavior and durability of ECC. Tensile strain capacity exceeding 5% has been demonstrated on ECC materials reinforced with polyethylene and polyvinyl alcohol fibers. ECC strain hardens after first cracking, similar to a ductile metal, and demonstrates a strain capacity 300 to 500 times greater than normal concrete. Even at large imposed deformation, crack widths of ECC remain small (less than 60 μm). Although ECC performance under monotonic loading has investigated to date, limited research has been conducted on its flexural fatigue performance (Sherir, 2012; Suthiwarapirak et al. 2004). Repetitive fatigue loading (normal to bridge structures) could result in the deterioration in the flexible ECC link slab used for construction of joint-free bridge decks. There is a lack of research studies on the structural performance of link slabs made of green cost-effective ECC mixtures subjected to monotonic and fatigue loadings for the development of design guidelines/specifications.

1.2 Research Significance

The rehabilitation of the bridge structure is a major concern for reinforced and pre-stressed concrete structures due to accelerating deterioration with increasing traffic volumes, stress levels, environmental and time-dependent damages. Further, as the bridge structure ages, the rehabilitation cost increases even though billions of dollars are already spent every year in the USA and Canada for bridge repair and maintenance. The decreasing budget allocations and increasing need for bridge rehabilitation specifically in Canada due to poor durability performance of bridge structure are becoming a major problem for highway transportation authorities.

The leaking expansion joints are a major source of multi-span bridge deteriorations in North America. For reducing the pre-mature deterioration, the expansion joints can be replaced by flexible ECC link slabs forming a joint free bridge decks (Kim et al. 2004). The high strain hardening characteristic and multiple micro-cracking behavior of ECC can improve the durability and extends the service life of the bridge decks (Keoleian et al. 2005, Hossain & Anwar, 2014).

During the past few years at Ryerson University, the locally available aggregates and supplementary cementitious material (SCM) have been incorporated for the production of sustainable and cost effective ECC mixes for structural applications (Shamaran et al. 2010, Sherir, 2012, Maulin, 2012; Hossain & Anwar, 2014). The use of ECC link slab has been a new emerging technology, however limited research has been conducted on its flexural monotonic and fatigue performance. The lack of research studies specifically in Canada requires a detailed investigation on link slabs subjected to flexural monotonic and fatigue loading using greener ECC mixes to understand structural behaviour and to develop design guidelines and specifications. The findings of this research will surely benefit engineers, builders and local authorities when designing and constructing joint-free bridges with ECC link slabs.

1.3 Research Objectives and Scopes

The main objectives of this research program are to:

- Evaluate the structural performance of model link slab specimens of $1/4^{th}$ scale by conducting tests under flexural monotonic loading (to failure) by incorporating seven different ECC mixes incorporating different types/content of fly ash (FA) namely CI and F and size/type of sand aggregates (such as silica (SS), crushed (CS) and mortar sand (MS)) through the load-deformation/moment-rotation responses, stiffness, strain developments, crack characterization, crack width, energy absorbing capacity and ductility. Study the performance of ECC link slabs compared to their self-consolidating concrete (SCC) (considered in this investigation as normal concrete made with coarse and fine aggregates) counterparts under monotonic loading based on the above criteria. Evaluate also the influence of various ECC mixtures and SCC on link slab performance.

- Study the structural response of link slabs made of a selected high performance ECC mixture (using class CI fly ash and local mortar sand) subjected to flexural fatigue loading by conducting tests based on two different approaches: applying two different fatigue stress levels (40% ± 20%, 55%±20%) at a fixed fatigue cycles of 400000 and applying different fatigue cycles of up to 1 million at a fixed stress level of 40% ± 20%. Conduct flexural fatigue tests on $1/4^{th}$ scale link slabs in three different stages under pre-fatigue monotonic, fatigue and post-fatigue monotonic loading. Study the fatigue performance of ECC link slabs for both approaches (variable fatigue stress levels and number cycles) compared to their SCC counterparts based on load-deformation responses, strain developments, crack characterization, energy absorbing capacity, ductility index and stiffness. Evaluate the post-fatigue resistance of ECC link slabs (compared to their SCC counterparts) based on residual strength, stiffness, ductility, energy absorbing capacity and crack development and crack width characteristics.

- Compare the experimentally obtained moment resistance of link slab to those obtained from theoretical analyses. Also compare experimental link slab rotation to those prescribed by previous researchers and design specifications.

- Conduct test on 1/6th scale full bridge with ECC link slab tested under monotonic loading (up to service load) to demonstrate the link slab performance in actual joint-free bridge consisting of two simply supported adjacent spans based on load-deflection/moment-rotation response and strain development as well as inflection point identification. Compare experimentally obtained location of inflection points and girder rotation compared with those suggested by researchers and design specifications such as Lepech and Li (2009), AASHTO LRFD (2012) and CHBDC (2006).

- Make recommendations for the ECC link slab performance and development of design guidelines. Describe the viability of designing and constructing joint-free bridges with ECC link slabs.

1.4 Thesis Outline

This thesis consists of 6 chapters presenting a comprehensive investigation on the structural performance of link slabs (made of ECC and SCC) for joint-free bridge construction.

Chapter 1 introduces the link slab for the joint-free bridge deck construction, ECC materials and relevant research studies. It describes the objectives and scopes of this research.

Chapter 2 presents the comprehensive literature review on material, mix design and properties of ECC and SCC with especial reference to supplementary cementing materials, fibers and aggregates. It also describes relevant research studies on link slab, link slab structural behaviour, and available design guidelines for link slabs as well as implementation and application of link slabs in joint-free bridge decks.

Chapter 3 describes the experimental program and theoretical analysis including material properties, geometric dimensioning of scaled down link slabs and full bridge models, experimental instrumentation and testing procedures.

Chapter 4 presents the results of the experimental investigation on 1/4th scale link slab specimens subjected to monotonic loadings. The performance is described based on the load-deflection/moment-rotation response, strain developments, cracking/crack propagation, energy absorption, ductility and failure modes. The influence of seven ECC mixes and aggregate types/size on the link slab structural performance under monotonic loading is described

compared with those made with SCC. In addition, results of a test conducted on $1/6^{th}$ scale full bridge with ECC link slab tested under monotonic loading is described based on load-deflection/moment-rotation response and strain development as well as inflection point identification. Experimentally obtained location of inflection points, moment resistance and girder rotation are compared with those obtained from theoretical formulations and design specifications.

Chapter 5 presents the results of the flexural fatigue performance of the $1/4^{th}$ scale link slabs tested in three different stages under pre-fatigue monotonic, fatigue and post-fatigue monotonic loadings. The fatigue performance of link slabs is evaluated based on load-deformation responses, strain developments, crack characterization, energy absorbing capacity, ductility index and stiffness degradation. Experimental results are compared with those obtained from theoretical formulations and design specifications.

Chapter 6 summarizes the findings of the research and provides recommendation for future research studies on the link slabs.

CHAPTER TWO
LITERATURE REVIEW

2.1 Introduction

This chapter presents a literature review on the performance of link slabs used in the joint-free bridge deck construction using normal concrete and engineered cementitious composites (ECCs) subjected to monotonic and fatigue loading as well as ongoing research on the material and mechanical properties of the incorporated concretes especially ECCs.

2.2 Pervious Research on Link Slab for Joint-free Bridge Construction

Back in 1970's many bridge structures were designed as simply supported girders supporting a simply span concrete decks. A mechanical expansion joints were provided at the end of each deck spans for allowing a girders to deform freely under internal and external stresses (Lam et al. 2008). The low durability performance of mechanical expansion joints in the bridge deck led the engineers to develop an efficient design of joint-less bridge structure known as link slab (Caner &Zia, 1998). Experimental research has been conducted on developing design guidelines for durability and structural performance of link slabs using different concretes (normal concrete and ECC), varying reinforcing ratio and debonding length (Caner & Zia, 1998; Gilani, 2001; Zia et al. 1995; Maulin, 2012; Lepech & Li, 2009). Limited research has also been conducted on the fatigue performance of link slab as well its implementation and performance in a real bridge structure. Kim et al. (2004) investigated the durability performance of the traditional ECC link slab subjected to flexural fatigue loading only up to maximum allowable AASHTO's rotation of 0.00375 radian at 100000 fatigue cycles. Caner and Zia (1998) tested the performance of normal concrete link slab in reduced scale bridge structure and proposed some design guidelines.

Since the early 1980's, researchers have investigated the performance of joint-free bridge decks in a multiple simply-supported girders. Zuk (1981) analyzed the effects of expansion and contraction joints in joint-free bridge deck, but due to lack of experimental results, his model was not implemented in an actual application. Gastel and Zia (1989) developed a finite element model for joint-free bridge decks using a linear strain theory along the depth of the link slab, but once again the model was not validated due to lack of experimental results.

The first experimental investigation of the joint-free bridge deck with connecting link slab was conducted by Caner and Zia (1998). Two reduced scale bridge specimens with simply supported steel and pre-stressed girders and a connecting link slab were tested under monotonic loading. The first experimental investigation revealed that link slabs were subjected to flexural stresses under typical traffic loading rather than elongation like a mechanical expansion joints. Tensile cracks were formed on top of the link slab under service condition due to development of negative moment. It was pointed out that in addition to applied loading, additional tensile stresses were imposed on the link slab due to creep, shrinkage and temperature loading. For enhanced durability performance of link slab, they suggested to use epoxy coated reinforcement or carbon fiber reinforced polymer (FRP) bar to avoid corrosion. Further, it was proposed to reduce the stiffness of the link slab by limiting the debonding length to 5% of the adjacent bridge for maintaining the simply support performance of the girder with a continuous deck as per Equation 2.1.

$$L_{dz} = 5\%(L_1 + L_2) \tag{2.1}$$

where L_{dz} denotes the total length of the debondig zone, and L_1, L_2 are the lengths of adjacent bridge spans.

Aside limiting the length of the link slab, Caner and Zia (1998) also suggested to minimize the reinforcing ratio of the link slab based on the stress criterion (Equation 2.2) at girder's end rotation of 0.0015 radian (AASHTO, 2012) for maintaining low structural stiffness.

$$f_s < 0.4f_y \tag{2.2}$$

where f_s and f_y are denoting the allowable stress and yielding stress of the reinforcing bar.

Many problems were associated with the experiments conducted by Caner and Zia (1998). The major problem was development of large tensile crack widths on top of the link slab due to use of normal concrete. Although heavily steel reinforced link slab would have reduced the crack's width to the acceptable limits, but it would increase the stiffness of the link slabs. Weak

interfaces were formed between the concrete bridge deck and link slab joint because the applied tensile stresses were resisted only by the link slab rather than a composite actions of deck and girder. Also there was a lack of experimental and analytical results on the fatigue performance of the link slabs.

Experimental investigations were conducted on the full scale link slabs subjected to both monotonic and fatigue loading using ECC (Kim et al. 2004; Li et al. 2003; Kim & Li, 2004). Experimental results of ECC based link slabs were compared to the conventional reinforced concrete (RC) link slab. While previous research was focused on the reduced scale full bridge models using conventional RC, the new investigation focused on the full-scale link slab portion only. Therefore the imposed end rotations of the link slabs caused by adjacent bridge spans were replicated in the laboratory. The reinforcing ratio for the ECC and RC link slabs was adopted from the guidelines proposed by Caner and Zia (1998) for satisfying the stress criterion of RC link slab at the end rotation of 0.0015 radian. Monotonic and fatigue test results revealed the suitability of ECC material for the link slab application developing a low structural stiffness for allowing the hinge formation, while keeping the crack widths below the acceptable limits at the ultimate loading. The yielding of reinforcing bar was delayed in comparison to the conventional RC because of high tensile strain capacity and ductility of ECC that allowed a compatible deformation of the composite with reinforcing bar. Based on the analysis, it was suggested to reduce the amount of the steel reinforcement further for the ECC link slab to maintaining the simply supporting behaviour of the girders with lower structural stiffness. The stiffness of the ECC links slabs remained unchanged after cyclic testing at 100000 fatigue cycles. All ECC link slabs formed multiple micro-cracks (with width below 130 μm) within the debonding zone only. Unlike previous experiments, no cracking was observed within the interface of the concrete and the ECC link slab, since additional shear studs were provided only within the interface for reducing the stress concentration by the composite action of the girder and the deck.

The first field application of the ECC link slab was designed and implemented in the State of Michigan in 2005 (Li et al. 2005). The design procedure adopted by previous researchers (Caner & Zia, 1998; Kim et al. 2004) was validated by the strong correlation of the girders end-rotation and strain development on the link slab surface. The maximum tensile strain development of the ECC link slab was less than the elastic limits with the proposed end-rotation below the maximum

allowable AASHTO's rotation of 0.00375 radian. Also the simply supporting behaviour of the girders was maintained with the continuous deck slab. The major encountered problem was the early shrinkage of the ECC that caused additional stresses followed by micro-cracking formation specifically within the link slab and deck interface before the applied loading.

Qian et al. (2009) finalized the design procedure for the effective length of the ECC link slab, after extensive testing with different debonding zone length. Based on the analysis, it was suggested that length of the link slabs falls between the inflection points. The locations of the inflection points vary from 0 to 20% based on the stiffness of the link slab. With a low structural stiffness of the ECC, Qian et al. (2009) recommended 7.5% of adjacent span's length for the total length of the ECC link slab (Equation 2.3).

$$L_{ls} = 7.5\%(L_1+L_2) \hspace{5cm} (2.3)$$

where L_{ls} denotes the total length of the link slab and L_1 and L_2 represents the length of the adjacent bridge spans.

They have also suggested adding a transition zone within the interface of the concrete deck and the link slab for shifting the stress concentration to debond zone only. The length of the transition zone with installation of additional 50% shear connector was set as 2.5% of the span's length (Figure 1.2).

The high production cost of the ECC encouraged the scholars to develop an economical and greener mixture using locally available crushed sand and supplementary cementitious material for the purpose of the link slab application (Sahmaran et al. 2009 ; Maulin, 2012; Sherir, 2012). Maulin (2012) investigated the structural performance of the scaled down link slab with different reinforcing ratios (0.01 and 0.012), and using the green ECC mix incorporating crushed sand and fly ash F at 70% replacement of cement. The experimental investigation revealed that number of micro-cracking was reduced at higher reinforcing ratio due to increased structural stiffness. Also there was apparent difference for structural performance due to the change of aggregate type and size as well as use of fly ash.

Sherir (2012) reported the creep performance for a duration of six months (monitoring still continues at Ryerson University for the last three years) of the link slabs by comparing the

influence of the crushed and micro-silica sand based ECC to a normal concrete. The experimental investigation revealed that more cracks were formed for the crushed sand based ECC link slab compared to those with micro-silica sand. The link slab with normal underwent less creep damage due to the presence of larger aggregates with higher modulus of elasticity. ECC link slabs showed more deformation due to the high strain hardening capacity due to the presence of polyvinyl alcohol (PVA) fibers.

Hossain and Anwar (2014) conducted experimental investigations by introducing different ECC mixtures made with different types of sand (crushed and micro-silica sand) and supplementary cementitious material (fly ash, volcanic ash and volcanic pumice) for the link slab application. The influence of crushed sand, volcanic ash and ground pumice on the structural performance of the link slabs was evaluated based on the load-deformation, ductility and energy absorbing capacity. The analysis revealed that crushed sand developed higher ultimate load and energy absorbing capacity compared to silica sand, whereas the pumice based ECC link slabs developed higher bending deflection but lower ultimate load capacity.

2.3 Existing Design Guidelines for ECC Link Slab

After experimental investigation and field demonstration, Lepech and Li (2009) developed a design guideline for the ECC link slab. The overall length of the link slab and the debonding zone based on the pervious experimental research was modified further to calculate length of the link slab and debonding zone as per Equations 2.4 and 2.5 respectively.

$$L_{ls} = 7.5\%(L_1 + L_2) + G_{1-2} \tag{2.4}$$

$$L_{dz} = 5\%(L_1 + L_2) + G_{1-2} \tag{2.5}$$

where L_{ls} and L_{dz} denote the length of the link slab and debonding zone respectively; L_1 and L_2 represent the length of the adjacent spans and G_{1-2} symbolizes the length of the gap between the girders of the adjacent spans.

Equation 2.6 is proposed for determining the applied moment on the link slab (M_{ls}) imposed by the maximum end rotation of the adjacent bridge spans:

$$M_{ls} = \frac{2E_{ECC}I_{ls}}{L_{dz}} \theta_{max} \tag{2.6}$$

where E_{ECC} is the modulus of elasticity of the ECC, θ_{max} is the maximum end rotations and I_{ls} represents the uncracked moment of inertia as per Equation 2.7.

$$I_{ls} = \frac{B_{ls}t^3}{12} \tag{2.7}$$

where B_{ls} and t denotes the width and thickness of the link slab, respectively.

Based on American Association of State Highway and Transportation Officials (AASHTO's, 2012 design code), the maximum end rotation caused by the live load depends on the maximum allowable deflection of the adjacent simply supporting bridge spans can be obtained as per Equation 2.8.

$$\theta_{max} = \Delta_{max-short} \left(\frac{3}{L_{short}} \right) \tag{2.8}$$

where θ_{max} represents the maximum end-rotation angle of the adjacent bridge spans, measured in radians, $\Delta_{max-short}$ denotes the maximum allowable deflection of the shorter spans in mm and L_{short} is the shorter adjacent spans length in mm. With the maximum allowable deflection based on the AASHTO's code is limited to L/800, the maximum end rotation imposed by adjacent spans will be equivalent to 0.00375 radian.

Lepech and Li (2009) used iterative design procedure for determining the adequate reinforcing ratio, starting with the minimum reinforcement. Through the analysis, the selected reinforcing ratio was adjusted accordingly to resist the applied moment imposed by the girders end-rotation. Unlike conventional RC link slab, the resisting moment was based on the structural loading capacity rather than serviceability requirements due to micro-cracking behaviour of the ECC (Lepech & Li. 2006). The resisting moment capacity of the link slab was determined based on the non-linear sectional analysis with the assumption of a perfectly elastic-plastic response for the ECC. For the conservative design practice, the linear tensile strength of the ECC was used while ignoring the strain hardening characteristic (as seen in the typical stress-strain characteristics, Figure 2.1) after the first cracking (Lepech & Li. 2009). After extensive tensile test results on ECC, Lepech and Li (2008& 2009) proposed a yielding stress and strain of 3.45MPa and 0.02%, respectively based on the first cracking responses.
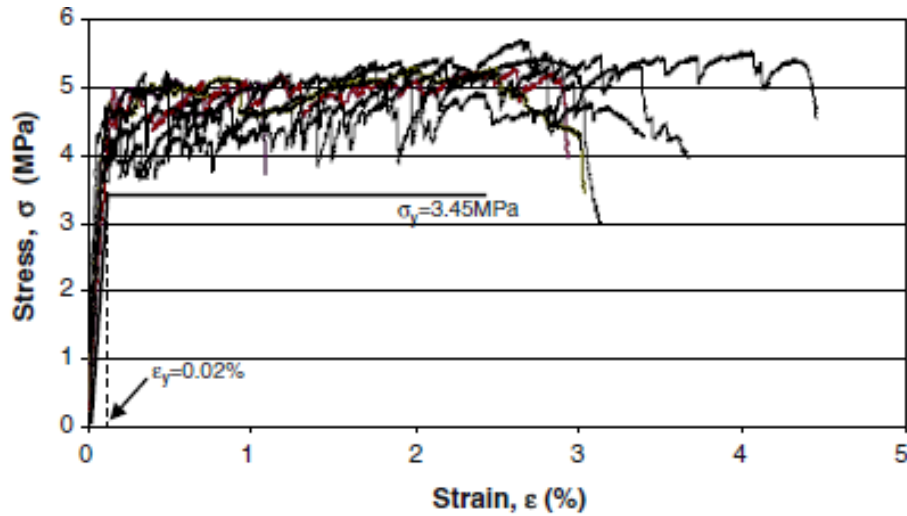
Figure 2.1: Idealized Elastic-Plastic Response of the ECC (Lepech &Li 2009)

For finding resisting moment capacity, the same stress criterion was adopted by Caner and Zia (1998) using 40% of the yield strength of the reinforcement as a conservative working stress (Equation 2.2). The elastic and plastic responses of the ECC section develop a tension kink for the concrete's tensile stress. The location of the tension kinks for the ECC and the resisting strains and stresses across the depth of the ECC link slab are illustrated in Figure 2.2.
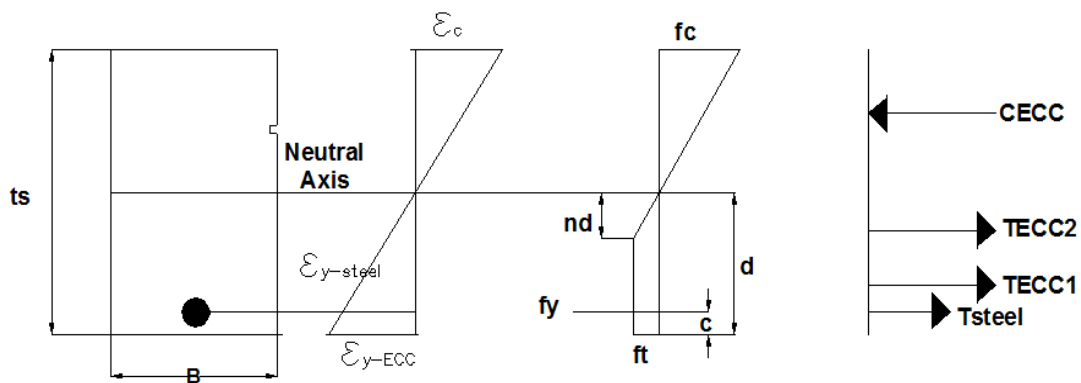
Figure 2.2: Strain, Stress Distribution of ECC Link Slab for Non-Linear Sectional Analysis (Lepech & Li 2009)

B and t_s in Figure 2.2 represent the width and the depth of the link slab, respectively, ε_c, $\varepsilon_{y\text{-steel}}$, and $\varepsilon_{y\text{-ECC}}$ represent the compressive strain and yielding strain of reinforcing steel and ECC,

14

respectively. 'd' symbolizes the distance from the neutral axis to the rebar and 'C' denotes the distance from the tension face to centroid of the rebar.

The proposed stress criterion by Caner and Zia (1998) was used to determine the corresponding tension kink and neutral axis for calculating the resisting moment capacity. The modular ratio is presented by Equation 2.9.

$$n_\varepsilon = \frac{\varepsilon_{y-ECC}}{0.4\,\varepsilon_{y-Steel}} \tag{2.9}$$

The n_ε represents the yield strain (modular) ratio, ε_{y-ECC} and $\varepsilon_{y-Steel}$ denote the yield strain of the elastic-plastic behaviour of ECC and steel reinforcement, respectively.

The depth of the neutral axis was determined based on the modular ratio and the equilibrium of resisting forces across the depth of ECC link slab. Lepech and Li (2009) proposed equations for calculating the ECC tensile forces. The resisting forces across the depth of the ECC link slab and their equilibrium are presented through Equations 2.10 to 2.13 and 2.14, respectively.

$$T_{steel} = (0.4f_{y\text{-}steel})A_s \tag{2.10}$$

$$T_{ECC\text{-}1} = f_t\,[(1-n_\varepsilon)d+c]B \tag{2.11}$$

$$T_{ECC\text{-}2} = 0.5f_t\,n_\varepsilon dB \tag{2.12}$$

$$C_{ECC} = 0.5 \qquad\qquad f_t \qquad\qquad (\frac{1}{n_\varepsilon d})(t_s\text{-}d\text{-}c)^2 B$$

$$\tag{2.13}$$

$$T_{steel} + T_{ECC1} + T_{ECC2} = C_{ECC} \tag{2.14}$$

The T_{steel}, $f_{y\text{-}steel}$ and A_s are denoting the tensile force, yielding stress and total area of the provided steel reinforcement. The $T_{ECC\text{-}1}$, $T_{ECC\text{-}2}$, f_t and C_{ECC} are representing the tensile forces, tensile stress and compressive force of the ECC, respectively.

The resisting moment capacity, $M_{r\text{-}ls}$ is calculated by summing the contribution of all forces about the neutral axis and is presented in Equation 2.15.

$$M_{r-ls} = \left\{ T_{Steel}d + T_{ECC-1} \left(\frac{(1-n)d+c}{2} + nd \right) + T_{ECC-2} \left(\frac{2}{3} \right) nd + C_{ECC} \left(\frac{2}{3} \right) (t_s - d - c) \right\} \quad (2.15)$$

The selected reinforcing ratio is adjusted accordingly so that the resisting moment is greater than the applied moment. With the finalized reinforcing ratio, the adequate spacing of the longitudinal rebar is determined by Equation 2.16.

$$S = \frac{A_{bar}}{\rho t_s} \quad\quad\quad (2.16)$$

where S represents the bar spacing, A_{bar}, ρ, t_s represent the cross-sectional area of the selected rebar, reinforcing ratio and link slab thickness, respectively.

Further, the transition zone is designed with additional 50% shear stud connectors in accordance with AASHTO design procedure for accounting the large shear transfer within the bridge deck and link slab interface (Qian et al. 2009).

2.4 Engineered Cementitious Composite (ECC)

ECC, a new generation of high performance fiber reinforced cementitious composite, has been designed with unique micro-mechanical properties for achieving a high ductility and damage tolerance under tensile and shear loading(Li & Kanda 1998; Li 1998; Li 2003; Li et al. 2001). The major characteristic that distinguishes ECC from other types of fiber reinforced concrete (FRC) is its high tensile strain capacity of 3 to 5%. The systematically engineered micro-mechanical parameters associated with fiber, matrix and control of interfacial properties lead to high strain hardening characteristic with multiple micro-cracking behaviors (Li 1993; Li 1998; Lin et al. 1999). A unique fracture property of ECC is attained through the careful customization and proportioning of the material such as selecting specific fiber properties (suitable strength, modulus of elasticity and aspect ratio) along with effective interfacial properties of fiber and the matrix (Li 2003). In compare to other HPFRC, a short discontinuous fiber with 2% volume is used in the ECC mix for achieving a high performance concrete for structural applications. The

typical mixing proportion of a first generation of ECC using polyvinyl alcohol (PVA) fiber is presented in Table 2.1.

Table2.1: Typical Mix Design Proportion of ECC by Weight (Li 2003)

Cement	Fly Ash	Sand	Water	HRWRA	Fiber (%)
1	1.2	0.8	0.58	0.013	2

Different types of fibers have been incorporated into ECC mixtures, but PVA fibers were found to be most effective and efficient for achieving the strain hardening characteristic after the first crack formation (Weimann & Li 2003). The typical uniaxial tensile stress-strain curve and cracking development of the ECC at 2% PVA fiber is presented in Figure 2.3.
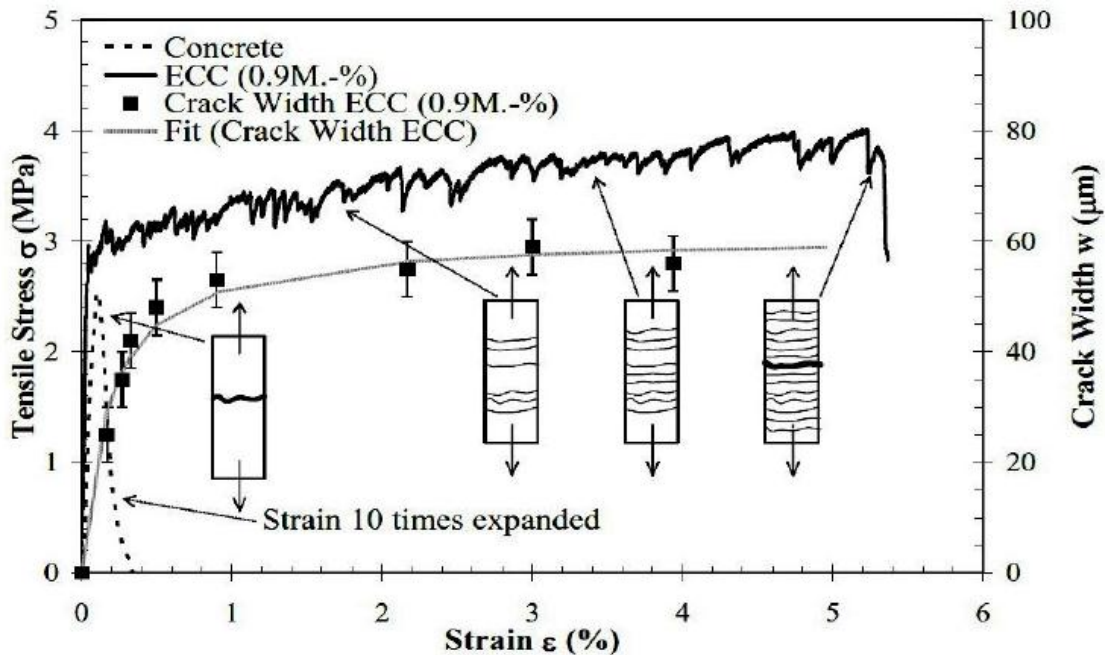
Figure2.3: Tensile Stress-Strain Curve and Crack Width Development (Weimann & Li. 2003)

After first crack formation, ECC's tensile stress is increased further due to its unique strain hardening characteristic. The crack widths at ultimate loading are remained below 80 µm. The steady-state cracking behaviour is independent to the type of the loading and amount of fiber reinforcement (Özbay et al. 2013; Ranade et al. 2014). The strain hardening characteristic and

17

micro-cracking behaviour are attained by the strength and fracture energy criteria proposed by Kanda and Li (1998). The satisfaction of the criterion will ensure the initiation of micro-cracking from initial flaw sites in the composites before the tensile loading reach the fiber bridging capacity (Kanda & Li 1998, Yang & Li 2006). The use of these micromechanical models for tailoring ECC material ensures the strain hardening characteristic and large bending capacity (Figure 2.4) similar to a ductile metal plate at its plastic deformation phase (Li 2011; Nawy 2008).

Using the same strength and fracture energy criteria, Sahmaran et al. (2009) further developed a greener ECC by incorporating locally available crushed sand aggregates and fly ash as a replacement of cement. Although each material influenced the mechanical and durability properties of the hardened ECC, but similar responses were attained as observed in experimental results.

Figure2.4: Ductile Response of ECC under Flexural Loading (Li 2011)

2.4.1 Materials for ECC

The multiple micro-cracking behaviour and strain hardening characteristic of the ECC are mainly influenced by the proportion and behaviour of the incorporated materials. Further, with

advancement of greener ECC, a great depth of knowledge and literature review is required to understand the fundamental role of each material for tailoring effective matrix and fiber interface for maintaining the strain hardening characteristic. The roles of fibers, fly ash replacement and influence of sand aggregates within the ECC mixes are discussed below.

2.4.1.1 Role of Fibers

The most common type of fiber used for production of ECC is Polyvinyl Alcohol (PVA) fibers at 2% volumes. The short, discontinuous PVA fiber with high tensile strength and modulus of elasticity enhance the matrix's toughness while carries tensile stresses after the first crack formation through the fiber bridging characteristic. The fiber bridging transfers the stresses across the crack for maintaining the low crack widths (JCI-DFRCC Committee 2003). The surface of the PVA fiber is oil coated (by 1.2% of mass) to tailor the interfacial properties among the fiber and matrix for strain hardening performance (Li 2003; Li et al. 2002). The oil coating reduces the interfacial bonding, while increasing the tensile strain capacity of the ECC mix, therefore under tensile stresses; the fiber tends to be ruptured rather than pull out like other FRC (Li et al. 2002). Table 2.2 summarizes the essential properties of the PVA fiber for maintaining the strain hardening characteristic of the ECC mix.

Table 2.2: Geometrical and Mechanical Properties of PVA fiber

Diameter (μm)	Length (mm)	Nominal Strength (MPa)	Modulus of Elasticity (GPa)
39	6 to 12	1620	42.8

2.4.1.2 Fly Ash

Fly ash has been incorporated into ECC mixtures at different replacement rate of the cementing material. Fly ash is a fine powder (typically 20 to 50 μm in size) produced through the by-product of pulverized coal blown into a fire furnace at a power generating plant. The chemical compositions similar to the cementing material with much higher surface area typically between 250-600 m^2/kg allows a better reaction with calcium hydroxide (Kosmatka & Panarese 1988; Neville 2002). The use of fly ash in the ECC mix leads to reduction of interfacial bonding among

19

the PVA fiber and the matrix while increasing the frictional bonding among them (Wang & Li 2007; Sahmaran et al. 2009; Peled & Shah 2003). These characteristic are responsible for the tight crack width, improved ductility, durability and sustainability of the ECC mix (Yang et al. 2007; Bisaillon et al. 1994; Hussian & Rasheeduzzafar 1994; Kuroda et al. 2000; Lepech & Li 2005b; Karahan et al. 2012).

Depending on the type, physical and chemical composition of the fly ashes, the characteristic and performance within the mix could influence the mechanical properties. According to American Society for Testing and Materials (ASTM), there are two classes of the fly ashes. There is class C fly ash with a high calcium content and class F with lower calcium content. The high calcium content of class C allows a self-hardening process of the mix without the presence of any cement (ASTM C618 2012). The specification for fly ashes in accordance to ASTM C618 is presented in Table 2.3.

Table 2.3: Specifications for Fly Ash

Class of Fly Ash	ASTM Specification
Class C	$SiO_2+Al_2O_3+Fe_2O_3> 50\%$
Class F	$SiO_2+Al_2O_3+Fe_2O_3> 70\%$

2.4.1.3 Role of Aggregates

The aggregate type and size plays a significant role for fiber dispersion within the ECC mix to obtain a strain hardening and micro-cracking behaviour. The uniform fiber dispersion becomes more difficult with increasing maximum aggregate size. The clumping and interaction of fibers would occur at higher volume and maximum aggregate size and simultaneously the increase in interface toughness reduces the ductility of the ECC mix (Sahmaran et al. 2009). As a result, the standard ECC incorporates micro-silica sand (maximum size of 110μm) with an aggregate to binder ratio of 0.36 to maintain adequate stiffness and volume stability (Li et al. 1995). Researches revealed that using crushed sand with maximum aggregate size of 1.19 mm did not significantly influence the fiber dispersion and similar ductility responses and strain hardening characteristic of using micro-silica sand were attained (Sahmaran et al. 2009; Maulin 2012; Sherir 2012).

2.4.2 Mechanical Properties

2.4.2.1 Compressive Strength

ECC exhibits a similar compressive strength as high performance concrete (HPC), typically ranging from 40 to 60 MPa depending to the mix design parameters (Sherir 2012; Hossain & Sherir 2014). While a low young's modulus of 20.4 GPa is employed, a linear behaviour under compression prior to failure similar to HPC is attained (Wang & Li 2003).

The compressive strength of the ECC mix is reduced at higher fly ash content due to slow reactivity and development of hydration products at initial early ages (Hossain & Sherir 2014; Mindess et al. 2003). The compressive strength of the ECC mix is improved by using larger sand aggregates such as crushed sand. The increase in maximum size results as a higher volume and dense interfacial transition zone among the sand particle and the matrix (Hossain & Sherir 2014; Mehta & Monteiro 2006).

2.4.2.2 Flexural Strength

The unique micro-structure of the ECC allows a high tensile strain capacity with multi micro-cracking and strain hardening characteristic (Li 2011). Based on the mix design parameters, the flexural strength of the ECC varies from 5 to 16 MPa (Wang & Li 2003).

Through extensive experimental investigations, it was confirmed that flexural strength of the ECC is reduced with increasing fly ash content due to reduced interface toughness among the PVA and the mortar, while the bending capacity is enhanced with improved frictional bonding. Using larger sand aggregates such as mortar or crushed sand, improved the flexural strength capacity, whereas the ductility was reduced due to increased interface toughness (Hossain & Sherir 2014; Sahmaran et al. 2009; Li et al. 1995). Figure 2.5 illustrates the typical flexural strength response of a green ECC mix with high volume of fly ash at replacement levels of 55% and 70%.
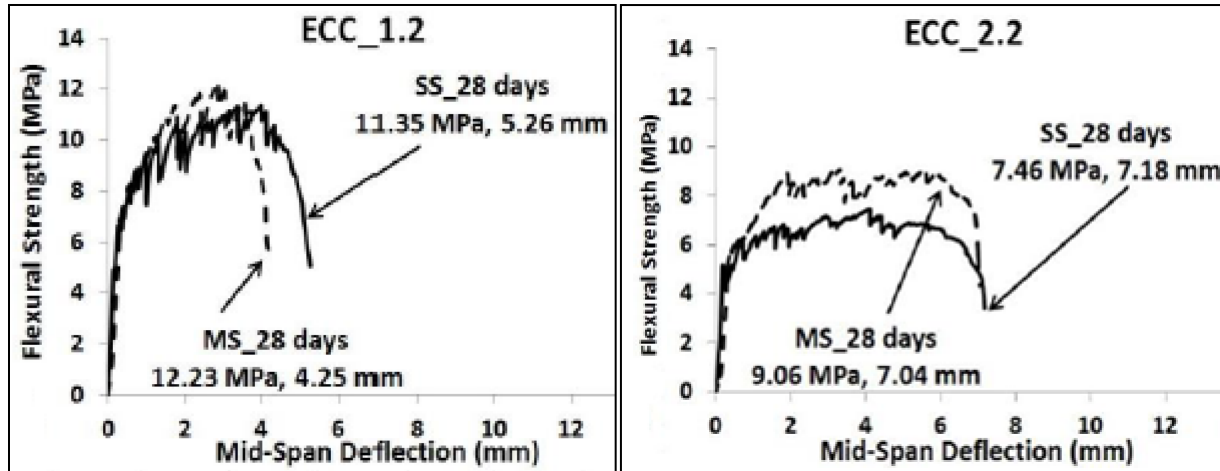
Figure 2.5: Typical Flexural Strength–Mid Span Deflection of Green ECC (Hossain & Sherir 2014)

2.4.2.3 Fatigue Flexure

Many scholars have investigated the durability and mechanical properties and failure mechanism of the ECC subjected to monotonic loading. However few studies have been conducted on the flexural fatigue performance and failure mechanism of the ECC mix. The fatigue flexure behaviour of ECC is important for its application in bridge structures.

Matsumoto (1998) investigated the flexural fatigue performance of the polyethylene fiber based ECC (PE-ECC) and normal concrete by their failure modes, associated failure mechanism and fatigue strength life cycle analysis (SN-curve). The test results revealed that unlike normal concrete, PE –ECC formed multiple micro-cracking under fatigue loading until the fibers were ruptured to their ultimate strength. Due to the lack of experimental data, Matsumoto was not able to develop a S-N curve, predicting the life cycle analysis of the ECC mix. Zhang and Li (2002) explored the performance of the ECC/concrete overlay within the rigid pavement subjected to constant fatigue stress induced by truck loading. The flexural fatigue test monitoring confirmed that ECC overlay improved the strength and deformability capacity, at least double the concrete over concrete overlay.

Suthiwarapirak et al. (2004) conducted experimental research on the fatigue performance of shotcreted PVA-ECC repairing material. Similar to PE-ECC, multiple micro-cracking was observed until the fibers were ruptured. The test results demonstrate a bilinear function stress life

relationship (SN-curve) with similar response, shape and mode of failure close to metal fatigue fracture.

Sherir (2012) performed an extensive flexural fatigue testing on different ECC specimens, incorporating 70% fly ash content and use of fine aggregates of micro-silica and crushed sand. He adopted two different approaches; variable fatigue stress level (40%, 55% and 70%) and different fatigue cycles (100000, 200000, 300000, 1 million) for investigating the flexural fatigue performance of ECC mixtures. The experimental investigation revealed that mid-span deflection evolution, number of micro-cracking and damage level was significantly increased at higher fatigue stress levels and cycles. For both approaches, the damage level was higher for silica-sand based ECC in compare to crushed sand. It is found that fly ash behaved as a filler material instead of hydrating products with larger sand aggregate size. Therefore, the densification of the matrix improved the flexural fatigue performance of the crushed sand based ECC.

2.5 Summary

Extensive experimental investigation have been performed on material properties of ECC mix incorporating locally available sands and fly ashes for tailoring enhanced mechanical and durability properties similar to HPC. With extensive material engineering, there is a lack of experimental validation of using green ECC mixtures in structural applications such as link slabs for joint free bridge deck structures. For more than a decade different scholars have performed theoretical and experimental investigations on structural and durability performance of link slab by varying geometrical dimensions and using normal concrete and traditional ECC mix. Limited equations were proposed for designing a link slab based on the field demonstration of the ECC link slab in State of Michigan. However, there is a lack of experimental results for tailoring the optimized green ECC mix and developing design equations for the fatigue performance of the link slab.

CHAPTER THREE
EXPERIMENTAL PROGRAM

3.1 Introduction

An extensive experimental program has been planned for studying the structural performance of the link slabs subjected to monotonic static and flexural fatigue loading. Seven types of ECC mixtures with different types/dosage of fly ash and sand aggregates were used to construct $1/4^{th}$ scale model link slab specimens. For a comparative structural performance evaluation, link slab specimens made with a ready-mix SCC were also constructed and tested under static and flexural fatigue loading conditions. In addition, a $1/6^{th}$ scale full joint-free bridge model having two simply supported spans connected together with ECC link slab was also tested under monotonic loading up to the service load.

This chapter describes full details of the experimental investigations on $1/4^{th}$ scale link slab specimens and $1/6^{th}$ scale joint-free full bridge with ECC link slab illustrating materials used for ECC/SCC mix designs, geometric dimensions of link slabs/full bridge specimens, design of link slabs/full bridge, casting and curing of specimens, testing scheme, instrumentation of specimens, test set-up, testing procedure, ECC/SCC properties and steel properties. This chapter also describes the design of link slab and full bridge specimens and calculation procedures of moment resistance of link slab and full bridge model specimens based on theoretical and design specifications.

3.2 Design of Link Slabs and Full Bridge Models and Geometric Dimensioning Details

The design of the link slabs and full bridge model specimens was conducted as per Caner and Zia (1998). The typical deformed shape and moment distribution due to the applied loading for a two span simply supported bridge structure with a link slab is schematically represented in Figure 3.1. Flexural crack formations were expected at the top of the link slab due to the development of tensile stresses. The link slab section is designed between the points of inflections. Based on the stiffness of the link slab, the location of the inflection points varies from 0 to 20% of the adjacent span's length (Kim et al. 2004; Caner & Zia, 1998).

24
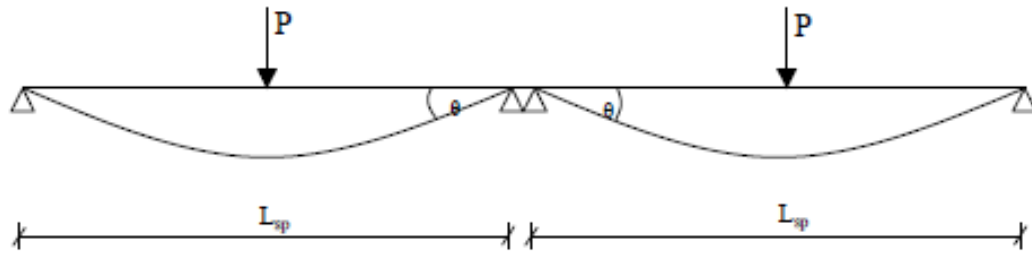
(a) Deformed Shape of the bridge

Girder rotation

Link slab deformation and flexural crack formation

Debond Length

Inflection point (M=0)   Inflection point (M=0)
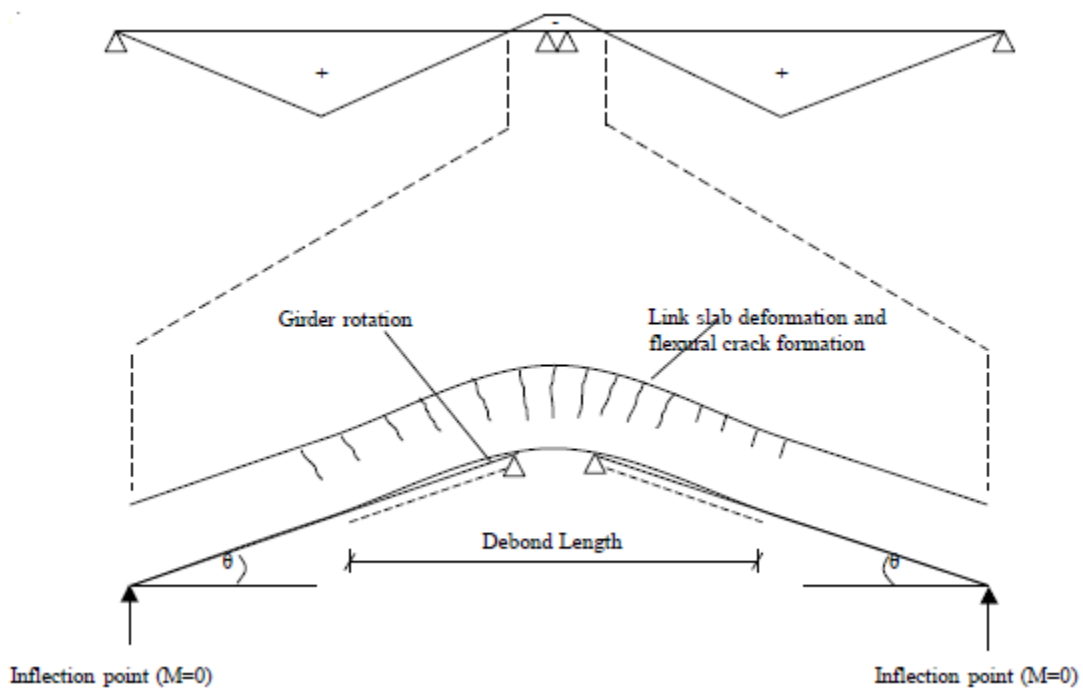
(b) Moment Distribution and flexural crack formation on link slab

Figure3.1: Two Span Bridge Deformation with Focus on Link Slab Section (Kim et al. 2004)

3.2.1 One Fourth Scale Link Slab Design and Configurations

The model was focused on the link slab section within the inflection points as shown in Figure 3.1. The location of inflection points (length of the link slab) based on the stiffness of the section (ECC and the steel rebar) was determined as 6.5% of the adjacent span's length. The summary of the link slab specimen's configurations, reinforcement detailing and concrete mixtures are presented in Table 3.1. Overall, the total length of the link slab for the 1/4th scale model was 810 mm as shown Figure 3.2 and Table 3.1. The length of the debonding zone based on the proposed

25

design guidelines by Caner and Zia (1998), was set as 5% of simple spans - a total length of 330 mm. The length of the transition zone with additional 50% shear stud connector (total of 16 studs) was selected as 300 mm following Qian et al. (2009). The cross-sectional dimensions for the 1/4th link slab models were 175 mm in width and 60 mm in depth. A minimum longitudinal steel reinforcing ratio of 1.1% (three 6 mm bars) were provided for maintaining a low structural stiffness of the link slab. Additional transverse reinforcements at 210 mm c/c spacing were provided using 6mm bars (Figure 3.2 and Table 3.1). In total 13 link slab specimens were cast - 9 specimens for monotonic and 4 specimens for flexural fatigue testing. The link slab designation shown in Table 3.1 has two parts: First Part "LS-*" represents specimen number and the second part such as "ECC-**-**-**" or "concrete type-fly ash type - % of fly ash as cement replacement-type of sand" represents concrete mixture that is used in the debonding zone. For Example: ECC-CI-1.2-SS where ECC means engineered cementitious composite, CI means class of fly ash, 1.2 represents 55% cement replacement by fly ash and SS means silica sand.

Table3.1: Link Slab Specimens Configuration Subjected to Monotonic and Fatigue Loading

Link Slab Designation	Length (mm)	Debonding Zone Length 5% (mm)	Transition Zone Length 2.5% (mm)	Concrete in Transition Zone	Concrete in Debonding Zone
Tests under monotonic loading ¼ Scale Link Slab					
LS2-ECC-CI-1.2-SS	810	330	150	SCC	ECC-CI-1.2-SS
LS3-ECC-F-2.2-SS	810	330	150	SCC	ECC-F-2.2-SS
LS4-ECC-F-1.2-SS	810	330	150	SCC	ECC-F-1.2-SS
LS6-ECC-F-2.2-CS	810	330	150	SCC	ECC-F-2.2-CS
LS10-ECC-CI-2.2-SS	810	330	150	SCC	ECC-CI-2.2-SS
LS11-ECC-CI-2.2-CS	810	330	150	SCC	ECC-CI-2.2-CS
LS28-ECC-CI-1.2-MS	810	330	150	SCC	ECC-CI-1.2-MS
LS25-SCC	810	330	150	SCC	SCC
LS32-SCC	810	330	150	SCC	SCC

Test under Fatigue loading-1/4 Scale Link Slab								
Link Slab Designation	Length (mm)	Debond Zone Length 2.5% (mm)	Transition Zone Length 5% (mm)	Concrete in Transition zone	Concrete in Debond zone	Number of Cycle	Mean Fatigue Stress Level (%)	Fatigue Stress Range (%)
LS29-ECC-CI-1.2-MS	810	330	150	SCC	ECC-CI-1.2-MS	400,000	40	±20
LS30-ECC-CI-1.2-MS	810	330	150	SCC	ECC-CI-1.2-MS	400,000	55	±20
LS31-ECC-CI-1.2-MS	810	330	150	SCC	ECC-CI-1.2-MS	1 million	40	±20
LS33-SCC	810	330	150	SCC	SCC	400,000	40	±5

CI- class CI flay ash; F: class F fly ash; SS: silica sand; CS: crushed sand; MS: mortar sand; 1.2: 55% fly ash as cement replacement, 2.2: 70% fly ash as cement replacement; LS: link slab; SCC: self-consolidating concrete
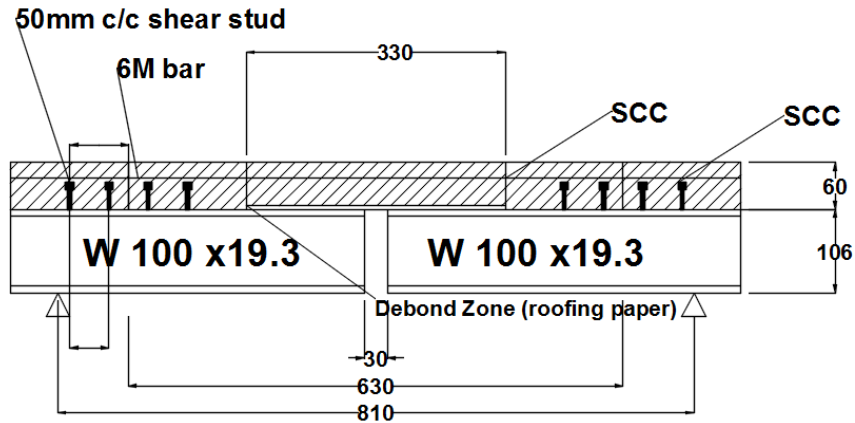
(a) SCC Link Slab
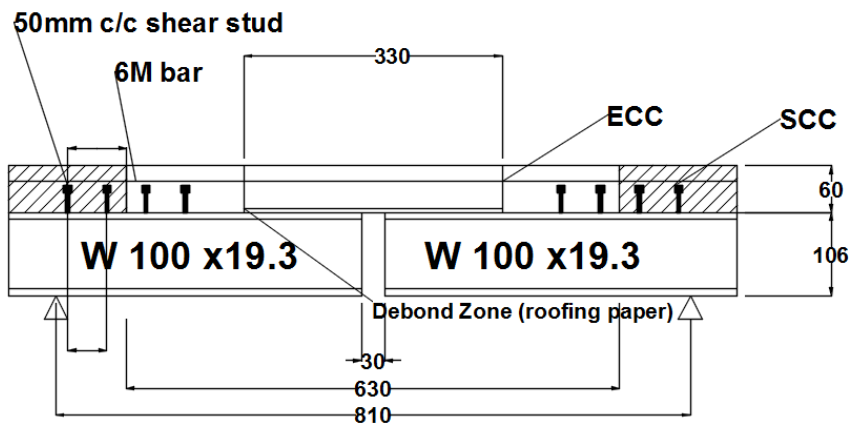
(b) ECC Link Slab
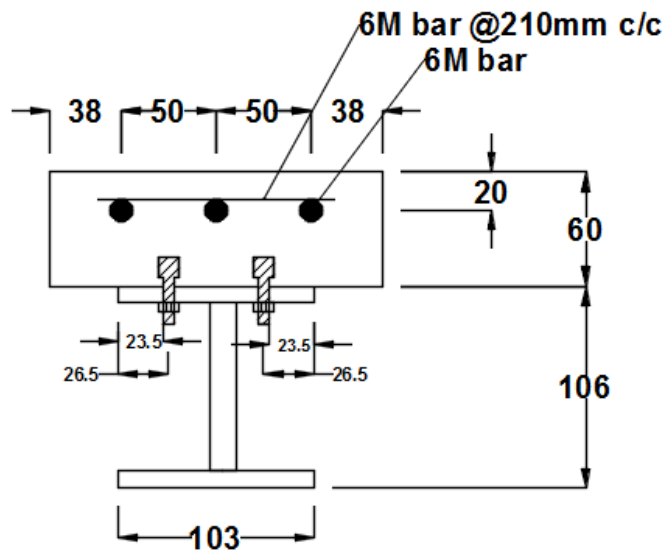
(c) Link Slab Cross-Section

Figure 3.2: Geometry and Reinforcement Details of Link Slab (Dimensions in mm)

3.2.2 One Sixth Scale Full Bridge Specimen

The 1/6th scale full bridge model consists of two simply supported composite spans (Span 1 and Span 2: made of steel I-beam and concrete decking connected through shear studs) with connecting ECC link slab. The two simply supported bridge spans are denoted as SP1-SCC and SP2-SCC, and the connecting ECC link slab is designated as LS-ECC. The dimensions, reinforcement detailing and selected mixtures for each segment of the full bridge model are presented in Table 3.2.

Table 3.2: Geometric Properties and Reinforcement Detailing for Each Segment of Full Bridge Model

Section	Length (mm)	Debond Zone Length 5% (mm)	Transition Zone Length 2.5% (mm)	Concrete	Longitudinal Reinforcing Ratio	Number of 10 M shear Stud	Center to center Shear Stud Spacing (mm)
SP1-SCC	1000	0	0	SCC	0.01	24	75
LS-ECC		240	100	ECC-CI-1.2-MS	0.01	8	45
SP2-SCC	1000	0	0	SCC	0.01	24	75

The 1/6th scale full bridge model was 300 mm in width and 55 mm in depth with overall length of 2190 mm. The simply supported adjacent SCC spans (SP1-SCC & SP2-SCC) were designed in accordance to Canadian Highway Bridge Design Code (CHBDC, 2006). The code requires a minimum longitudinal reinforcing ratio of 0.01, therefore the minimum ratio was provided at the bottom of the SCC segments (with 19 mm clear cover) due to the development of positive bending moment. Mechanical shear studs (10 mm in diameter) were provided at 75 mm center to center spacing for maintaining the composite actions of the SCC with the steel girder in accordance to CHBDC (2006). The equations based on CHBDC guidelines for shear stud capacity are presented in Equations 3.1 to 3.3.

Minimum $\{P= \emptyset_s A_s F_y \quad$ and $P=0.85\emptyset_c f_c B t_c + \emptyset_r A_r F_y \quad \}$ (3.1)

Minimum $\{q_r = 0.5\emptyset_{sc} A_{sc} \sqrt{f_c E_c} \quad$ and $q_r = \emptyset_{sc} A_{sc} \ F_u \ \}$ (3.2)

$N = P/q_r$ (3.3)

where P represents the applied shear force at the interface; A_s, F_y, $\emptyset_s$ denote cross-sectional area of steel girder, yielding stress and factor of safety (0.95), respectively; B, t_c, f_c, $\emptyset_c$ symbolize width, thickness, compressive stress, and factor of safety for the concrete deck, respectively; A_r, F_y, $\emptyset_r$ denote the steel reinforcing area, reinforcement yielding stress and factor of safety for the rebar, respectively; q_r denotes the capacity of one shear stud; A_{sc}, F_u, $\emptyset_{sc}$ are symbolizing the cross sectional area of one stud, the ultimate tensile resistance of one stud and resisting factor of 0.85, respectively; N represents the total number of required shear stud.

The ECC link slab connecting the simply supported SCC decks were designed in accordance to the design guide proposed by Lepech and Li (2009). The total length of the ECC link slab was 7.5% of the adjacent SCC spans, in total of 340 mm (Equation 2.4). The length of the debonding zone, similar to pervious link slab specimens, was set as 5% of simply supported spans; a total length of 240 mm (Equation 2.5). The total length of the transition zone based on Lepech and Li (2009) was 100 mm (2.5% of adjacent spans). A minimum longitudinal steel reinforcing ratio of 1.1% (4, 6 mm bars) was provided for maintaining a low structural stiffness of the link slab, while resisting the developed negative moment due to the applied loading. Additional transverse reinforcements were provided at 130 mm c/c spacing using 6 mm bars. The schematic representation of the 1/6th scale full bridge model, including geometric dimensioning, reinforcement detailing and concrete mixtures are presented in Figure 3.3.

(a) Cross-sectional View

(b) Elevation View
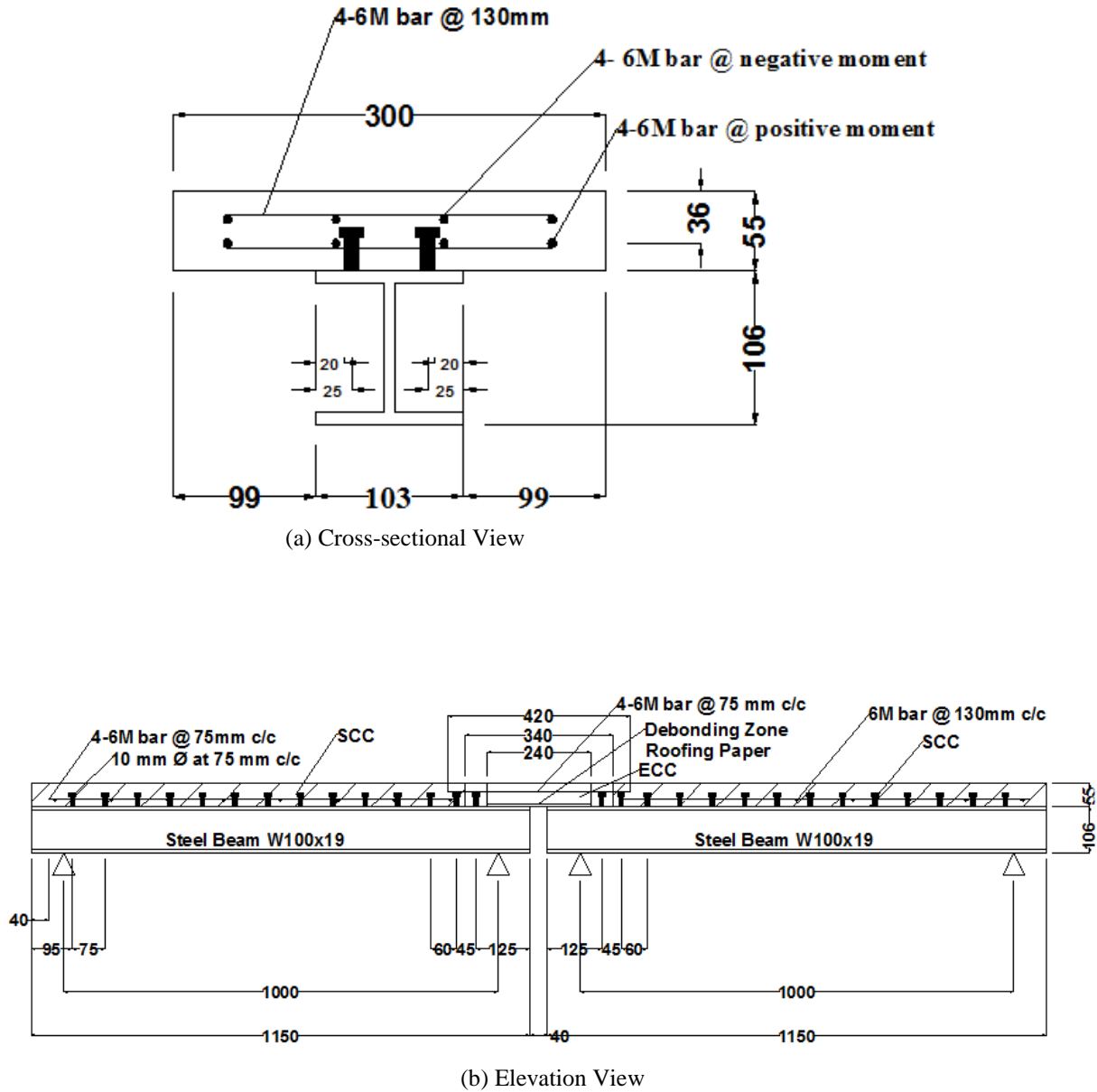
Figure 3.3: Geometry and Reinforcement Details of Full Bridge (Dimensions in mm)

3.3 Material and Properties

Seven ECC mixtures and one ready mix SCC mix were used for the deck construction of the scaled down link slabs and full bridge specimen. Seven ECC mixtures were designed by incorporating different types/dosage of fly ash (class CI and F with 55% (1.2) and 70% (2.2) cement replacements) and different sand aggregates (crushed sand 'CS', silica sand 'SS' and mortar sand 'MS') were used for construction of link slabs. The SCC mixture was a commercial

31

ready mix having 10 mm maximum size coarse aggregates. For both models a W100 x19 steel structural section in accordance to Canadian Institute of Steel Construction (CISC) (2010) was used as a supporting girders. The reinforcing steel bars were 6mm in diameter with a mean yield and ultimate strength of 407 MPa, 550 MPa and 224 GPa, respectively.

3.3.1 Engineered Cementitious Composites

Seven ECC mixtures incorporating different types/dosage of fly ash and sand aggregates were developed at Ryerson University over the last 5 years. The mix designs of the ECC mixtures are presented in Table 3.3.

Table 3.3: ECC Mix Design Proportions

	Micro-Silica Sand						
	Ingredients per weight of cement						
Mixture ID	Water	Cement	FA	Sand	PVA	HRWRA	W/b [*]
LS2-ECC-CI-1.2-SS	0.581	1	1.2	0.798	0.045	0.009	0.27
LS3-ECC-F-2.2-SS	0.847	1	2.2	1.160	0.067	0.010	0.27
LS4-ECC-F-1.2-SS	0.581	1	1.2	0.798	0.045	0.009	0.27
LS10-ECC-CI-2.2-SS	0.847	1	2.2	1.160	0.067	0.010	0.27
Crushed Sand							
LS6-ECC-F-2.2-CS	0.848	1	2.2	1.159	0.069	0.010	0.27
LS11-ECC-CI-2.2-CS	0.848	1	2.2	1.159	0.069	0.010	0.27
Mortar Sand							
LS28-ECC-CI-1.2-MS	0.585	1	1.2	0.798	0.046	0.009	0.27

[*] W/b- Water to binder ratio; PVA: poly vinyl alcohol fiber, FA: fly ash,

The cement used for all 7 ECC mixtures was Type GU Portland cement. The fly ashes of class F and class CI conforming to the ASTM C618 (2012) were used. The chemical and physical properties of the Portland cement and fly ashes are presented in Table 3.4. For maintaining the strain hardening characteristic of the ECC mixtures, micro-silica, crushed and mortar sand were used with maximum aggregate sizes of 110 μm, 1.18 mm and 1.18 mm, respectively. The PVA fibers used for ECC mixes were 39 μm in diameter and 8 mm in length with a tensile strength capacity of 1600 MPa. For improvement of workability, the polycarboxylic-ether type high-range water-reducing admixture (HRWRA) with 30% of solid content was used for all 7 ECC mixtures.

Table 3.4: Physical and Chemical Properties of Portland cement, fly ash F and CI

Chemical Properties			
Compositions	Cement	Fly Ash F	Fly Ash CI
Sum ($SiO_2+Al_2O_3+Fe_2O_3$)	27.6	85.6	76.12
SiO_2 (%)	19.6	59.5	41.57
Al_2O_3 (%)	4.9	22.2	26.11
Fe_2O_3 (%)	3.1	3.9	8.44
CaO (%)	61.4	5.57	14.3
MgO (%)	3	-	3.4
SO_3 (%)	3.6	0.19	1.55
Alkalis as Na2O	0.7	2.75	0.71
Loss of Ignition (%)	2.3	0.21	1.49
Physical Properties			
Specific Gravity	3.15	2.18	2.43
Water Requirement (%)	-	93.4	95.9

3.3.2 Self-Consolidating Concrete

The self-consolidating concrete (SCC) was used as control mix (representing normal concrete) for construction of 1/4th scale link slabs, as well as the simply supported deck spans for the 1/6th scale full bridge model. The SCC was made with commercially available dry content (30 kg) pre-packaged bags. The dry content included the nominal aggregate size of 10 mm, Portland cement, silica fume and air-entraining admixtures. For each pre-package bag, a 2.4 liter of water was added for development of the SCC mixture.

3.3.3 Steel Girder

The supporting steel girder for the 1/4th scale link slab and 1/6th scale full bridge models was selected as W100 x19 section. The geometric shape and sectional properties of W100x19 section in accordance to CISC (2010) is presented in Figure 3.4 and Table 3.5.
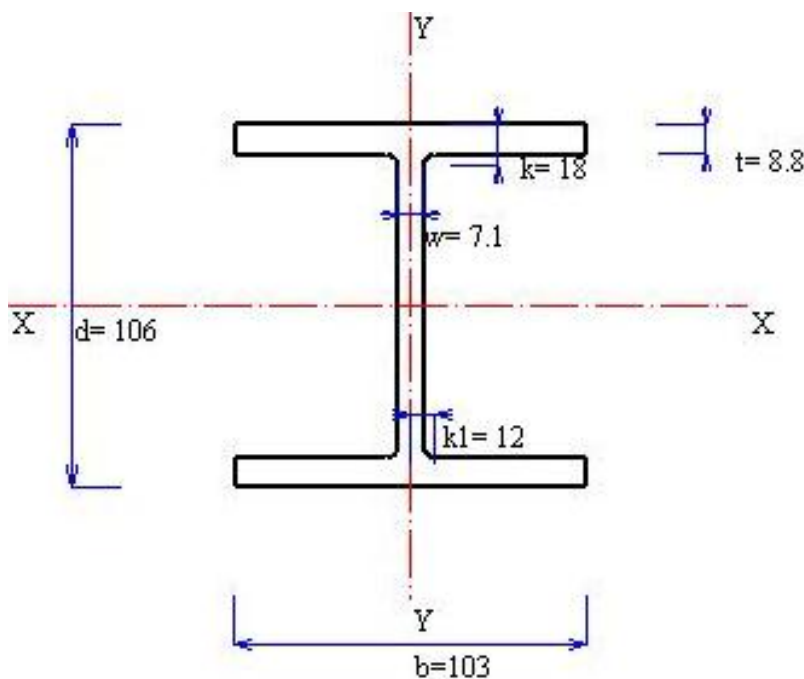
Figure 3.4: Schematic Representation of W100x19 Section as Girder

Table 3.5: Properties of W100x19 Structural Steel section

Section	Area	I_{x-x} 10^6mm^4	S_{x-x} 10^3mm^3	I_{y-y} 10^6mm^4	S_{y-y} 10^3mm^3	Depth mm	Flange Width mm	Flange Thickness mm	Web Thickness mm	Yielding Stress f_y MPa
W100x19	2480	4.77	89.9	1.61	31.2	106	103	8.8	7.1	345

3.3.4 Shear Stud Connector

The selected shear stud for the composite action of the steel girder and the concrete bridge decks was selected in accordance with CISC (2010). The yielding (f_y) and ultimate stress (F_u) of the shear stud were 350 MPa and 410 MPa, respectively. The schematic representation of the shear stud is presented in Figure 3.5.
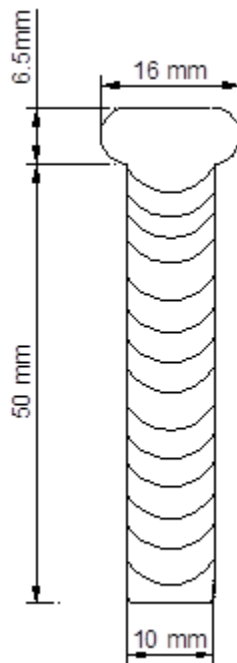
Figure 3.5: Schematic Representation of Shear Stud (Dimensions in mm)

35

3.4 Construction Model Specimens

This section presents the detail construction methodologies used for experimental investigation including: the production of SCC/ECC mixtures, casting and fabrication sequences of the specimens.

3.4.1 Mixing Sequences and Production of ECC and SCC

The seven ECC mixtures used in investigation were produced by using a Hobart Type mixer with 20-liter capacity. The weighted solid contents except for the PVA fibers were introduced into the mixture and mixed for 30 second. After that 90% of the water was added to the mixer and mixed for additional 2 minutes at a higher speed. Then the remaining water and HRWRA was introduced to the mix (mixed for 1 minute) for the development of a uniform and consistent mortar mixture. Lastly, the PVA fibers were added to the mortar for another 3 minutes of stirring until all fibers were dispersed with mortar mixture. The schematic representation of the mixing sequence is presented in Figure 3.6.

(a) Mixing of Solid Ingredients   (b) Water& HRWRA Addition   (c) PVA Fiber Addition
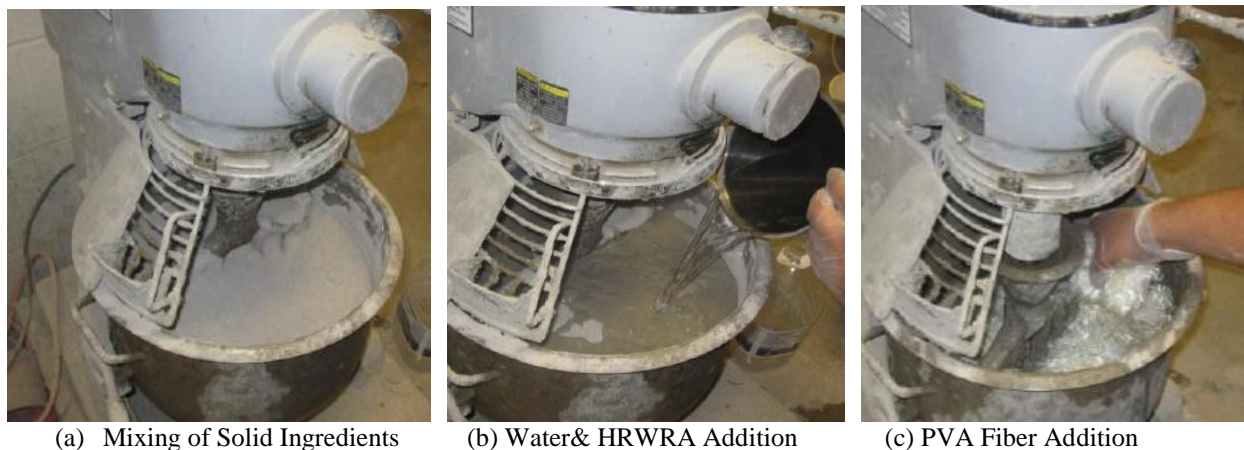
Figure 3.6: Mixing Sequences of ECC Mixtures

The 120-liter drum mixer was used for mixing SCC. The dry mix packages were introduced into the mixer for a dry 30 second mixing. After that 75% of the potable water was added to the dry contents for 2 minutes of mixing. The remaining 25% of the water was slowly added to the mix

for additional 2 minutes until the required flowability and workability was achieved. The schematic representation of the mixing sequences is presented in Figure 3.7

(a) Mixing Dry SCC Ingredient   (b) Water Addition

Figure 3.7: Mixing Sequences of SCC Mixture

3.4.2 Fabrication and Casting of Model Specimens

Long wooden boards were fastened together for preparing the deck slab of the 1/4th scale link slabs and 1/6th scale full bridge specimens. For each specimen, the wooden deck mold was clamped and locked into the two separate steel girders at 30 mm distanced apart. As a barrier for steel and concrete a 15-lb roofing paper was provided in the debonding zone of the link slab.

Similar to the general field practice, the bridge decks were cast initially with flowable SCC mix, and left for 24 hours for setting. Then the link slab segment was cast with ECC or SCC after initial 24 hours. At least three control specimens for each types of concrete in the form of cylinders, beams and cubes were also casted at the same time. All the specimens were cured for 28 days using wet burlaps in the laboratory conditions with a relative humidity and temperature of 50% $\pm$ 2.5% and 24 $\pm$ 2°C, respectively. The sequential casting process of the 1/4th scale link slab and 1/6th scale full bridge models are presented in Figures 3.8 and 3.9, respectively.

(a) Mold Preparation

(b) SCC Bridge Deck Casting

(c) Link Slab Casting

Figure 3.8: Casting Process of 1/4th Scale Link Slab Model

(a) Mold Preparation

(b) SCC Bridge Deck Casting

(C) ECC Link Slab Casting

Figure 3.9: Casting Sequence of Full Bridge Model

3.5 Test Set-Ups, Instrumentation and Testing Procedure

3.5.1 Strength Properties of Concretes

Performance of hardened SCC and ECC control mixtures were measured by mean compressive strength at the age of 28 days or at the testing of model link slab or full bridge specimens. For each concrete type at least 3 control specimens were casted and prepared for the testing. The compression test for cylindrical and cubic samples of SCC and ECC was performed as per ASTM C39 (2003), and ASTM C109 (2011).

The four-point bending test was performed on the ECC and SCC control prism specimen at 28 days or at the age of testing of link slab/bridge models in accordance to ASTM C78 (2010). Prior to testing, all the prism specimens were sanded for obtaining a flat surface. The four-point bending test was performed using a closed-loop controlled servo-hydraulic system under displacement condition at a loading rate of 0.005 mm/s. The load and mid-span deflection were recorded on a computerized data acquisition system. The total span length of the flexural specimens was 304.8mm.

3.5.2 One Fourth Scale Link Slab Subjected to Monotonic Loading

All nine link slab specimens were tested under monotonic loading at the age of 28 days for demonstrating the actual loading and support conditions of the real bridge structure. The inflection points spanning 810 mm were simulated by the pin and roller supports. For practical purpose, the link slab was tested in an inverted orientation for simulating actual link slab behaviour in a joint-free bridge deck. Prior to testing, strain gauges were installed at the mid-span location for recording and monitoring the rebar tensile strain and concrete tensile/compressive strains during loading up to failure. Linear variable displacement transformers (LVDTs) were located at different locations for recording and monitoring the deflections. Inclinometer was installed at the support location for recording the support-end rotation. Detailed schematic representation of the link slab test set-ups, including location of the strain gauges, LVDT's and inclinometer are presented in Figure 3.10.
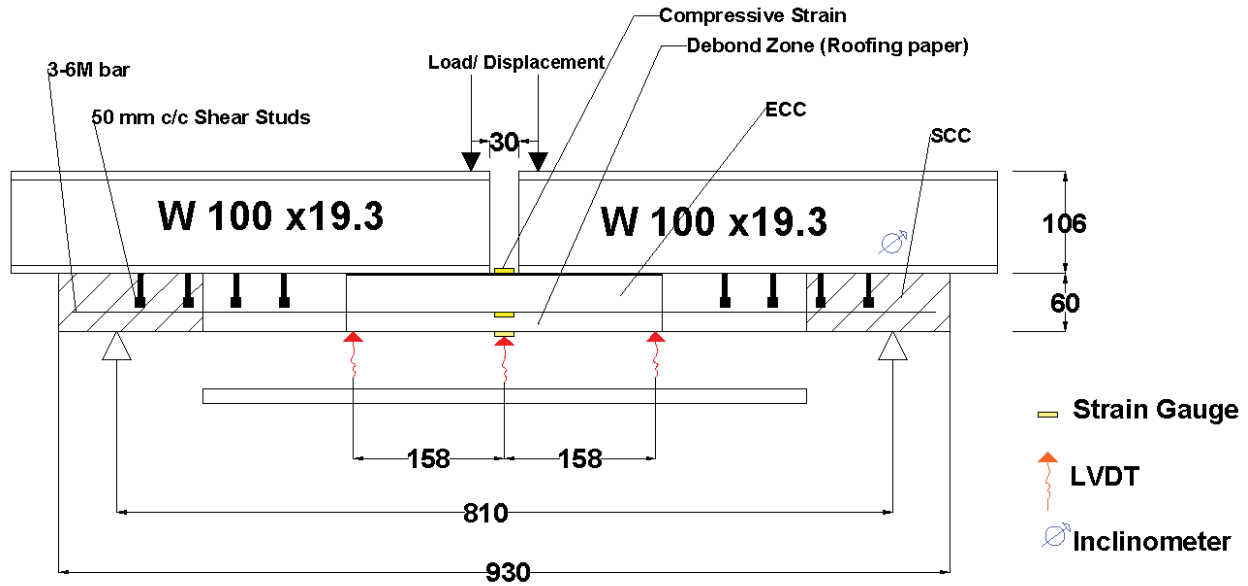
Figure 3.10: Monotonic Test Set-Ups for 1/4th Scale Link Slab Specimen (Dimensions in mm)

Same testing procedure was adopted for all nine link slab specimens incorporating different concrete mixtures. The monotonic testing was performed using a closed-loop controlled servo-hydraulic system under displacement condition at loading rate of 0.005 mm/s. The loading was continued to post-peak failure, up to 85% of the ultimate load for determination of the post-peak ductility and energy absorbing capacity. While the load and mid-span deflection were recorded by the MTS machine, additional data acquisition system was used for recording the strain developments, deformation through LVDTs and support-rotation. The crack propagation and failure modes were visually observed and recorded during the test. The crack's width was measured using the crackscope. Figure 3.11 represents the testing instrumentation of the 1/4th scale link slab specimen.
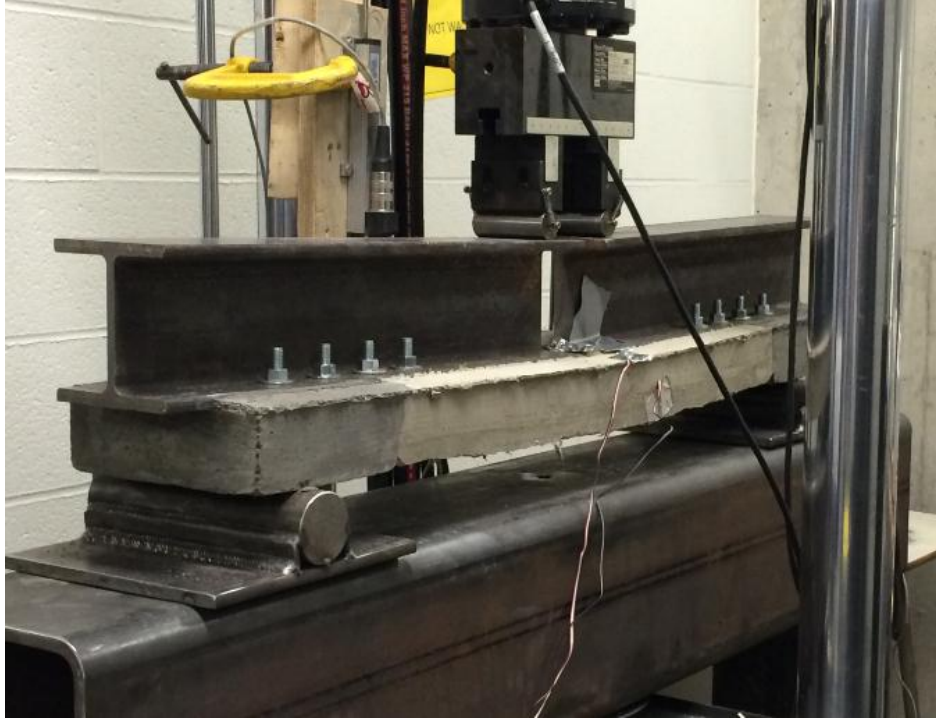
Figure 3.11: Testing and Instrumentation of 1/4th Scale Link Slab Specimen

3.5.3 One Fourth Scale Link Slab Subjected to Flexural Fatigue Loading

Flexural fatigue tests were performed to investigate the cyclic behavior of the 1/4th scale ECC link slab compared with the control SCC link slabs. Overall three ECC and one SCC link slabs were prepared and tested at the age of 28 days. The flexural fatigue testing was performed in three different stages: pre-fatigue behaviour under monotonic loading to failure, fatigue behaviour under cyclic loading at different stress levels and post-fatigue behaviour under monotonic loading to failure. The pre-fatigue monotonic test was performed to evaluate the ultimate strength, bending capacity and strain development of the link slabs and also to determine the applicable fatigue stress levels. After the analysis of the pre-fatigue monotonic testing, the flexural fatigue loading was performed on companion link slab specimens based on two different approaches. The first approach applied different fatigue stress levels of 40% and 55% of the ultimate load (determined from pre-fatigue monotonic testing) at a constant 400000 fatigue cycles. The second approach applied constant fatigue stress level of 40% at 4Hz cyclic loading rate (4 cycles per second) with variable fatigue cycles of 400000 and 1000000. After the fatigue performance, the flexural monotonic test was performed on the exhausted fatigued link slab specimens for determining the residual strength and bending capacity.

42

For both pre-fatigue and post-fatigue monotonic performance, same testing procedure and instrumentation as used for the 1/4th scale link slab subjected to monotonic loading were adopted (section 3.5.2 and Figure 3.10).

Flexural fatigue testing for both approaches was performed using a closed-loop controlled servo-hydraulic system. The specimens were pre-monotonically loaded to the mean fatigue stress levels of 40% and 55% under load control condition, at a rate of 0.5 kN/min as a ramp into fatigue loading. Then fatigue loading was applied with an upper and lower limit of ±20% of the applied mean stress level until the end of the fatigue cycles (400000 and 1 million cycle). During the fatigue flexural tests, the mid-span deflection and deflection evolutions were recorded by the system. Additional data acquisition system was used for recording the maximum concrete (tensile/compressive) and rebar strain developments at the mid-span location (Same instrumentation as Figure 3.10). The crack propagation was visually observed and recorded for every 10000 fatigue cycles.

3.5.4 One Sixth Scale Full Bridge Subjected to Monotonic Loading

The full bridge specimen was tested under monotonic loading at the age of 28 days for simulating a reduced scale real bridge structure with connecting ECC link slab. Prior to testing, strain gauges were installed at mid-span location of the SCC spans (where maximum positive bending moment expected) and center of the ECC link slab specimens (where maximum negative moment was expected) for recording the maximum concrete compressive/tensile strain and rebar strains. Additional strain gauges were installed at the location of the inflection points for verification of the location of inflection points as per design guide by Lepech and Li (2009). LVDTs were provided at different locations for measuring the deflection of composite girders and link slab. The inclinometer was installed on the inner support (ECC and SCC interface) for measuring the rotation developed by the ECC link slab. The detailed representation of the experimental devices used for monitoring the full bridge model during testing is presented in Figure 3.12.
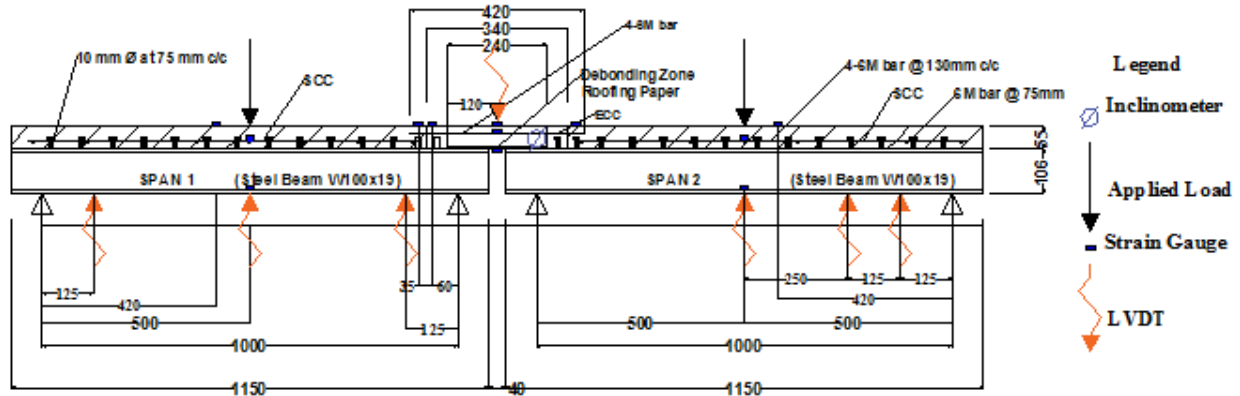
Figure 3.12: Monotonic Test Set-Ups for 1/6th Scale Full Bridge Model (dimensions in mm)

The monotonic testing was performed using a hydraulic actuator system under load control condition at a loading rate of approximately 3 kN/min. The loading was applied at the centre of the SCC simply supporting deck (centre of each of the composite girder) where maximum positive bending moment was expected (Figure 3.12). The applied loading was selected up to service stage load, determined as 50% of the design load calculated prior to the testing based on the resistance of composite section as per CHBDC (2006) and Lepech and Li (2009) as illustrated in Appendix A.

A data acquisition system was used for recording the load, deflection, strain development and the ECC support end-rotation for the 1/6th scale full bridge model at critical locations (Figure 3.12). The testing and instrumentation of the 1/6th scale full bridge model is presented in Figure 3.13.

Figure 3.13: Testing Instrumentation of 1/6th Scale Full Bridge Model

3.6 Summary

This chapter described the experimental investigations on 1/4th scale link slab models and 1/6th scale full bridge model made with SCC and ECC. The detailed design guidelines and geometric dimensioning of the test specimens (link slabs and full bridge) are presented along with test procedures, instrumentation and testing under monotonic and fatigue flexure loading.

CHAPTER FOUR

STRUCTURAL PERFORMANCE OF LINK SLABS UNDER MONOTONIC LOADING

4.1 Introduction

This Chapter presents the results of the experimental investigation on 1/4th scale link slab specimens subjected to monotonic loadings. The performance is described based on the load-deflection/moment-rotation response, strain developments, cracking/crack propagation, energy absorption, ductility and failure modes. The influence of seven ECC mix types (based on fly ash types CI and F and the replacement percent 55% and 70%) and aggregate types/size (local mortar/crushed sand and silica sand) on the link slab structural performance under monotonic loading is described compared to those made with a self-consolidating concrete (SCC). In addition, results of a test conducted on 1/6th scale full bridge with ECC link slab tested under monotonic loading (up to service stage – 50% of the design load) is described based on load-deflection/moment-rotation response and strain development (in steel rebar, concrete and steel I-beam) as well as inflection point identification. The moment resistance of link slab is compared with those obtained from theoretical analyses. In addition, experimentally obtained location of inflection points is compared with those suggested by design specifications.

The properties of ECC and SCC mixtures such as compressive/flexural strengths and bending deflection capacity are also presented.

4.2 Properties of ECC and SCC mixtures

The 28 days compressive and flexural strength including mid-span deflection at ultimate load for the seven ECC and one SCC mixtures (mean value of at least three cylinder/beam specimens) are presented in Table 4.1

Table 4.1: Compressive and Flexural Strength of ECC and SCC Mixes

Mix No.	Designation	Compressive Strength (MPa)	Flexural Strength (MPa)	Mid-Span Deflection (mm)
1	LS2-ECC-CI-1.2-SS	52.14 ± 8.11	5.13 ± 0.07	2.24
2	LS3-ECC-F-2.2-SS	45.19 ± 1.30	6.56 ± 0.25	2.93
3	LS4-ECC-F-1.2-SS	47.55 ± 1.51	10.13 ± 1.61	2.52
4	LS6-ECC-F-2.2-CS	50.15 ±8.02	10.25 ± 3.04	4.13
5	LS10-ECC-CI-2.2-SS	53.79 ± 1.79	7.36 ± 0.46	5.83
6	LS11-ECC-CI-2.2-CS	57.34 ± 0.19	5.03 ± 0.75	3.61
7	LS28-ECC-CI-1.2-MS	55.5 ± 6.70	11.07 ± 1.76	1.22
8	LS25-SCC	45±2.51	4.95±0.81	0.65
9	LS32-SCC	36.4 ± 1.38	4.06 ± 0.24	0.65

The 28 days compressive strength of ECC made with class CI-FA was higher in compare with class F-FA at the same FA replacement. The higher content of Calcium Oxide (CaO) in FA-CI promotes higher and denser hydration products resulting stronger bonds in interfacial transition Zone (ITZ) and higher compressive strength (Alexander et al. 2003). Also the 28 days compressive strength of the ECC mixes reduced at higher SCM replacement rate specifically for class F-FA. This can be attributed to the lower content CaO and slower hydration rates which resulted in an increased porosity levels between the formed hydration products (Sahmaran et al. 2008).

At each SCM replacement level, the ECC mixes with micro-silica sand yielded lower compressive strength in compare with the mortar and crushed sand. It is observed that the compressive strength of the ECC mixes similarly to the normal concrete are dependent on the maximum aggregate size. The maximum aggregate size for micro-silica sand for these ECC mixes were 0.3 mm while for crushed and mortar sands were 1.18 mm. The increased maximum aggregate size promotes higher water content in the ITZ, which increases the volume of the paste and the aggregate at stronger bonding (Mehta & Monteiro, 2006). Therefore the 28 days compressive strength for the ECC mixes with crushed and mortar sands were higher in compare with the micro-silica sand.

Even though there are variation for the 28 days compressive strength of the proposed ECC mixes, yet the minimum compressive strength of 45 MPa exceeds the strength of the SCC and fulfills the engineering requirements specifically for bridge deck applications.

The flexural strength for all mixes varied from 4.06 to 11.07 MPa and the mid-span deflection varied from 0.65 to 5.83 mm. SCC has shown lower flexural strength of 4.06 MPa and mid-span deflection of 0.65 mm compared with the ECC specimens. The SCC specimen exhibited a brittle failure after the formation of first crack whereas ECC specimens undergone tensile strain hardening by increasing the load and deflection. The strain hardening behaviour of the ECC is attained by fiber bridging phenomena where the PVA fiber is ruptured to its full strength rather than a pull-out like steel fibers (Li et al. 2001).

The test results showed that increased in FA content improved the bending capacity of the ECC mixes while the flexural strength was reduced. The presence of un-hydrated fly ash particles that acts as filling materials results as densification of ITZ and improvement of the frictional bonding between the PVA fiber and the matrix (Hossain & Sherir, 2014; Yang et al. 2007; Wang & Li, 2007). However the reduction of the chemical bonding and the toughness of the matrix results as a reduction of the flexural strength.

The increased in maximum aggregate size (MAS) of the sand for the ECC mixes increased the flexural strength while reduced the mid-span deflection. The improved flexural strength resulted from higher degree of aggregate interlocking that enhanced the matrix toughness and work of fracture (Sahmaran et al. 2009). However increased in MAS caused the balling effect of the PVA fibers, preventing them for the adequate coverage of the cement paste and causing the non-uniformity dispersions of the fibers that resulted as reduction of the bending capacity (Hossain & Sherir, 2014).

4.3 Structural Performance of 1/4th Scale Link Slabs with Different ECC Mixes Subjected to Monotonic Loading

The structural performance of the 1/4th scale link slabs made with seven ECC mixtures and one SCC mix subjected to monotonic loading is described and compared.

4.3.1 Experimental Load-Deflection/Moment-Rotation Responses and Theoretical-Code Based Analysis

Table 4.2 summarizes the test results. The typical load-deflection and moment-rotation curves for all the link slab specimens are represented in Figures 4.1 and 4.2. Table 4.2 shows that the ultimate load for various ECC and SCC mixes varied from 5.94 to 12.16 kN, and mid-span deflection at ultimate load varied from 6.75 to 12.22 mm. The first cracking load for the ECC mixes did not differ drastically, whereas the mid-span deflection varied from 1.41 to 4.6 mm.

Table 4.2: Summary of Load-Deflection and Moment Rotation Responses

Link slab Designation	Ultimate Load kN	Ultimate Deflection mm	Load (1st crack) kN	Deflection (1st crack) mm	Ultimate Rotation radian	Ultimate Moment kN.m	Theoretical Moment kN.m (Eq.2.15)
-ECC-CI-1.2-SS	9.89	10.45	3.25	2.01	0.0351	1.88	1.29
LS3-ECC-F-2.2-SS	10.51	12.22	3.25	1.89	0.0285	2.00	1.29
LS4-ECC-F-1.2-SS	10.4	9.39	3.5	1.63	0.0301	1.98	1.29
LS6-ECC-F-2.2-CS	10.94	11.44	3.25	1.76	0.0278	2.08	1.29
LS10-ECC-CI-2.2-SS	8.79	11.61	3.25	3.09	0.0444	1.67	1.29
LS11-ECC-CI-2.2-CS	10.04	12.04	3.5	2.91	0.0445	1.91	1.29
LS28-ECC-CI-1.2-MS	12.16	7.60	3.10	1.41	0.0206	2.31	1.29
LS25-SCC	6.54	14.7	4.86	0.9	0.0383	1.26	1.25
LS32-SCC	5.94	6.75	5.13	4.6	0.0222	1.28	1.25

Note: The theoretical moments for ECC are determined based on Eq.2.15
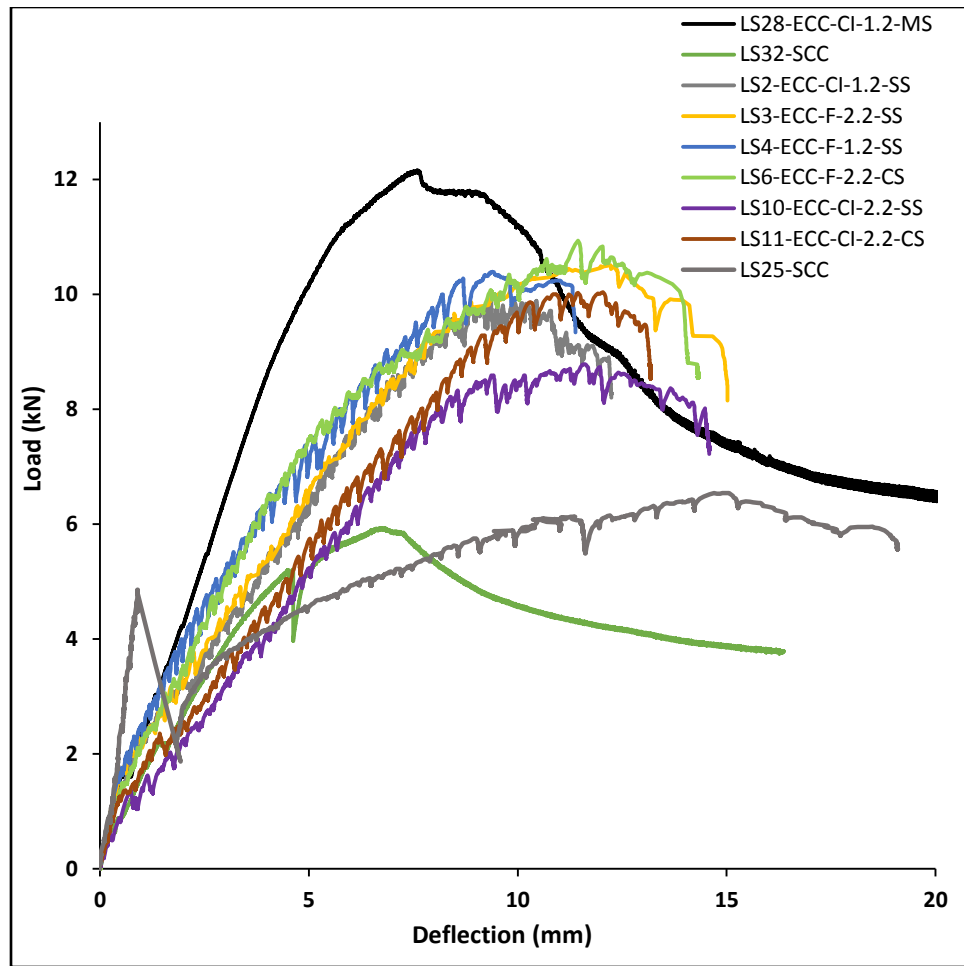
Figure 4.1: Comparison of Load-Deflection Response of Different Concrete Mixes
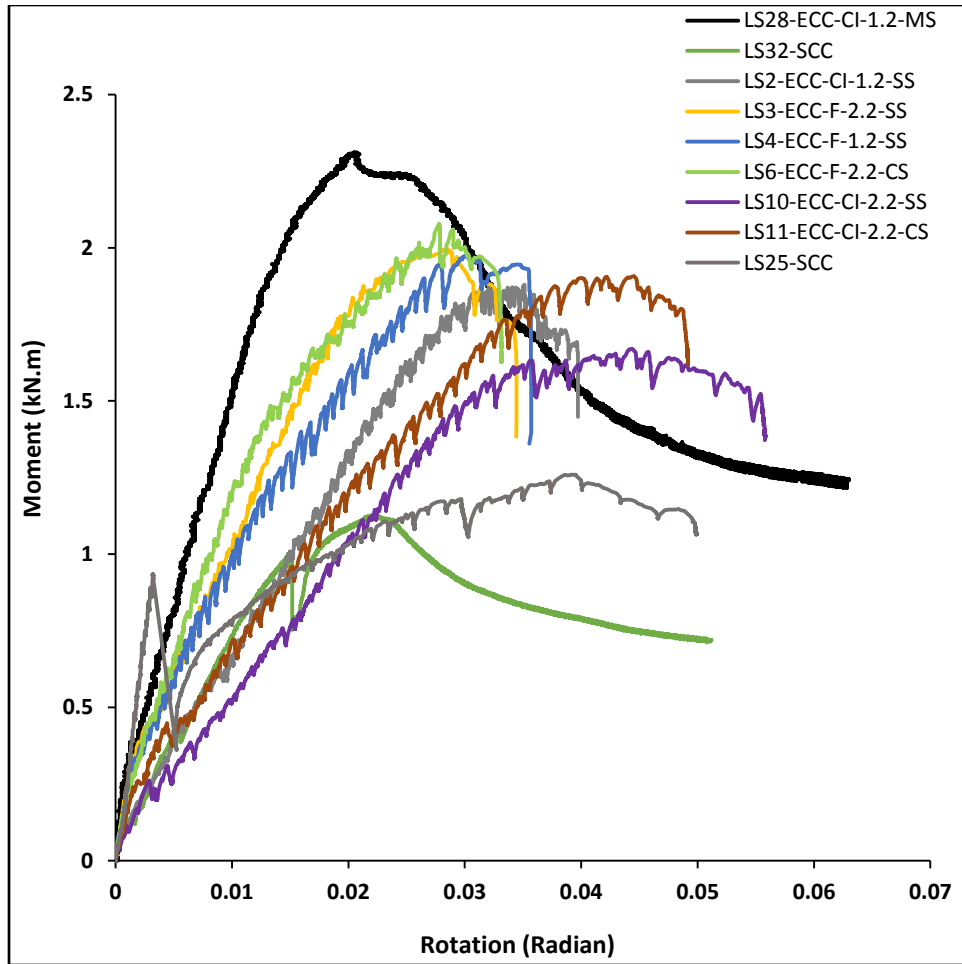
Figure 4.2: Comparison of Moment-Rotation Responses of Different Concrete Mixes

4.3.1.1 Performance of ECC and SCC Link Slab

The comparative load-deflection and moment-rotation responses for the ECC and SCC link slabs are presented in Figures 4.3.

(a)Load-Deflection Response　　　　　(b) Moment-Rotation Response
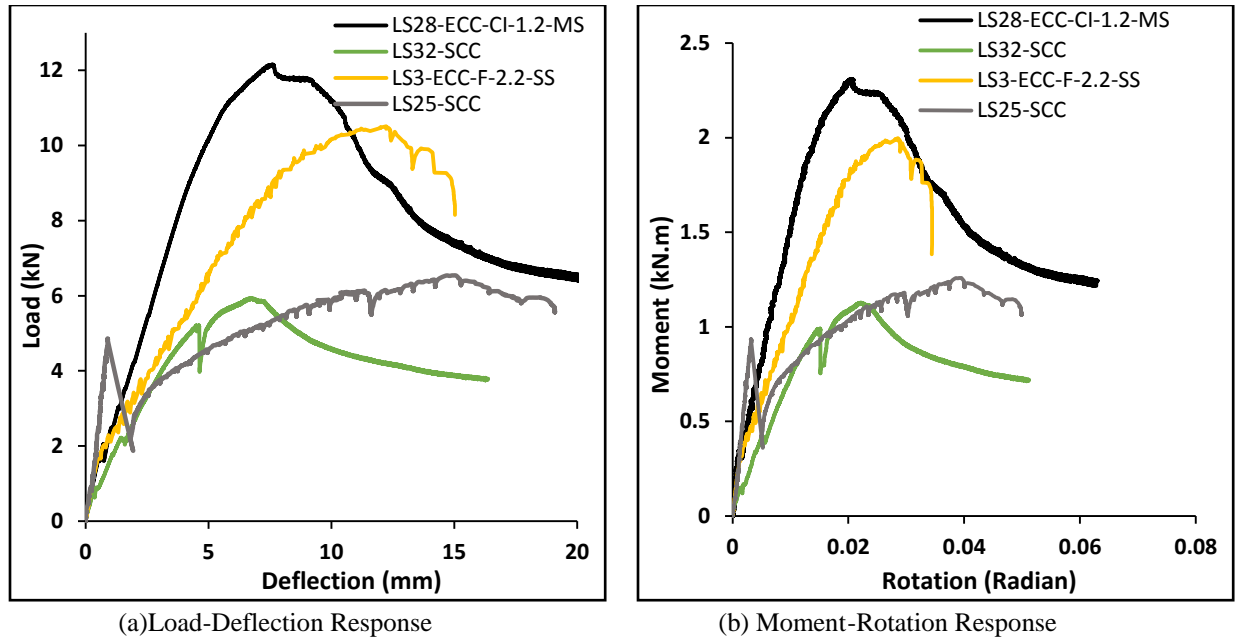
Figure 4.3: Comparison of Load-Deflection and Moment-Rotation Response of ECC and SCC

Link Slabs

As it is seen from Figure 4.3 that there is a significant difference between load-deflection responses of ECC and SCC link slabs. For all ECC link slabs, a steady increase in deflection was evidenced when the applied loading was increased. This proves that all ECC link slabs clearly defined the ductility and strain hardening behaviour without the aid of the reinforcing bars. Unlike ECC, SCC link slab experienced a sudden drop of load when the first crack was formed. This pattern demonstrates the brittle response of the SCC at the first crack where load is transferred to the steel bar and as result load increased again before failure - through the SCC and steel bond mechanism the second peak/ ultimate loading was achieved.

The moment-rotation responses showed similar patterns of load-deflections for the ECC and SCC link slabs. The ultimate moment capacity for all ECC link slab was higher compared to SCC link slabs. As it is observed from Table 4.2, the theoretical moment capacity of the ECC link slabs calculated by the Equation. 2.15 proposed by Lepech & Li (2009) are underestimated compared with the experimental moments. This is attributed to the conservative assumption of the tensile capacity and strain hardening behaviour of the ECC. Also additional factors related to mix design parameters, fiber bridging, multi-cracking characteristics and PVA fiber-matrix

interaction were not properly taken into account. Unlike ECC, the theoretical moment capacity of the SCC was very close to its experimental value.

4.3.1.2 Influence of Fly Ash on Link Slab Behaviour

The increase in FA replacement with cement (55% to 70% or 1.2 to 2.2) for both class CI and F did not show a significant influence on the ultimate load. However, it is evidenced from Figure 4.4 that the increase in both types of FA replacement increased the mid-span deflection and improved the bending capacity of link slab. The increase in FA replacement resulted in the reduction of the chemical bonding and toughness among the PVA fibers and matrix yet improved the interfacial frictional bonding in order to achieve higher deflection and bending capacity (Wang & Li, 2007; Sahmaran et al. 2008). The increased deflection and bending capacity (lower rotational stiffness) of the link slabs also improves the function of the joint-free bridge decks since it will allow the simply supported adjacent spans to deflect freely and separately from each other, rather than the formation of continuous stiff bridge spans (Lepech & Li, 2009).
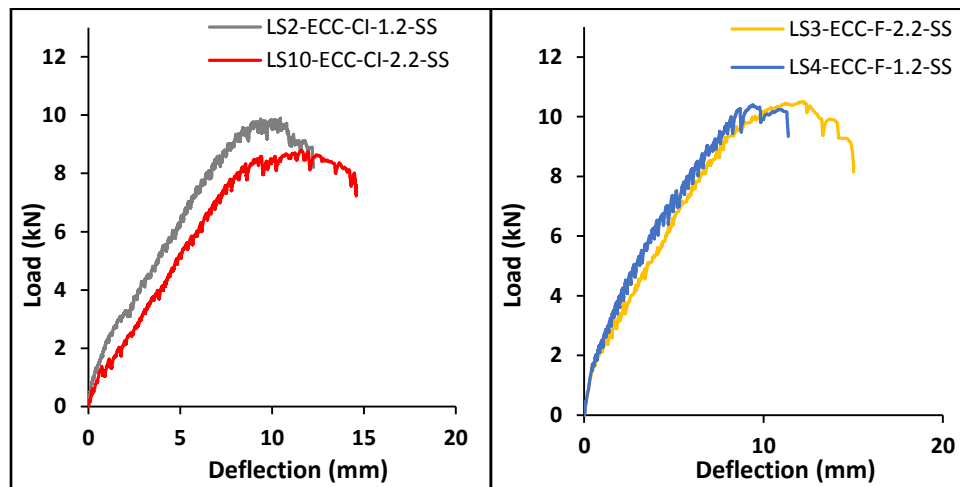
Figure 4.4: Load-Deflection Responses for ECC mixes with variable FA Replacement

4.3.1.3 Influence of Different Aggregate Sizes

As it can be observed from Figure 4.5, the use of ECC made with larger aggregate size (CS or MS has larger aggregate size than SS) improved the ultimate load capacity of link slab but reduced the mid-span deflection capacity, specifically for LS28-ECC-CI-1.2-MS. The larger aggregate size produced higher degree of aggregate interlocking which improved the load

capacity of the link slabs as observed for specimen LS28-ECC-CI-1.2-MS as suggested by Sahmaran et al. (2009). In addition, the increased ball size of the aggregates for crushed and mortar sand prevented the fibers to be coated with the matrix, which attributed to the reduction of the fiber-matrix frictional bonding and lower deflection/bending capacity (Sahmaran et al. 2009). Although the ultimate loading capacity is increased, the lower deflection and bending capacity may decrease the ductility (flexibility) of the link slabs - leading to the formation of continuous stiff bridge deck with lower rotation capacity of the simply supported adjacent spans connected by link slabs (Lepech & Li, 2009). However, ECC made with mortar sand and crushed sand in combination with class F or CI fly ash showed better flexure fatigue performance producing lower damage in terms of displacement evolution (Sherir, 2012) and suggested to be more suitable for link slab applications.
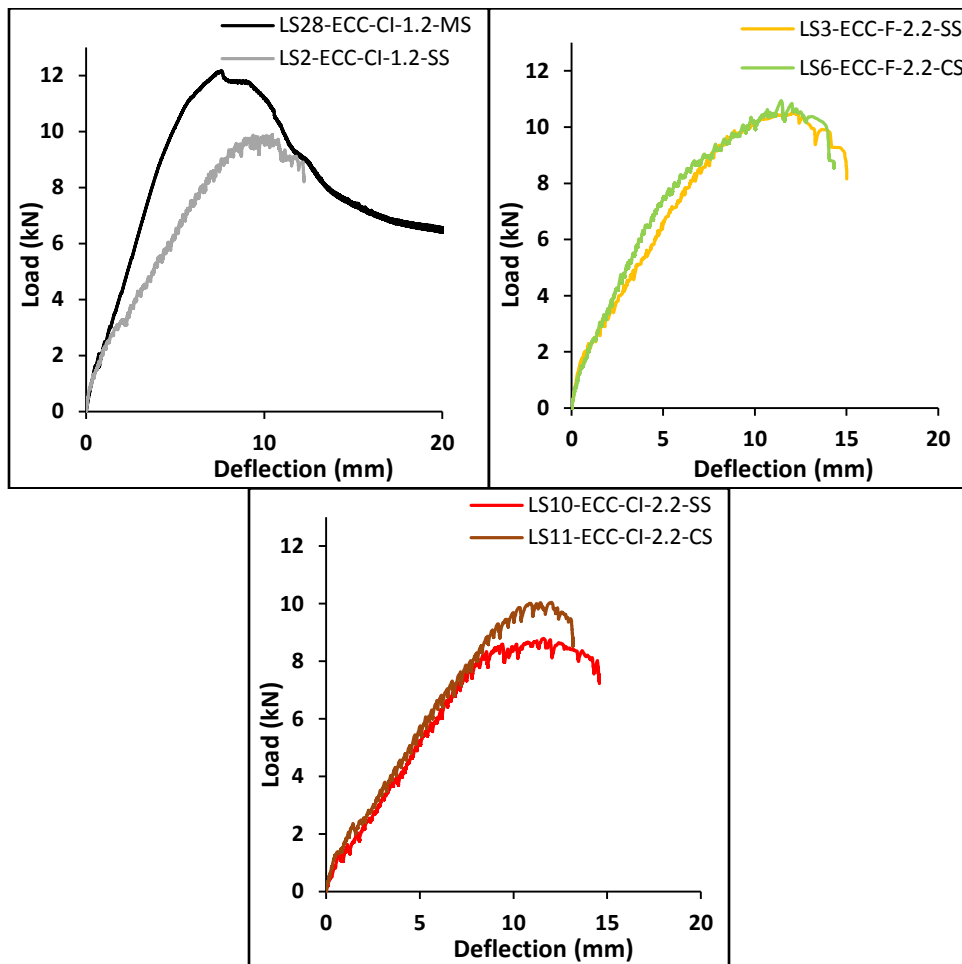
Figure 4.5: Load-Deflection Responses for ECC mixes with Different Sand Size

54

4.3.2 Strain Development

Concrete tensile/compressive and rebar strain developments for the seven ECC and two SCC link slabs at ultimate loading are summarized in Table 4.3 and Figures 4.6 and 4.7 respectively.

Table 4.3: Summary of Strain Development for Different Link Slabs

Designation	Ultimate/peak Load (kN)	Concrete Tensile Strain at peak load (Micro-Strain)	Rebar Strain at peak load (Micro-Strain)	Concrete Compressive Strain at peak load (Micro-Strain)	Load at Rebar yield (kN)
LS2-ECC-CI-1.2-SS	9.89	No reading	2646	-2396.0	8.3
LS3-ECC-F-2.2-SS	10.51	1803	1297	-3863.0	Not Yielded
LS4-ECC-F-1.2-SS	10.4	5656	1974	-3073.0	9.49
LS6-ECC-F-2.2-CS	10.94	8560	1631	-3765.0	Not Yielded
LS10-ECC-CI-2.2-SS	8.79	No reading	No reading	-1290.0	Not Yielded
LS11-ECC-CI-2.2-CS	10.04	2267	70 (strain gauge damaged)	-2492.0	Not Yielded
LS28-ECC-CI-1.2-MS	12.16	5106	3172	-1481.0	9.17
LS25-SCC	6.54	146 (at 4.3kN)	2465	-4395	5.66
LS32-SCC	5.94	No reading	2723.36	-783.1	4.41
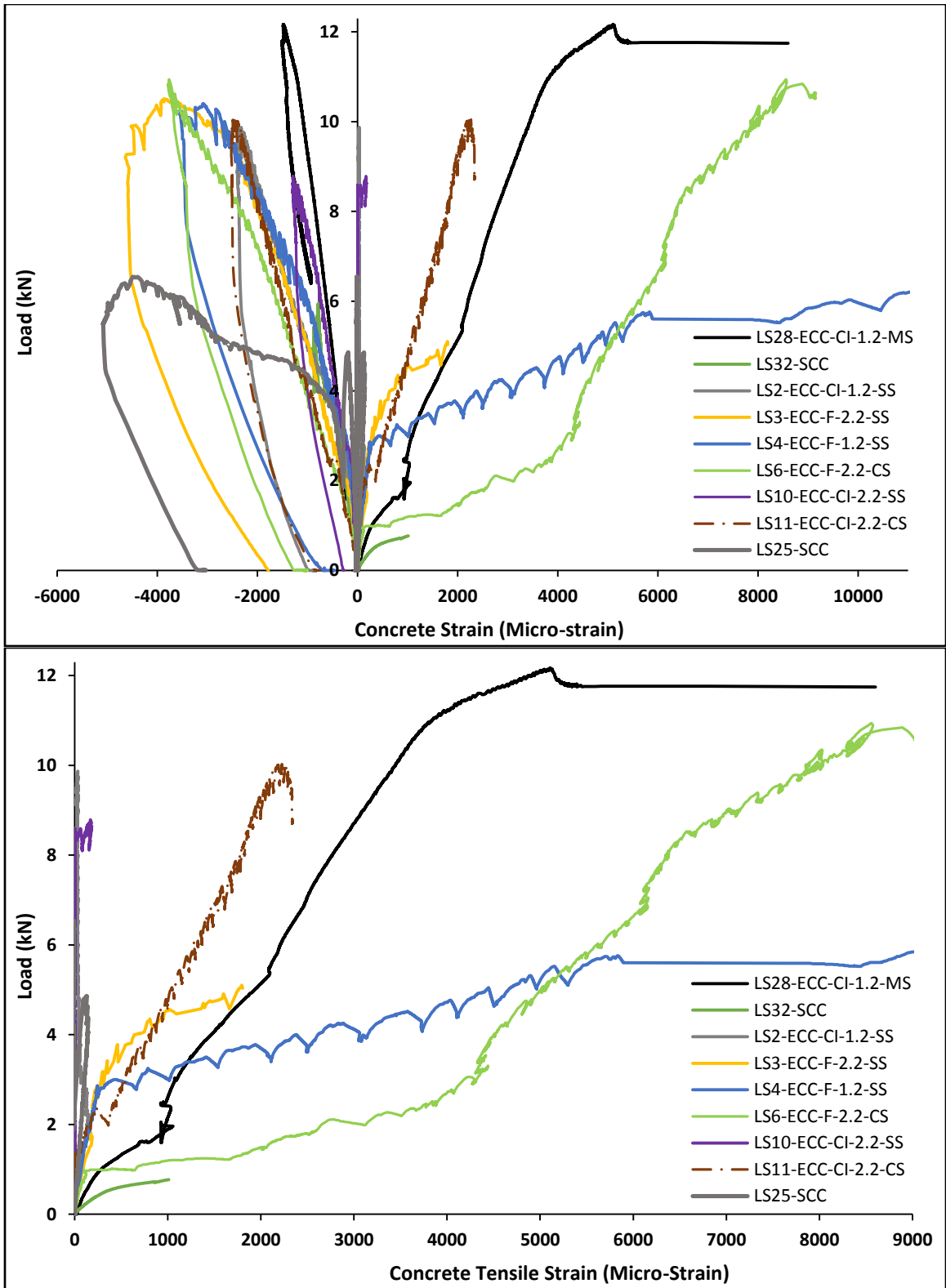
Figure 4.6: Concrete Strain Developments for Different Concrete Mixes
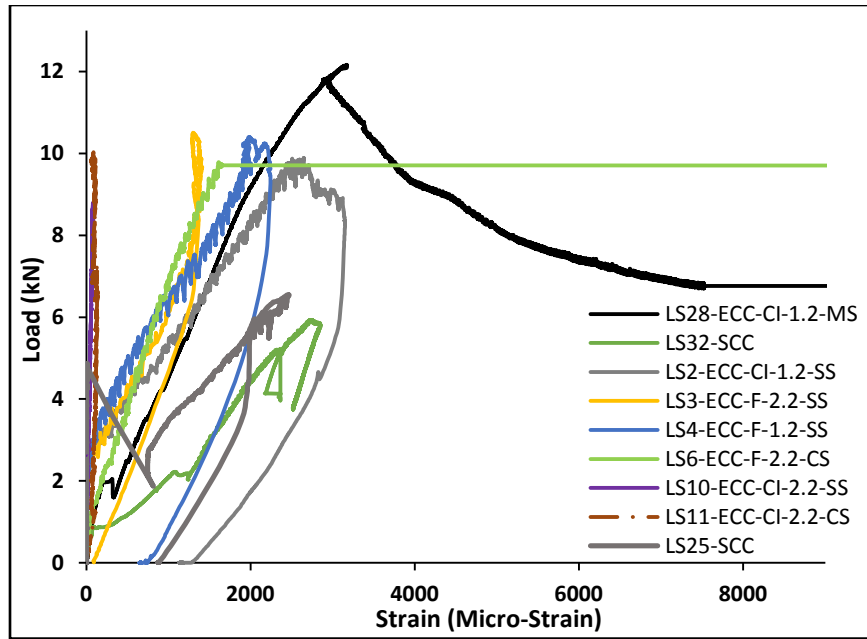
Figure 4.7: Rebar Strain Developments for Different Concrete Mixes

4.3.2.1 Performance of ECC and SCC Link Slab

Typical load-strain curves for the ECC and SCC link slabs are presented in Figure 4.8 to differentiate the concrete and rebar strain development among ECC and SCC.
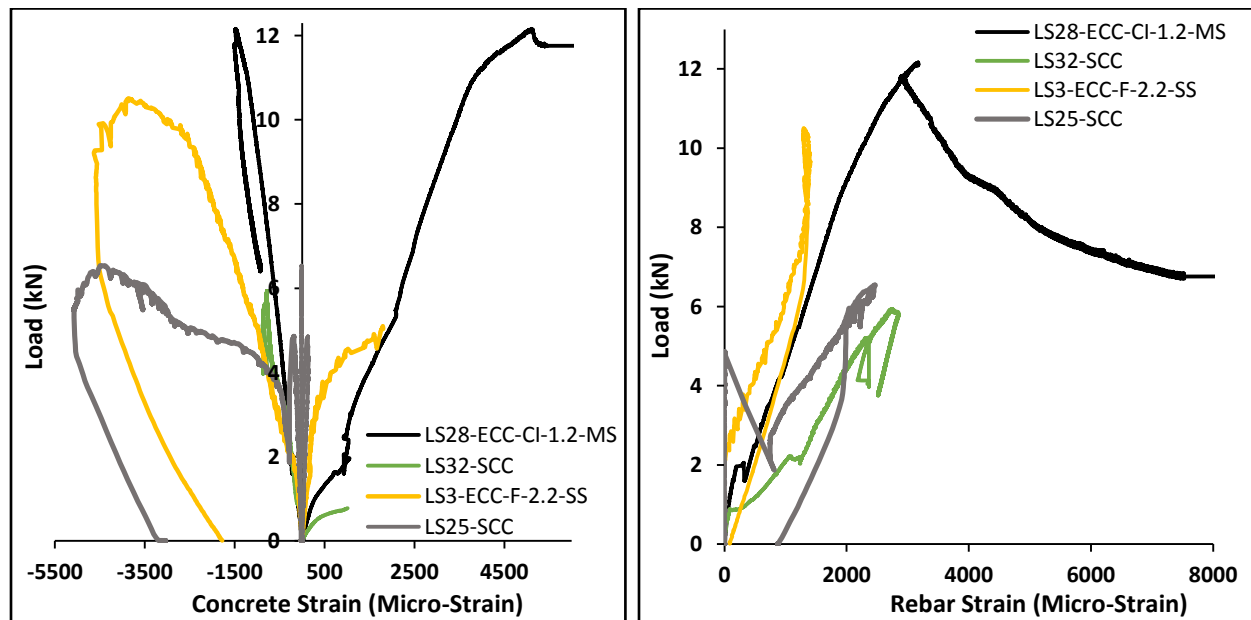
(a)Concrete Tensile Strain Development

(b) Rebar Strain Development

Figure 4.8: Strain Developments for ECC and SCC Link Slabs

57

As it is observed from Table 4.3 and Figure 4.8, the concrete tensile/compressive strains for all ECC link slabs were much higher than SCC links slabs reached the yielding stage at the ultimate loading, except for LS2-ECC-CI-1.2-SS and LS10-ECC-CI-2.2-SS where the stain gauges broke during test. The rebar strain development was also lower in ECC link slabs and yielding of the rebar occurred at higher load. This can be attributed to the fiber bridging and micro-cracking characteristics where at onset of cracking, load is gradually transferred to the steel bar. In SCC link slabs, at the formation of a major crack, load was transferred to the rebar suddenly causing them to be highly stressed and subsequently yield at lower load. Hence, after the formation of the crack ECC's tensile strain increased gradually unlike SCC where all the tensile stresses were transferred to the steel rebar. The increased tensile strain in ECC is caused by the fiber bridging phenomena where PVA fiber is ruptured to its ultimate tensile strength capacity rather than a pull out (Li et al. 2001). The lower bond stresses are formed between the steel rebar and ECC matrix due to the less confinement effect of the PVA fibers that eliminates the shear lag effect (Fischer & Li, 2002; Hossain & Anwar, 2014). Therefore the unified combination of ECC's tensile and steel rebar strain cause a high ductility, increase ultimate load and high energy absorption for all ECC's link slabs.

4.3.2.2 Influence of Different Fly Ash Replacement on Strain Development

Increase in FA content improves the tensile strain capacity of the concrete. However, this is not evident from the concrete strain development in Figure 4.9. It should be noted that due to the sensitivity of the strain gauges and breakage at earlier stage of the test, the results for the concrete tensile strain of LS3-ECC-F-2.2- might not be precise. However by observing the lower rebar strain for LS3-ECC-F-2.2-SS in compare with LS4-ECC-F-1.2-SS, it is evidenced that higher concrete tensile strain was developed at higher FA replacement rate. The higher rebar tensile strain development is also attributed to lower tensile strength of ECC with high volume of fly ash as a result of transfer of load to the rebar due to earlier crack development. The increase in FA replacement rate enhanced the interfacial frictional bonding while reducing the matrix toughness and chemical bonding among the fiber and matrix. This property attributes to the increased long term tensile ductility of ECC by 3% as reported by Wang & Li (2007).
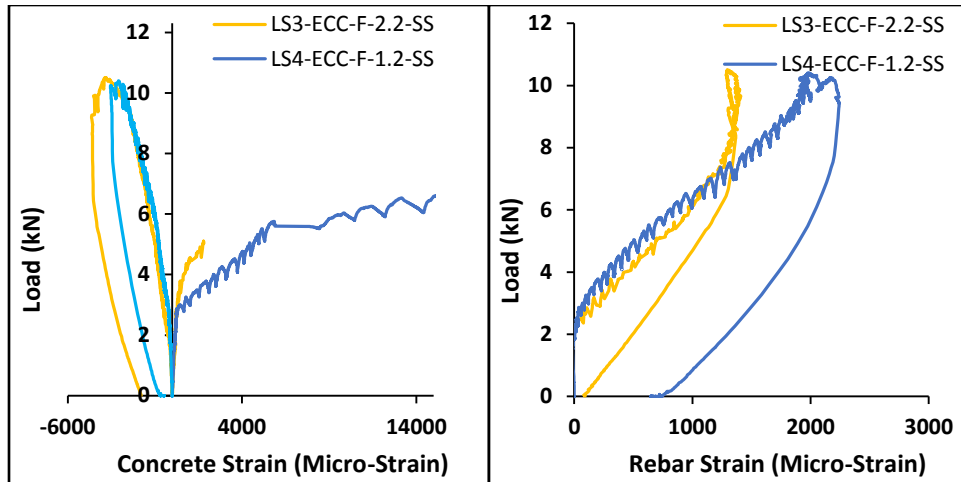
Figure 4.9: Concrete and Rebar Strain Development for ECC with Different FA Replacement

4.3.2.3 Different Aggregate Size

ECC mixes with CS (larger aggregate sizes) developed higher strain compared to SS (lower aggregate size). The contribution of the aggregate interlocking for larger maximum of the crushed and mortar sand aggregate size may have increased the tensile strain capacity of the ECC link slabs (Hossain & Anwar, 2014).
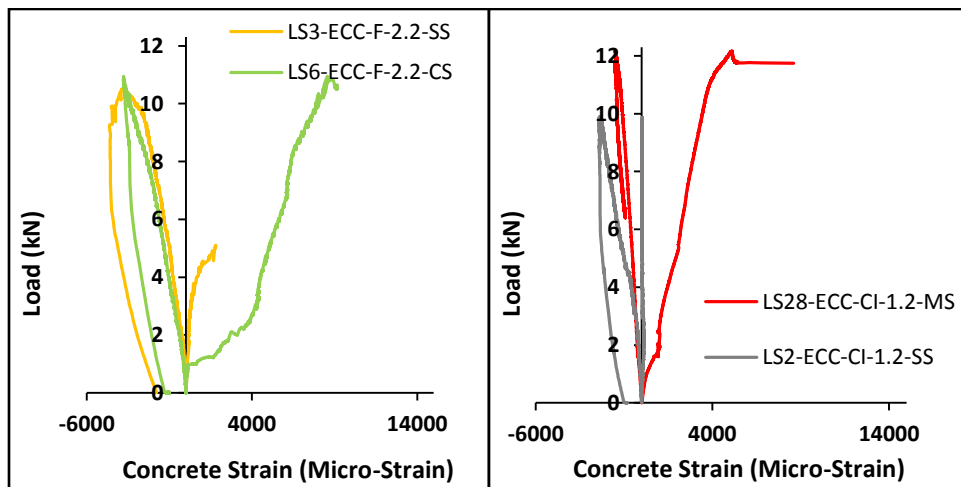
Figure 4.10: Concrete Strains Development for ECC Link Slabs with Different Sand Sizes

59
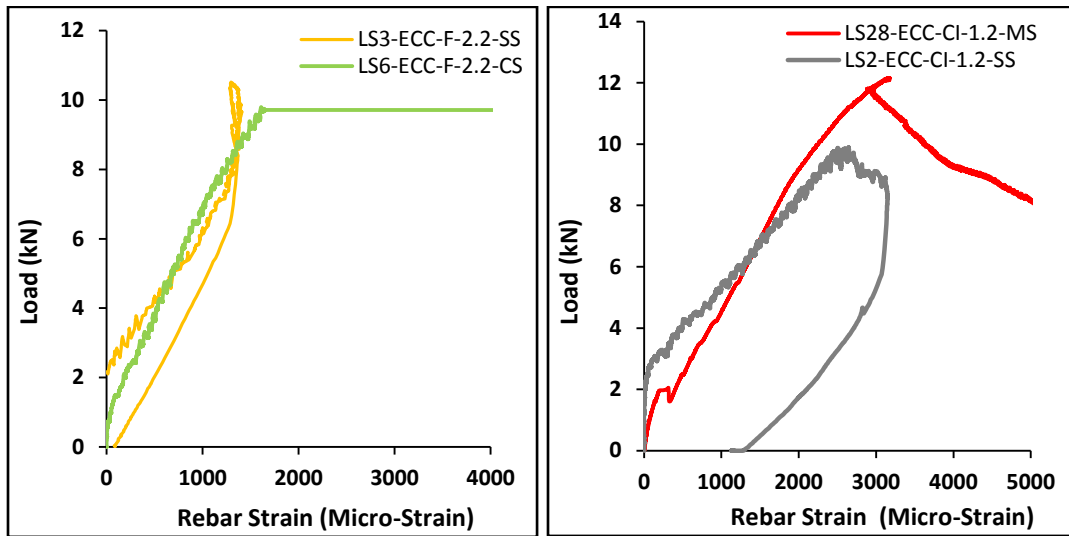
Figure 4.11: Rebar Strain Developments for ECC Link Slabs with Different Sand Sizes

4.3.3 Crack Characterization

The cracks for all ECC and SCC link slabs were formed at the tension faces and were extended across the entire slab width indicating flexural behavior. For all link slabs the cracks were developed only in the debonding zone as can be seen in Figure 4.12, no cracks were formed within the transition zone. This observation proved that 5% debonding zone and 2.5% transition zone length with the addition of the shear studs as proposed by Qian et al. (2009) was sufficient for maintaining the stress concentration within the link slab. With increasing load and deflection, multiple micro-cracking occurred for the ECC link slabs and the crack width increased until it stabilized between 50 to 115 μm before the failure. The bending failure of the ECC link slabs occurred when the fiber bridging was reached for one of the cracks resulting in localized deformation. In contrast for SCC link slab a major crack was formed at the first crack loading and as the load was increased the crack width increased drastically to 3 mm until it reached the failure (Figure 4.13). All crack width measurements were performed in the unloading stage by using crack microscope. The crack closure was observed for all ECC link slabs during the unloading stage by 30 %. The summary of the crack characterization for all link slabs in terms of the number of the cracks and the range of crack width are presented in Table 4.4. The range of the cracks widths were measured for at least 10 major cracks development in the centre of the link slabs.

60

Table 4.4: Crack Characterization for Different Link Slabs

Designation	No of micro-crack	Range of Crack Width (μm)
LS2-ECC-CI-1.2-SS	26	50-75
LS3-ECC-F-2.2-SS	48	50-75
LS4-ECC-F-1.2-SS	30	50-75
LS6-ECC-F-2.2-CS	15	50-75
LS10-ECC-CI-2.2-SS	25	50-75
LS11-ECC-CI-2.2-CS	11	50-75
LS28-ECC-CI-1.2-MS	15	50-115
LS25-SCC	1 major crack	3200
LS32-SCC	1 major crack	3000

It is noted from Table 4.4 that the crack width for all ECC link slabs were below 115 μm in contrast to the SCC link slabs which was 3 mm. In terms of the durability and serviceability state, the crack widths for the ECC links slabs were below the current AASHTO Standards Specification for Highway Bridges (2002) which is 330 μm.

Figure 4. 12: Crack Characterization in Transition Zone

(a)ECC Link Slab   (b) SCC Link Slab

Figure 4.13: Crack Propagation and Failure of ECC and SCC link slabs

The number of the micro-cracks increased when the FA content increased from 1.2 to 2.2 for the ECC link slabs as higher FA content lowered the matrix toughness, which resulted as the easier work of fracture.

Use of Class CI fly ash decreased the number of cracks compared to fly ash class F. Use of CS or MS also reduced the number of micro-cracks compared to those with SS (Table 4.4). Class CI fly ash produces ECCs with higher matrix toughness (because of more calcium content) compared to those with class F and hence, produces lower number of cracks. The increase in

maximum size of aggregate (MAS) results in better aggregate interlocking which increases the matrix toughness and work of fracture for cracks propagation (Sahmaran et al. 2009). Within the same MAS, mortar and crushed sand; the link slabs with the crushed sand exhibited lower number of the cracks and crack widths in compare with the mortar sand. Once again the angular shape of the crushed sand provides better aggregate interlocking which enhances the fracture work in compare with the mortar sand (which has rounded particle).

4.3.4 Energy Absorbing Capacity and Ductility of Link Slabs

The energy absorbing capacity for the link slabs (summarized in Table 4.5) was determined by the area under the load-deflection curves (Figure 4.1) up to the post-peak load of 85% of the ultimate/peak load. From Table 4.5, it is observed that all ECC link slabs have higher energy absorbing capacity compared to their SCC counterparts. Even the minimum energy absorbing capacity of 81.2 joules for ECC link slab is 2.5 times higher than 35.3 Joules of SCC link slab. The high energy absorption capacity indicates the superior strain hardening behavior of the ECC mixes. As it is observed from the load-deflection response in Figure 4.1, the high energy absorption capacity of ECC link slabs were associated with the higher ultimate load and deformation capacity (ductility) compared to SCC.

The ductility index was determined based on the ratio of energy at the 85% of the peak load to the peak load energy of the link slabs (AASHTO, 2012; Wang & Belarbi, 2011). While the energy based ductility indexes for all ECC link slabs were greater than their SCC counterpart, they also satisfied the proposed ranges of 12-25 of the ASTM C1018 (1997) standard for the fiber reinforced concrete for the post-peak failure. The high ductility index proves that ECC at post failure maintains its strength which attributes to its ductile failure in contrast to the brittle failure of the SCC link slab.

The high energy absorbing and ductility performance make ECC an excellent material for the construction of link slab s in comparison to the SCC. This attribute allows the flexible ECC link slab to form hinges and allows the adjacent simply supported bridge spans to deform freely.

Table 4.5: Energy Absorption and Ductility Responses of Link Slabs

Designation	Energy at 85% ultimate load (J)	Energy ratio with respect to SCC	Ductility Index	Ductility ratio with respect to SCC
LS2-ECC-CI-1.2-SS	81.6	2.31	19.778	1.47
LS3-ECC-F-2.2-SS	111.59	3.16	29.189	2.16
LS4-ECC-F-1.2-SS	81.25	2.3	24.167	1.79
LS6-ECC-F-2.2-CS	107.57	3.06	32.766	2.43
LS10-ECC-CI-2.2-SS	88.18	2.49	15.979	1.19
LS11-ECC-CI-2.2-CS	85.05	2.41	14.398	1.07
LS28-ECC-CI-1.2-MS	92.84	2.63	37.220	2.76
LS25-SCC	37.4	1.05	14.55	1.07
LS32-SCC	35.31	1	13.477	1

The increased FA content resulted as a higher energy absorption capacity and ductility index for the ECC link slabs. The increased ductility index at higher FA content indicates the improved bending capacity response at post failure. As previously stated, the improved ductility of the ECC by increasing the FA content resulted from the reduction of the toughness matrix while improving the frictional bonding of the matrix and the PVA fiber which improves the bending capacity and the ductility index. The energy absorbing capacity and ductility index were improved at higher MAS of sand due to the improved ultimate strength capacity and increased in stiffness of the matrix. The higher energy absorbing capacity followed by fiber bridging characteristic at the post-peak failure improved the ductility index of the ECC mixes with increase in MAS.

4.3.5 Stiffness

The initial stiffness of all link slab specimens calculated from load-deformation responses is tabulated in Table 4.6. The comparative stiffness plots for the ECC and SCC link slabs are also presented in Figure 4.14.

Table 4.6: Summary of Link Slab's stiffness

Link Slab Designation	First cracking Load (kN)	First Cracking Stiffness (kN/m)
LS2-ECC-CI-1.2-SS	3.25	120.8
LS3-ECC-F-2.2-SS	3.25	161.4
LS4-ECC-F-1.2-SS	3.5	201.5
LS6-ECC-F-2.2-CS	3.25	173.3
LS10-ECC-CI-2.2-SS	3.25	98.7
LS11-ECC-CI-2.2-CS	3.5	112.8
LS28-ECC-CI-1.2-MS	3.10	205.7
LS25-SCC	4.86	500.1
LS32-SCC	5.13	300
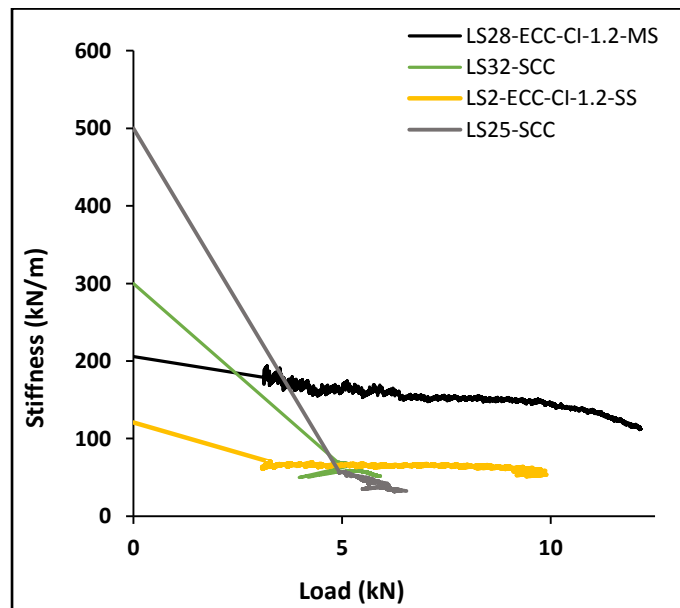
Figure 4.14: Stiffness of ECC and SCC Link Slabs

65

The initial stiffness of the ECC link slabs were are around 205 kN/m and steady decreased with the increase in load until reached to 100 kN/m at ultimate loading. In contrast, the initial stiffness for the SCC link slabs was higher up to the first crack load showing a value of 500 kN/m and decreased rapidly with the increase of load to 75 kN/m before converges to zero at ultimate loading. The steady state stiffness for the ECC link slabs after the first crack load demonstrates the fiber bridging and strain hardening characteristics.

Additional plots are presented in Figure 4.15 to study the influence of different fly ash content and different aggregate size on the stiffness degradation of ECC link slabs.
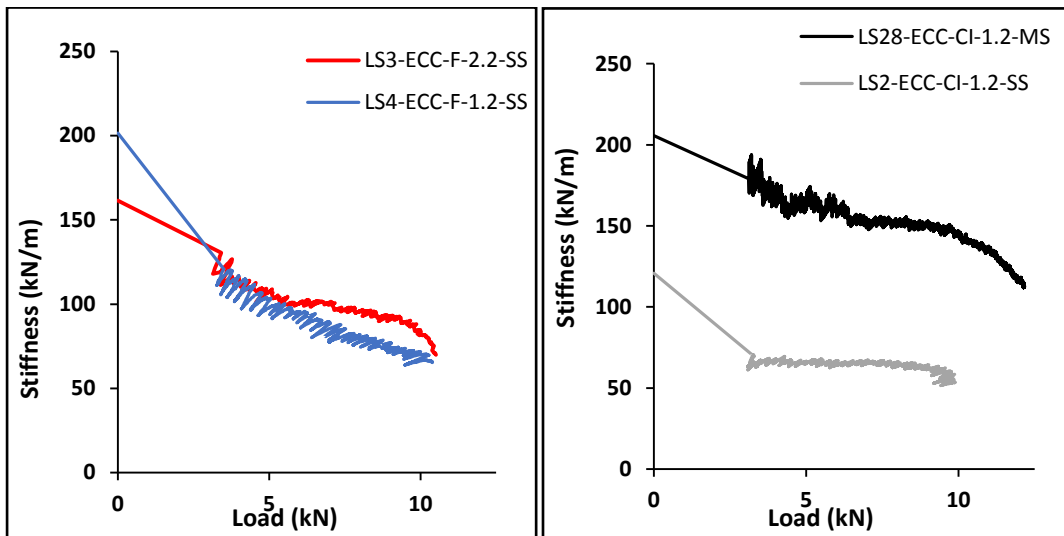
(a) ECC Link Slabs at different FA content   (b) ECC Link Slabs at different aggregate sizes

Figure 4.15: Stiffness evolution of ECC Link Slabs with Load

The lower fly ash content exhibits higher initial stiffness as it is visualized by Figure 4.15(a). However, after first cracking, the stiffness degradation is not influenced by the fly ash content. In contrast, the stiffness of the mortar sand based ECC link slab (at first cracking and ultimate load) is found to be higher compared with silica sand ECC. The stiffness of mortar sand based ECC link slab at pre-cracking and at ultimate loading were 205 kN/m and 100 kN/m, respectively whereas those for silica sand based ECC link slab were 120 kN/m to 50 kN/m, respectively. The

higher stiffness for the mortar sand based ECC link slab is attained by larger aggregate size that improves the loading capacity through aggregate interlocking through enhanced friction.

4.4 Structure Performance and Evaluation of a Scaled Down Full Bridge with ECC Link Slab Subjected to Static Loading

For a comprehensive study of a link slab application, two 1/6th scale simply supported full bridge spans (composite Span 1 and Span 2: made steel I-beam and concrete deck connected through shear studs) with connecting ECC link slab (Figure 4.16) were designed and tested under monotonic loading within the elastic limit (up to service stage - 50% of the design load). The full bridge model was adopted from the full-scale bridge tested by Caner & Zia (1998) and was designed in accordance to CHBDC (2006). The ECC mix with mortar sand and 55% fly ash CI (ECC-CI-1.2-MS) was used for the link slab construction and SCC was used for the adjacent bridge deck portions. This section presents the results of this experimental investigation in terms of the load-deformation/rotation responses, followed by comparative analysis with available theoretical models. In addition experimentally obtained location of inflection points was compared with those suggested by design specification.

4.4.1 Load-Deformation/Moment-Rotation Responses and Theoretical/Code Based Analyses

The load-deformation responses for the SCC simply supported spans (Span 1 and Span 2) and the ECC link slab were monitored through the linear variable differential transformers (LVDT) installed at strategic locations including at the maximum moment location through a computer aided data acquisition system. The applied loading was selected as 50% of the design load of the bridge span (normally considered in a real bridge structure at the service load stage) for analyzing the performance of ECC link slab. After extensive analysis and design, the applied service load for each simply supported composite bridge deck span was selected as 50.49 kN. For a comprehensive understanding a schematic representation of the full joint-free bridge model showing applied loading points and instrumentation (such as location of strain gauge and LVDTs inclinometer including their numbers) is presented in Figure 4.16.
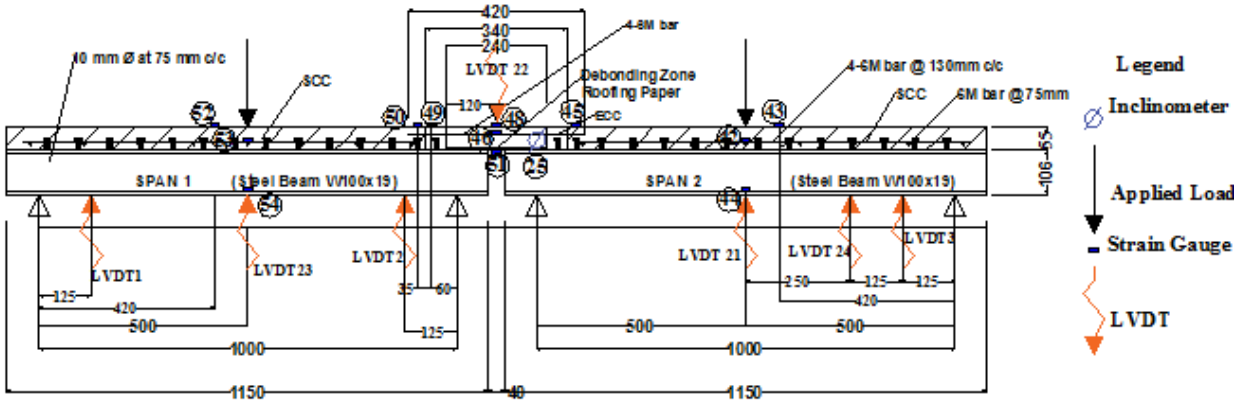
Figure 4.16: Schematic Representation instrumentations locations and designations for the 1/6th Scale Full Bridge Model (dimensions are in mm)

For validation of simply supporting performance of the adjacent spans, the experimental deflection (Δ)and support end rotation (θ) at the applied loading of 50.49 kN on each span were compared with those calculated based on theoretical calculations [Equations 4.1 and 4.2].

$$\Delta = \frac{PL^3}{48EI} \qquad\qquad\qquad [4.1]$$

$$\theta = \frac{PL^2}{16EI} \qquad\qquad\qquad [4.2]$$

where P, L, E and I denotes applied loading on each span at midpoint length of the spans, modulus of elasticity and second moment of inertia of the composite bridge span.

The experimental load-deformation/rotation responses for the full bridge structure are presented in Figures 4.17 and 4.18. Due to similar behaviour of adjacent spans, it was decided to only present the results for the SCC-SPAN 2 (SP2-SCC) and ECC link slab (LS-ECC) (Figure 4.16). Table 4.7 summarizes the key results from the experiments and theoretical analysis.

Table 4.7: Key results from Load-Deformation/Moment Responses of the Full Bridge Models with ECC Link Slab

Section	Reinforcing Ratio	Applied Load (kN)	Applied Moment (kN.m)	Experimental		Theoretical (Based on SCC simple span)	
				Maximum Deflection (mm)	Maximum Rotation (Radian)	Deflection at Maximum Applied Load (mm)	Rotation at Maximum Applied Load (Radian)
SP2-SCC	0.01	50.49	12.62	0.987 (downward)	0.00303 [**]	0.862	0.00258
LS-ECC	0.01	0	1.67 [*]	0.315 (upward)	0.00268 [***]	0	0.00258

[*]Induced Moment calculated by Equation 2.6
[**]Outer SCC support
[***]Inner SCC support (ECC and SCC interface)
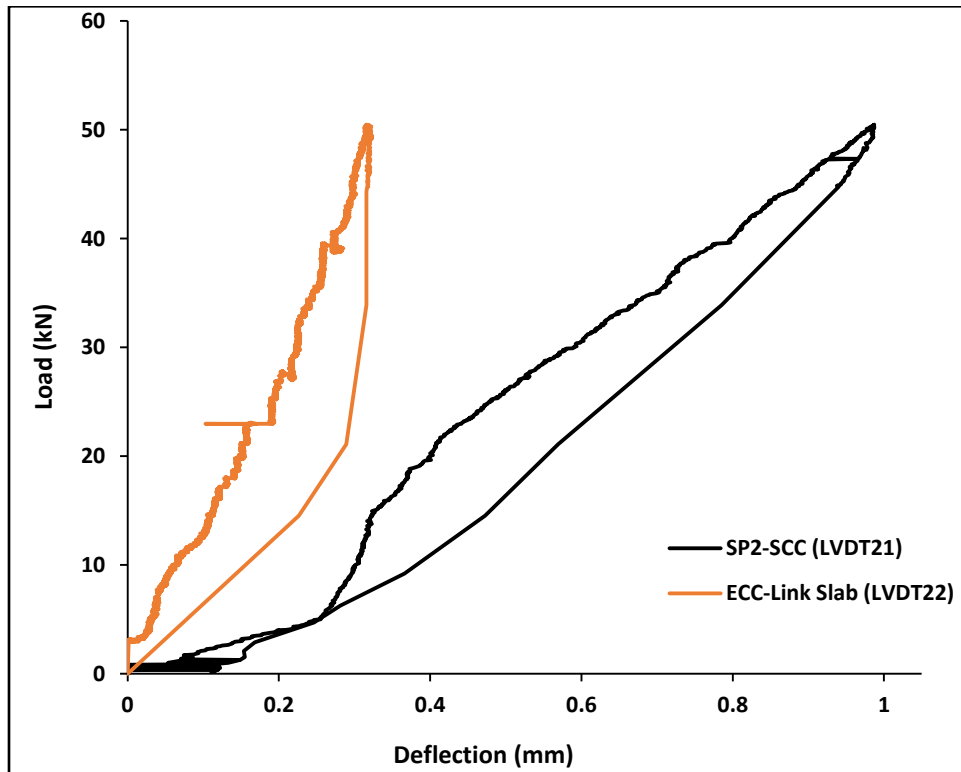
Figure 4.17: Load-Deflection Response of a Full Bridge with ECC Link Slab

As it was expected, the SCC spans deformed downward while the ECC link slab deformed upward due to the continuity of the bridge deck and development of positive and negative moment. For applied loading of 50.49 kN (at service load-stage), the mid-span deflections for the SP2-SCC and LS-ECC were 0.987 mm downward and 0.315 mm upward, respectively (Table 4.7).

The linear load-deflection response presented in Figure 4.17 demonstrates that ECC-Link Slab and SP2-SCC are within the elastic limits as the test was originally designed to be conducted at the service stage. At the service load stage, the induced moment on the ECC link slab was 1.67 kN.m (calculated by Equation 2.6), only 10% of the designed ultimate ECC link slab capacity. The low induced moment justifies the small deflections on the ECC link slab. The small induced moment at the service load stage indicates the prolonged life for the ECC link slab. Based on these analysis, the failure of the SCC bridge span within the full bridge is expected to occur rather than the ECC link slab.

The experimental mid-span deflection for the SP2-SCC span was compared with theoretical simple span deflection (calculated using Equation 4.1) at the maximum applied loading. The theoretical deflection (0.862 mm) was slightly lower than the experimental deflection (0.987 mm) - such negligible difference between them proves that full bridge model behaved as a two simply supported spans with a connecting ECC link slab. This proves that flexible ECC link slab allows the rotation of adjacent bridge girder as desired.
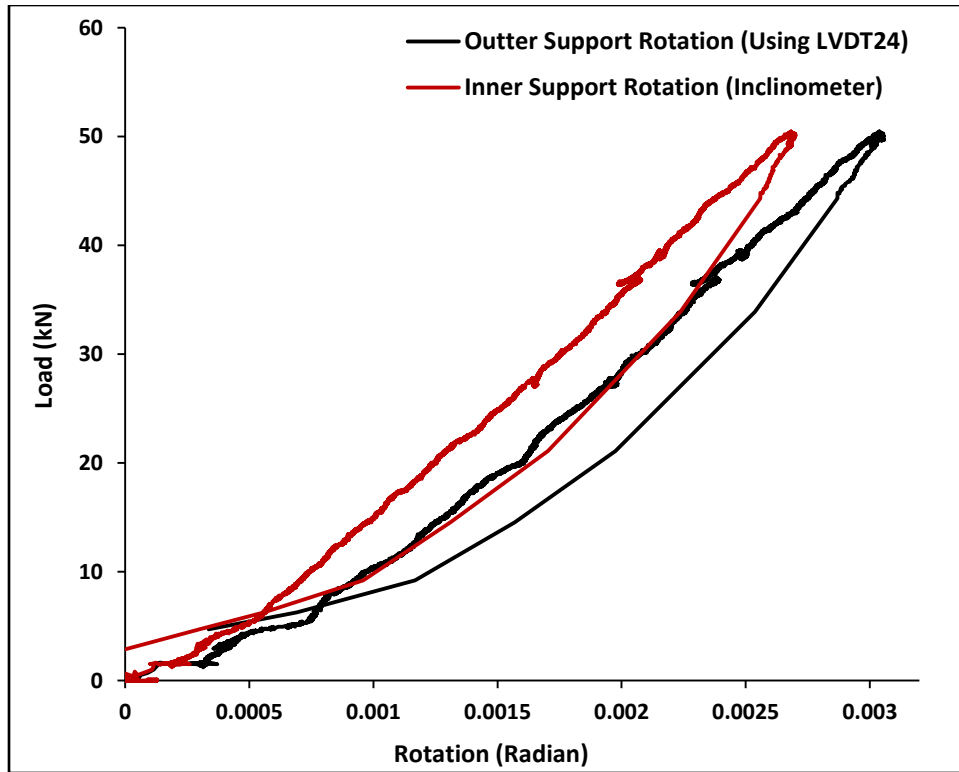
Figure 4.18: Load-Rotation Response of Full Bridge with ECC Link Slab

While the concrete deck was continuous due to the connecting ECC link slab, the steel girders for the SCC spans were designed as simply supported. In theory, equivalent inner and outer support rotations for the SCC spans are required for allowing the steel girders to deform freely as simply supported spans.

From the experimental results presented in Figure 4.18 and Table 4.7 it is observed that the inner support rotation (LS-ECC and SP2-SCC interface) was smaller in compare with the outer support (SP2-SCC). The inner and outer support rotation at service load-stage of 50.49 kN were 0.00268 and 0.00303 radian respectively. Even though ECC link slab exhibits a high bending capacity associated with low stiffness, it restrained the movement of the support rotation - therefore a small difference is evidenced between the inner and outer support. The negligible difference (only 11.5%) among the inner and outer support rotation, followed by comparative analysis of experimental and theoretical (Equation 4.2) support end rotation proves that ECC link slab with low stiffness/high flexibility and high ductility maintains the simply supporting

performance of the adjacent bridge girders (similar to a construction joints used between two adjacent spans in traditional bridge construction).

The experimental support end rotations (both inner and outer support) at service load stage satisfy the maximum allowable AASHTO (2012) end rotations of 0.00375 radian. These attributes prove that ECC is a suitable material for the link slab application since it satisfies the ultimate and serviceability limit states.

4.4.2 Strain Development Characteristics

As it was expected, tensile strain/stresses were developed at the bottom flanges of the steel I-girders for the SCC spans and on top of the ECC link slab due to the developments of the positive and negative moments. The summary of the strain developments for the composite SCC sections (including concrete, rebar and steel girder), and ECC link slabs are presented in Table 4.8. Figure 4.19 presents the development of strain (concrete/rebar/steel I-girder) with load for SCC girder and ECC link slab (location of numbered gauges are shown in Figure 4.16.

Table 4.8: Strain Developments for the Full Bridge with ECC Link Slab

Section	Reinforcing Ratio	Applied Loading (kN)	Strain Development		
			Tensile (micro-Strain)	Concrete Compressive (micro-strain)	Rebar (micro-strain)
LS-ECC	0.012	50.49	101 (Concrete, top of ECC link slab)	-41	+64
SP2-SCC	0.012	50.49	438 (bottom flange of steel girder)	-282	-259

- Compression strain; + tensile strain
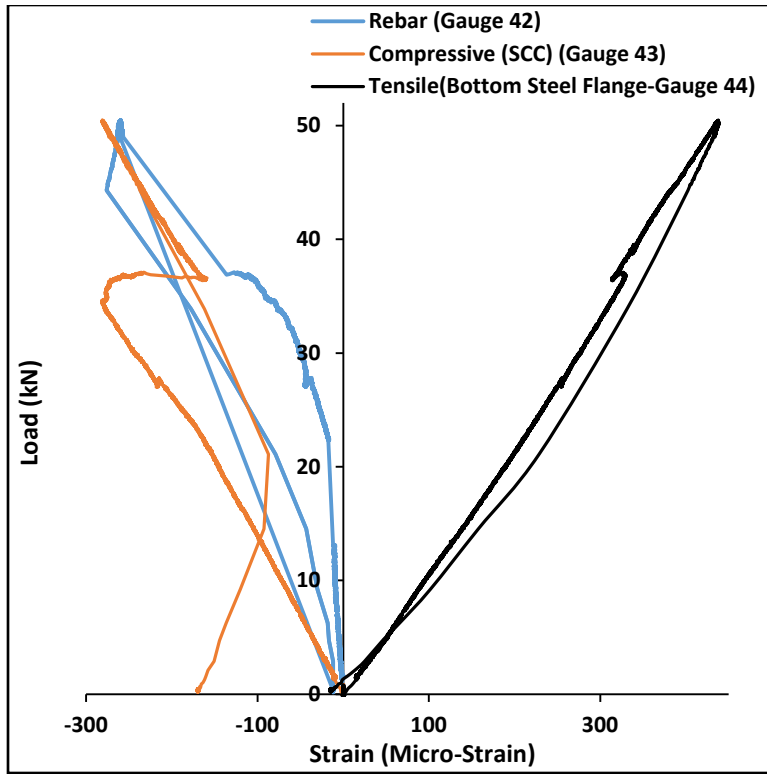
(a) SP2-SCC
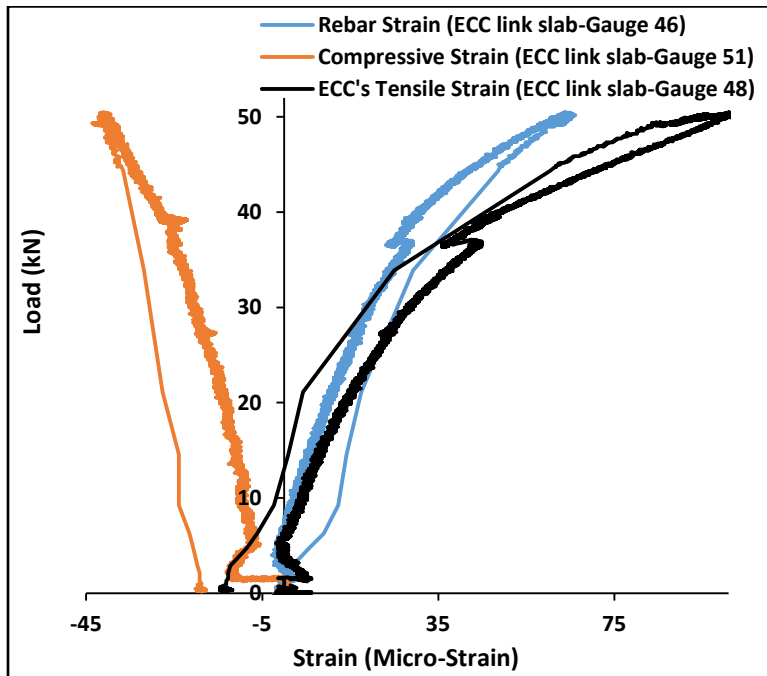
(b) LS-ECC

Figure 4.19: Strain Developments for a Full Bridge with ECC Link Slab

73

It can be noted from Figure 4.19(a) that the SP2-SCC (including compressive strain in concrete and rebar and tensile strain at the bottom flange of steel girder) demonstrate elastic linear strain developments. The compressive strain development for the SP2-SCC rebar indicates that the concrete deck is under compression and signifies that location of the elastic neutral axis is within the web of the steel girder which confirms the theoretical location of the neutral axis.

At the service load stage, the ECC link slab exhibited low strain developments (Figure 4.19b and Table 4.8). The negligible concrete tensile and rebar strain developments (only 101 micro-strain and 64 micro-strains) indicates the unused high strength capacity of the ECC link slab even at service load of adjacent girder. The strain development characteristics also justifies that SCC sections will fail in prior to the ECC link slab. As a result, a further reduction of the reinforcing bar is recommended for reducing the stiffness of the ECC link slab due to the strain hardening characteristic and high tensile strain capacity.

4.4.3 Comparative Analysis of Experimental and Theoretical Location of Inflection Points

The zero strain development along the length of the bridge span demonstrates the location of the hinges and the points of the inflections in the bridge spans (Figure 3.1). The distance between these points of inflections represents the length of the link slab specimen (Lepech & Li, 2009; Caner &Zia, 1998). Based on the stiffness of the link slab, the location of inflection point varies from 0 and 20% of the span's length. For the ECC link slab with a low stiffness and higher bending capacity the points of inflection is recommended as 7.5% of the adjacent bridge spans (Lepech & Li, 2009). The top fiber strain developments (Gauges 52, 50, 49, 48, 45, 43) for the full bridge model (along the length of the bridge) was used for determining the experimental location of the inflection points/hinge formation. The experimental hinge location and total length of the link slab are illustrated in Figures 4.20 and 4.21 respectively.
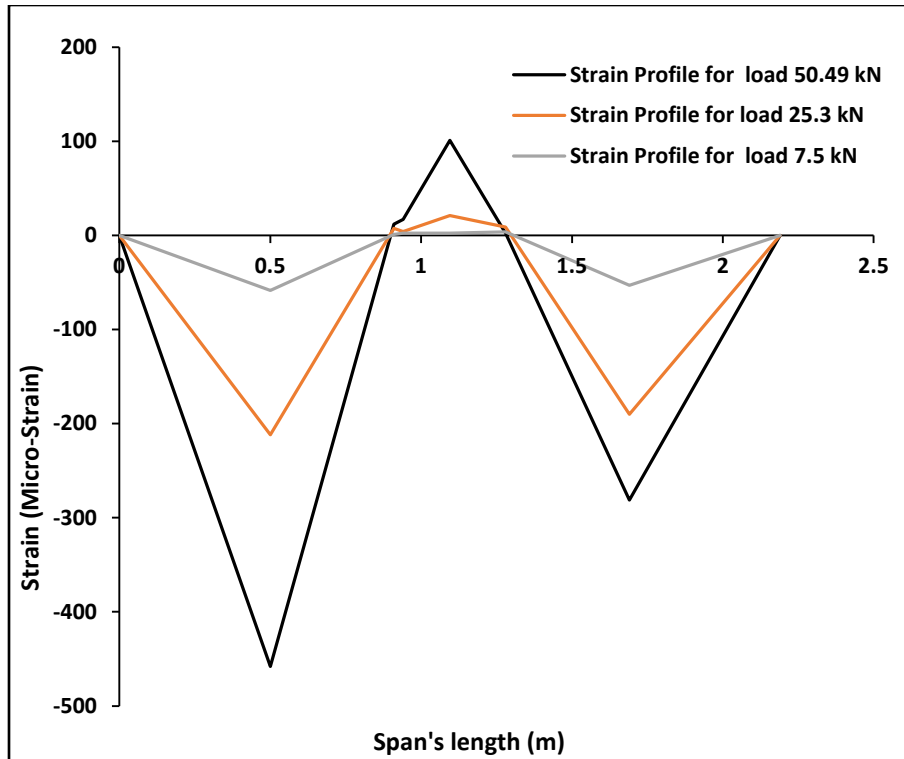
Figure 4.20: Top Fiber Strain Profile for Full Bridge with ECC Link Slab at Different Loading

As it is observed from Figure 4.20 and 4.21, for various load levels, the hinges were formed at 910 mm and 1280 mm from the left support (location of zero strain) on the adjacent bridge spans. As a result, the total length of the link slab is found to be 370 mm.

While the experimental length of the link slab was 370 mm, the design length was limited to 340 mm (designed according to Lepech & Li, 2009 approach). The small difference between the experimental and design length of the link slab (ratio of experimental to design length of 1.08) was influenced by the stiffness of the ECC link slab that provided rotational restraint to the adjacent spans. In the experimental full bridge, the hinges were formed at 9% of the adjacent spans rather than 7.5% suggested by the design specification. However, only 8% difference between experimental and design recommendation seemed to be very good. The high ductility and flexibility of the ECC link slab are exhibited and capability of ECC link slab in allowing adjacent spans to deform (rotate) freely for maintaining the traditional simply support span design approach is demonstrated.
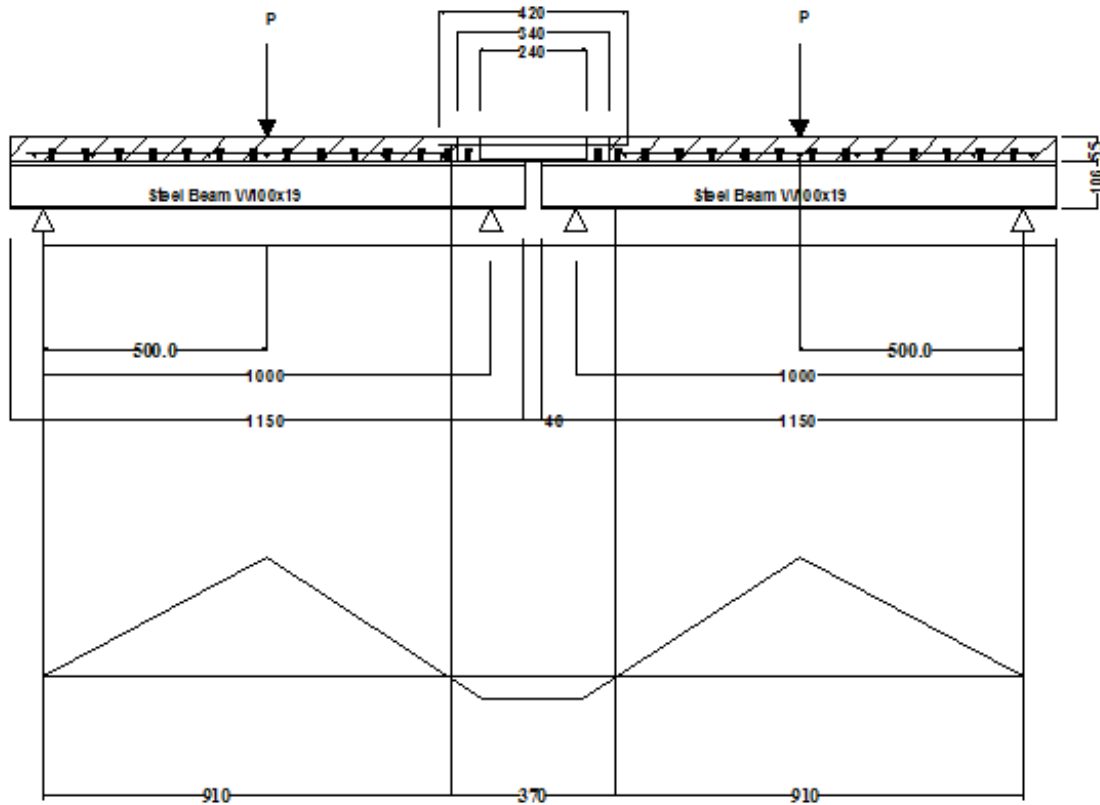
Figure 4.21: Schematic Representation for Location of Inflection Points (Dimensions are in mm)

4.5 Summary

This chapter described the results of for monotonic performance of the 1/4th scale link slab specimens incorporating different green cost-effective ECC mixes subjected to failure under monotonic loading. In addition, the performance of ECC link slab is demonstrated by conducting test on a 1/6th scale joint-free full bridge model having two simply supported spans subjected to monotonic loading up to service stage. The results of the 1/6th scale full bridge with ECC link slab were evaluated and discussed with available design guidelines proposed by other scholars. The experimental and theoretical analyses confirmed the viability of ECC link slab to construct joint-free bridges satisfying serviceability limit and design specifications.

CHAPTER FIVE

FATIGUE PERFORMANCE OF ONE FOURTH SCALE LINK SLABS

5.1 Introduction

The green sustainable ECC mix made with mortar sand and fly ash CI with good performance (in terms of strain hardening and multiple cracking characteristics (ECC-CI-1.2-MS) was selected to evaluate the flexural fatigue performance of the one-fourth scale link slab specimens. The flexural fatigue testing was performed in three different stages: pre-fatigue behaviour under monotonic loading to failure, fatigue behaviour under cyclic loading at different stress levels and post-fatigue behaviour under monotonic loading to failure. The pre-fatigue monotonic test was performed to evaluate the ultimate strength, bending capacity and strain development of the link slabs and also to determine the applicable fatigue stress levels. After the analysis of the pre-fatigue monotonic testing, the flexural fatigue loading was performed on companion link slab specimens based on two different approaches. The first approach applied different fatigue stress levels of 40% and 55% of the ultimate load (determined from pre-fatigue monotonic testing) at a constant 400000 fatigue cycles. The second approach applied constant fatigue stress level of 40% at 4Hz cyclic loading rate (4 cycles per second) with variable fatigue cycles of 400000 and 1000000. After the fatigue performance, the flexural monotonic test was performed on the exhausted fatigued link slab specimens to determining the residual strength, strain, rotation, energy and stiffness. For a comparative analysis SCC link slabs were also tested under the same conditions. However, it should be noted that SCC link slabs could not be tested at high stress level (at 55%) and high fatigue cycles (100000) as they failed before reaching the first fatigue cycle exhibiting poor performance under fatigue loading. Therefore, there was no available data for the SCC link slabs at 55% fatigue stress level and 1000000 fatigue cycle.

This chapter presents the results of the flexural fatigue performance of the $1/4^{th}$ scale link slabs tested in three different stages under pre-fatigue monotonic (already described in Chapter 3 but presented in this chapter from fatigue point of view to compare pre-and post-fatigue behaviour), fatigue and post-fatigue monotonic loading. The fatigue performance for both approaches (variable fatigue stress levels and cycles) are evaluated based on load-deformation responses,

strain developments, crack characterization, energy absorbing capacity, ductility index and stiffness.

5.2 Performance of Link Slabs at Different Fatigue Stress Levels

5.2.1 Fatigue Performance

To avoid slippage of the specimens, the link slabs were subjected to pre-monotonic loadings of 40% and 55% of the ultimate loads (determined from by ECC and SCC control link slab specimens subjected to monotonic loading to failure) as a ramp into the flexural fatigue loading. In the subsequent fatigue loading, the 40% and 55% stresses were selected as the mean fatigue stress levels with a stress range of ±20% of the ultimate load. As a result the stress ranged from 20% to 60% of the ultimate load for the link slab specimen subjected to 40% mean fatigue stress level. Similarly for the 55% mean stress level, the applied fatigue stress varied from 35% to 75% of the ultimate load.

The SCC link slab subjected to higher fatigue stress range of ±20% failed at the beginning of the fatigue testing before completing the first cycle. Due to the weak response of the SCC, it was decided to reduce the stress of the SCC link slabs to ±5% of the mean stress level.

5.2.1.1 Load-Deflection Responses and Deflection Evolution

During the fatigue loading, the mid-span deflection was recorded on the data acquisition system for every cycle. The load deflection responses for the ECC and SCC link slabs at variable fatigue stress levels of 40% ± 20, 55%±20 and 40% ±5 are presented in Figure 5.1 and key results are summarized in Table 5.1. For comprehensive understanding of stress variations, the mean fatigue stress levels for each link slab specimens are also presented in Figure 5.1.
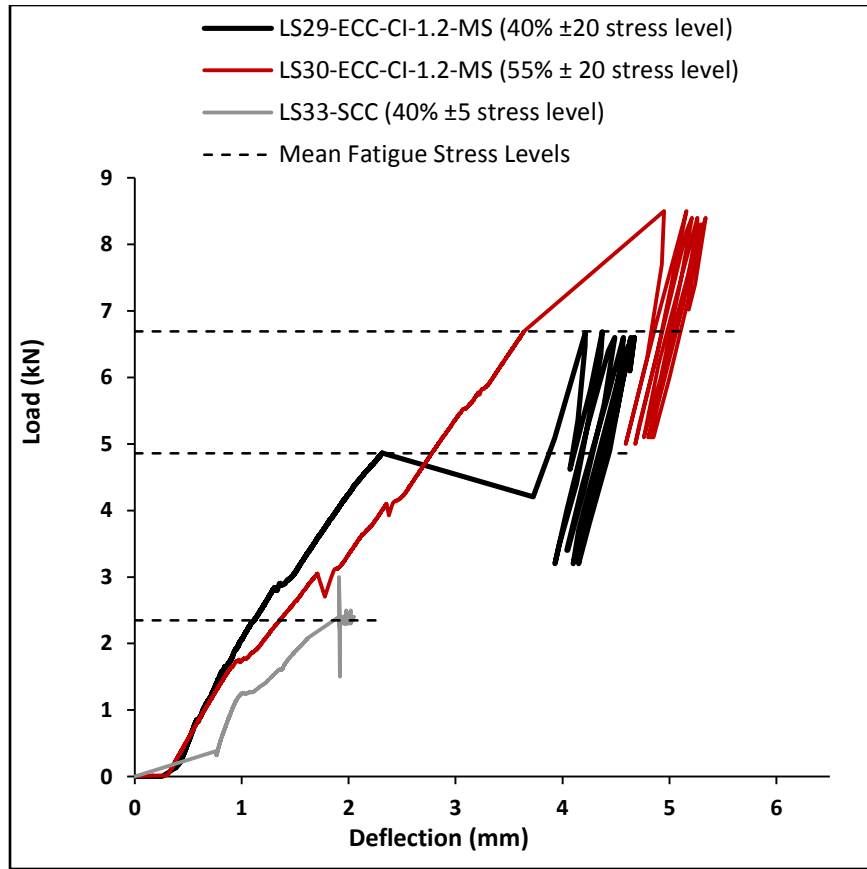
(a) Load-Deflection Response

Figure5.1: Load-Deflection Responses of Link Slabs at Different Fatigue Stress Level

Table5.1: Mid-Span Deflection Evolution at Different Fatigue Stress Level

Designation	Ultimate Load* (kN)	Mean Fatigue Stress Level (%)	Fatigue Stress Range (%)	Applied Fatigue Loading (kN)	Initial Deflection (mm)	Deflection Evolution for the first 10000 fatigue cycle (mm)	Final Deflection (mm)	Difference between First and Last value of Mid-Span Deflection (mm)
LS29-ECC-CI-1.2-MS	12.16	40%	±20%	4.86 ±2.43	2.31	4.1	4.7	2.39
LS30-ECC-CI-1.2-MS	12.16	55%	±20%	6.69 ±2.43	3.63	4.9	5.35	1.72
LS33-SCC	5.93	40%	±5%	2.37± 0.1	1.62	1.91	2.04	0.42

*Ultimate Load for each link slabs based on pre-fatigue monotonic performance

It is observed from Figure 5.1 that the mid-span deflection for the ECC link slabs (at 40% ±20% and 55% ± 20% stress level) increased drastically during fatigue loading due to formation of larger deflection band widths in compare with the SCC link slab (at 40%±5 fatigue stress level) with no band width development. While the increase in deflection for the SCC link slab at 40% ±5 stress level was only 0.42 mm, the increase for both ECC link slabs at 40% ±20 and 55%±20 stress level were 2.39mm and 1.79mm, respectively (Table 5.1). The large deflection band width for the ECC link slabs demonstrate a large bending capacity and strain hardening characteristic even at the high fatigue stress range (±20% of ECC's ultimate loading). This shows that after formation of cracks under repetitive fatigue loading at high stress range of ±20%, the bending capacity of the ECC is enhanced; therefore ECC controls the fatigue performance. As previously stated, the SCC link slab at the same high stress range of ±20% failed before completing a cycle.

From the mid-span deflection evolution curve (Figure 5.2(a)), it is observed that all link slab specimens (ECC and SCC) deform more at the initial fatigue cycles. The ECC link slab at 40% ± 20 fatigue stress level deforms from 2.31 mm to 4.10 mm and the SCC link slab at 40% ± 5% fatigue stress level deforms from 1.62 to 1.91 mm at the initial 10000 fatigue cycle (Figure 5.2(a)). The high deflection evolution at the initial fatigue cycle was caused by the stress jump from the mean stress (attained by the monotonic loading) to high fatigue stress ranges (±20% for the ECC and ±5% for the SCC link slabs).

It is also noted from Table 5.1 and Figure 5.1 that larger deflection band width was developed for the ECC link slab at 40% ±20 fatigue stress level in compare with the ECC specimen at 55% ±20 stress level. The change in mid-span deflection for the ECC link slab at 40% ± 20 was 2.39 mm whereas the change for the ECC link slab at 55% ± 20 stress level was 1.72 mm only (Table 5.1). The smaller change in deflection for the ECC link slabs at 55% ± 20 stress level was due to the increased damage level (lowering its subsequent fatigue resistance) during the pre-fatigue loading. The imposed high pre-fatigue stress level (55% of ECC's ultimate load) increased the mid-span deflection (associated with more concrete cracking and high steel strain development) and damage level for LS30-ECC-CI-1.2-MS (55%±20) before initiation of the fatigue loading. The increase in pre-fatigue damage level followed by intensive fatigue loading (±20%) led to a failure of the fibers and link slab specimen.

Similarly, the change in deflection evolution at initial 10000 fatigue cycle (Figure 5.2a), for the ECC link slabs subjected to 40% ± 20 and 55% ±20 fatigue stress levels are higher in compare to the full fatigue cycles (Figure 5.2b) due to same reason of stress jump from the mean to high range of fatigue loading (±20% of ECC's ultimate load). Same is also true for SCC link slab.
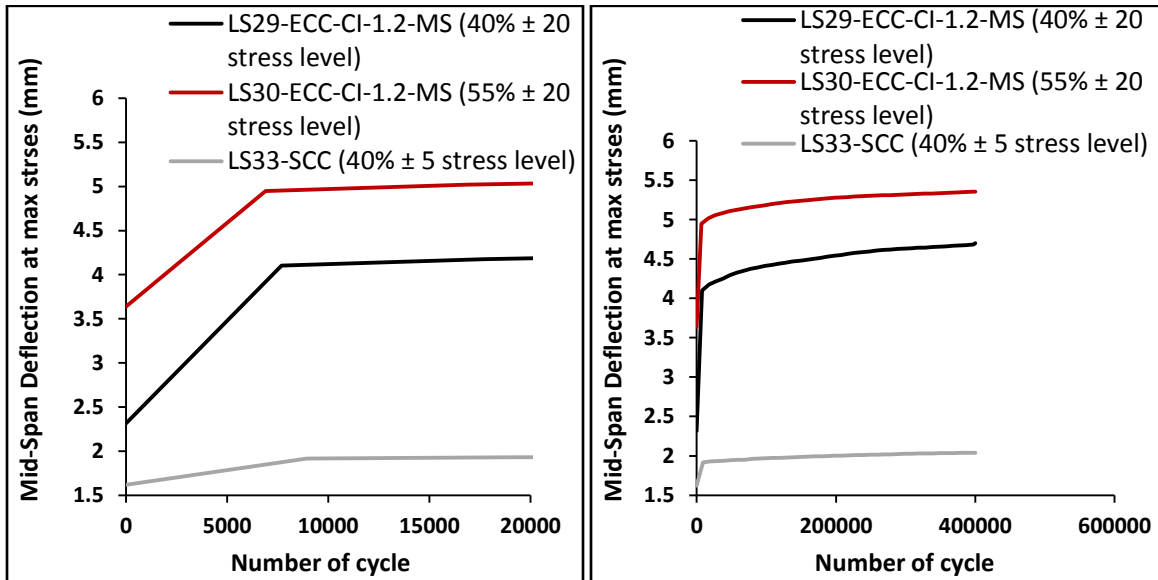
(a) Deflection Evolution at Initial 10000 Fatigue Cycle   (b) Deflection Evolution at Full Fatigue Cycle

Figure5.2: Mid-span Deflection Responses at Different Fatigue Stress Level

5.2.1.2 Strain Developments

During fatigue performance concrete and rebar strain developments due to applied fatigue loading were monitored and recorded for every cycle using a data acquisition system. The concrete tensile and compressive strain followed by rebar strain developments for the link slabs at different fatigue stress levels are presented in Figures 5.3 and key findings are summarized in Table 5.2.
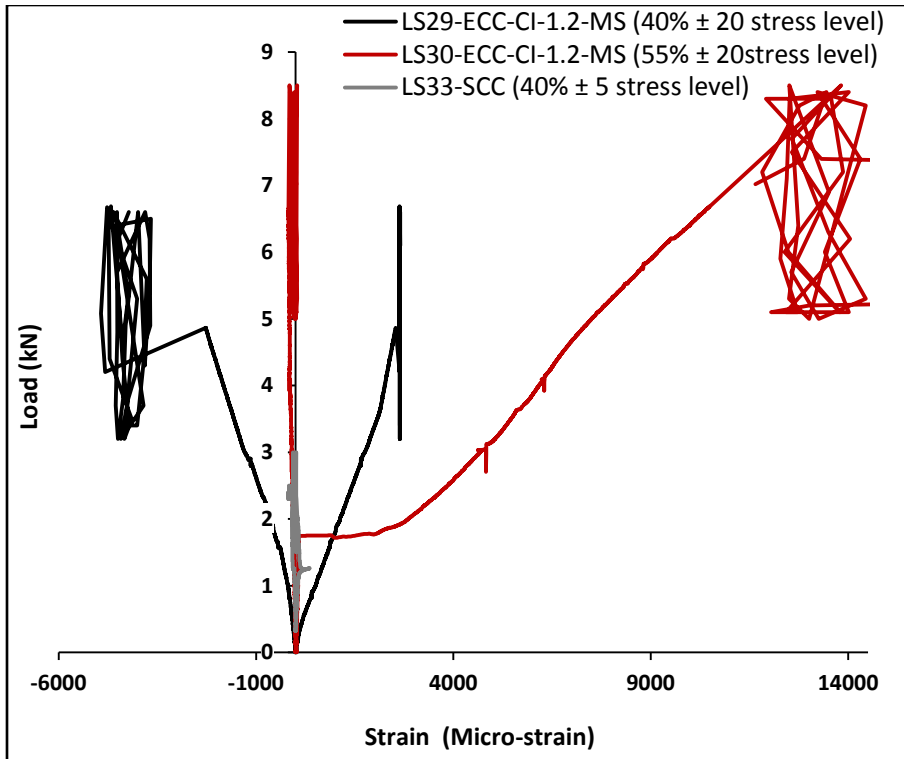
(a) Concrete Strain Developments
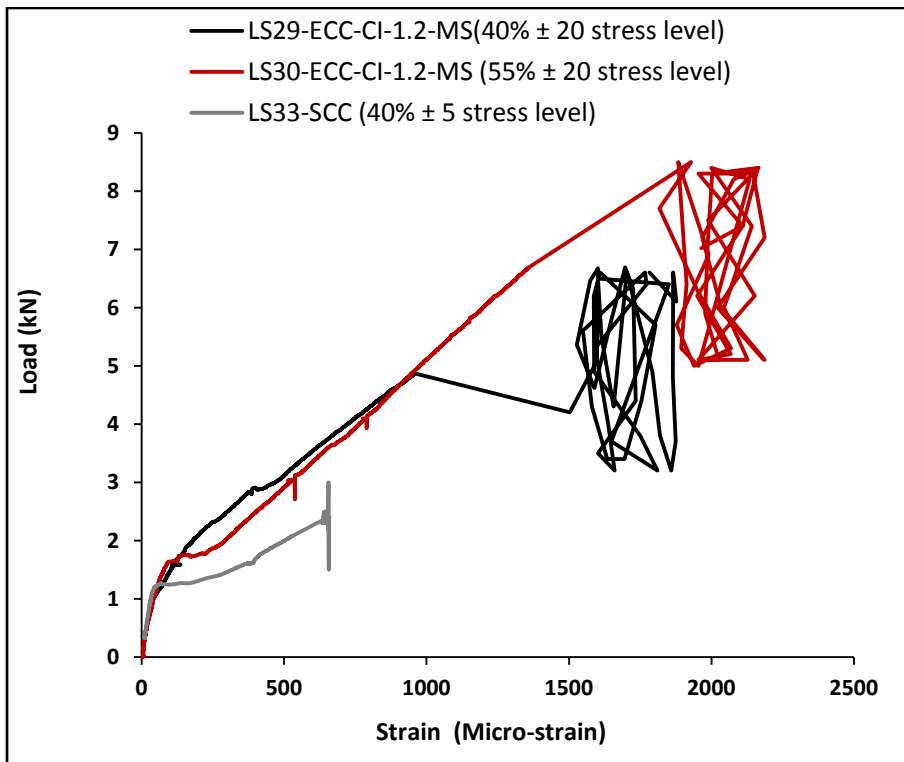
(b) Rebar Strain Development

Figure 5.3: Strain Developments for the Link Slab specimens at Different Fatigue Stress Levels

82

Table 5.2: Strain Development of Link Slab During Fatigue Performance at Different Fatigue Stress Levels

Designation	Fatigue Stress Level (%)	Applied Fatigue Loading (kN)	Initial Concrete Tensile Strain (Micro-Strain)	Final Concrete Tensile Strain (Micro-Strain)	Initial Concrete Compressive Strain (Micro-Strain)	Final Concrete Compressive Strain (Micro-Strain)	Initial Rebar Strain (Micro-Strain)	Final Rebar Strain (Micro-Strain)
LS29-ECC-CI-1.2-MS	40% ±20	4.86 ±2.43	2536.1	2647.1	-2281.5	-4227.3	961.3	1782.1
LS30-ECC-CI-1.2-MS	55%±20	6.69 ±2.43	10496.4	11653.3	-181.3	-25.1*	1358.6	1964.3
LS33-SCC	40%±5	2.37± 0.1	41.5	0*	-93.1	-184.2	529.5	645.8

*Strain gauge damaged

As it is evidenced from Figure 5.3(a), no concrete tensile strain band width was formed for the SCC link slab subjected to 40% ± 5% stress level. In fact, SCC concrete tensile strain was much lower at the beginning of fatigue performance because of stress release due to crack formation. Figure 5.4(a) also shows lower concrete tensile strain development at the initial fatigue cycle (at 10000 cycle). The rebar strain development was increased from 529.5 to 640 micro-strain for the first10000 fatigue cycle (Figure 5.4b). The increase in rebar strain for the SCC link slab at 40% ±5% may be associated with the transfer of load due to crack formation to the steel reinforcement. It is also evidenced (Figure 5.4b) that beyond the first 10000 fatigue cycle, rebar strain development remained constant since the applied stress range was very low (±5% of the mean stress level). The strain development characteristics justifies that the flexural fatigue resistance of SCC link slab is derived predominantly from the rebar contribution. In contrast ECC link slab at higher fatigue stress range (±20%) developed larger concrete tensile strain band width (in compare with SCC) during the fatigue loading (Figure 5.3a). The large tensile strain band width for the ECC link slab demonstrates its strain hardening characteristic that allows more bending and higher strain development compared to its SCC counterpart. Although the rebar strain was increased for the ECC link slab at 40%±20% stress level specifically for the first 10000 cycles, but it did not reach the yield strain (2000 micro-strain) even at the end of the 400000 fatigue cycles (Figure 5.4a and Table 5.2). This is indication of damage in ECC due to micro-crack formation during fatigue loading and gradual transfer of load to the steel rebar causing an increase in rebar strain. The higher increase in rebar strain for the ECC link slab was

caused by higher fatigue stress range of ±20% in compare with the SCC link slab (at ±5% fatigue stress range). The strain development signifies that ECC plays a significant role in enhancing flexural fatigue resistance and in mitigating damage.

The ECC tensile strain development for the link slab tested at higher fatigue stress level of (55%±20%) was greater compared to specimen tested at 40% ±20% stress level as indicated by the formation of larger tensile strain band width (Figure 5.3a and Figure 5.4a). However, developed ECC tensile strain was still lower compared to its tensile strain capacity 0.05. The rebar strain was close to the yield strain at the beginning of the fatigue loading and reached the yield strain of 2000 micro-strain at 147000 fatigue cycle. The increased rebar strain at 147000 fatigue cycle justifies that stresses were transferred to the reinforcing bars due to formation of micro-cracks along with rupturing of PVA fibers bridging the crack width. The rebar tensile strain for the ECC link slab tested at 55%±20% fluctuated at yield strain beyond 147000 fatigue cycle showing an increasing trend (Figure 5.4b). Overall, the large width of strain band development (both steel and concrete) for ECC links slabs compared to their SCC counterparts is an indication of ECC's superior performance in terms of inducing greater flexibility, ductility and energy absorbing capacity to the link slab.

(a) Concrete Tensile Strain   (b) Rebar Strain
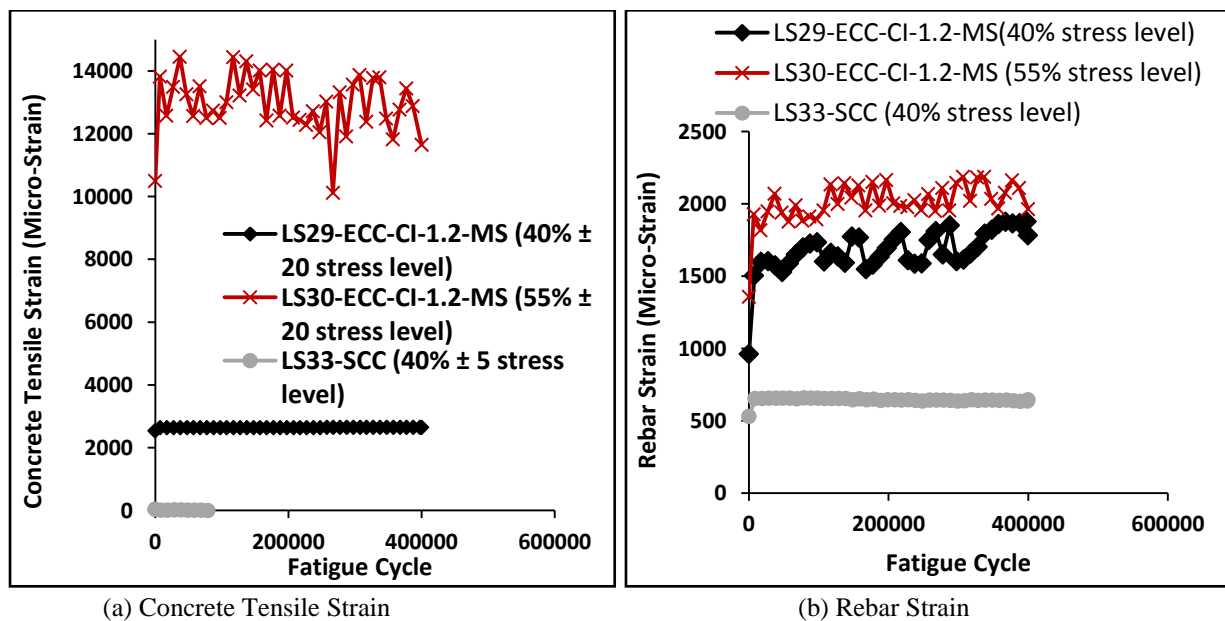
Figure 5.4: Strain Development Evolution for Link Slabs Subjected to Different Fatigue Stress Level

84

5.2.1.3 Evolution of Stiffness

The evolution stiffness of the 1/4th scale link slabs during the fatigue loading showing a trend of degradation is presented in Figure 5.5. Table 5.3 summarizes the initial stiffness and stiffness at final fatigue cycle of 400000 for SCC and ECC link slabs.

Table 5.3: Stiffness Degradation of Link Slabs at Different Fatigue Stress Level

Designation	Fatigue Stress Level (%)	Applied Fatigue Loading (kN)	Initial Stiffness (kN/mm)	Stiffness at end of fatigue cycle (kN/mm)
LS29-ECC-CI-1.2-MS	40%±20	4.86 ±2.43	2.10	1.42
LS30-ECC-CI-1.2-MS	55%±20	6.69 ±2.43	1.85	1.25
LS33-SCC	40%±5	2.37± 0.1	2.33	1.10
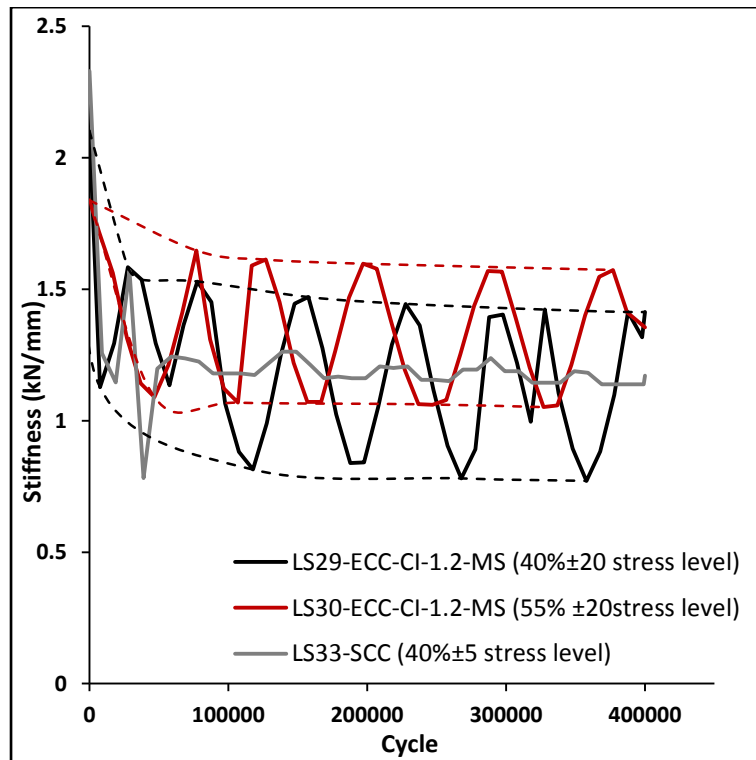
Figure 5.5: Stiffness Degradation of Link Slabs at Different Fatigue Stress Level

Figure 5.5 shows that the stiffness of the ECC link slabs oscillates due to fatigue loading application in the maximum and minimum stress levels as expected. The concrete cracking initiation results in stiffness degradation, but due to fiber bridging and strain hardening characteristic of the ECC, the recovery of stiffness is better in ECC compared to SCC. Although the stiffness for the ECC link slabs are recovered but due to the repetitive fatigue loading, gradual stiffness degradation is observed similar to SCC justifying the difference between initial and final stiffness. The initial stiffness (before the fatigue performance) for the ECC link slabs tested at 40% ± 20% stress level was 2.10 kN/mm and the stiffness was reduced to 1.41 kN/mm at end of the fatigue performance – showing a decrease of 33% (Table 5.3).

In contrast the SCC link slab initially demonstrated large stiffness (2.33 kN/mm) before the fatigue performance (Table 5.3). However the stiffness was dropped significantly from 2.33 kN/mm to 0.78 kN/mm at 30000 fatigue cycle) (a decrease of about 66%) due to major crack formation (Figure 5.5). Beyond 30000 fatigue cycles, gradual stiffness degradation was observed without major stiffness degradation. The stiffness response for the ECC link slab tested at 40% ± 20% and 55% ± 20% with respect to the fatigue cycle are very similar (Figure 5.5). The stiffness for the ECC link slab tested at 55% ± 20% stress level was reduced from 1.85 kN/mm to 1.25 kN/mm – a decrease of about 32% (Table 5.3). The broad band of stiffness fluctuations for ECC links slabs compared to SCC is due to higher stress levels of fatigue loading. The higher stiffness degradation of SCC link slab at low fatigue cycles and low stress levels clearly demonstrates SCC's lower fatigue resistance and strength/stiffness retaining capacity compared to ECC. The sudden transfer of load from concrete to rebar at the onset of a major crack with large crack width is attributed to SCC's such inferior performance.

5.2.1.4 Crack Characterization

Flexural cracks were developed predominantly at mid span of the link slabs from the tension face and gradually propagated towards the compression face (Figure 5.6). The number of cracks were monitored for every 10000 cycles while the crack widths were measured by crack microscope after completing 400000 fatigue cycles. The summary of the crack characteristics in terms of the number of the cracks and averaged crack width for the link slabs at different fatigue stress levels are presented in Table 5.4.

Table 5.4: Crack Characterization of Link Slabs at Different Fatigue Stress Level

Designation	Mean Stress Level	Fatigue Stress Range (%)	Number of cracks after 400 000 fatigue cycle	Crack widths after 400000 fatigue cycle (μm)
LS29-ECC-CI-1.2-MS	40%	±20%	17	100
LS30-ECC-CI-1.2-MS	55%	±20%	16 micro-cracks and 2 major cracks	150 560
LS33-SCC	40%	±5%	1 Major crack	1000

The first cracking appeared during pre-monotonic loading for all ECC link slabs followed by initiation of additional micro-cracks during flexural fatigue loading. In contrast, the first cracking for the SCC link slab tested at 40%±5% stress level appeared at the first fatigue cycle, even though the stress range was reduced to 5%. A major crack formed at the mid-span of the SCC link slab at first fatigue cycle. As the number of the cycles increased, the crack width grew wider and formed a major crack of 1 mm crack width (Table 5.4). The increase of crack width to 1mm after repeated fatigue loading can be attributed to the reduction of the bond strength among the reinforcing bars and the concrete (Zanuy et al. 2011).

In contrast a comparatively large number of cracks (eighteen) cracks were developed during fatigue loading in ECC link slabs. It should be noted that crack widths for all ECC link slabs remained below 560 μm after 400000 fatigue cycle due to fiber bridging phenomena (Table 5.4).

(a) LS29-ECC-CI-1.2-MS (at 40%±20% stress level)   (b) LS30-ECC-CI-1.2-MS (at 55%±20% stress level)
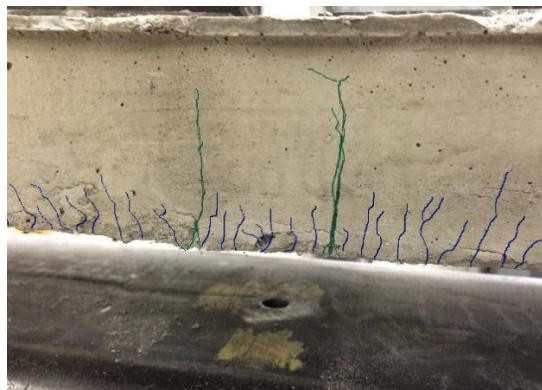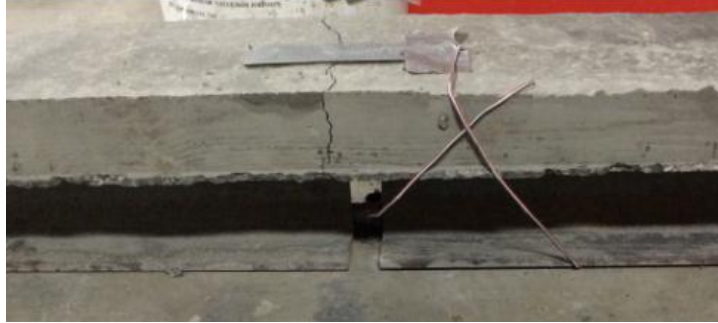
(c) LS33-SCC (at 40%±5% stress level)

Figure 5.6: Crack Propagation of Link Slabs at Different Fatigue Stress Level

It is observed from Figure 5.6 and Table 5.4 that the high fatigue stress level developed higher number of cracks and large crack widths. Micro-cracks were formed initially for the link slab subjected to 55% stress level along with two additional major cracks after the PVA fiber was ruptured at 147000 cycles. The crack widths as it is represented by green colour in Figure 5.6(b) grew wider until it reached 560 μm due to the presence of the reinforcing bar. In contrast the crack widths for the ECC link slab at 40%±20% stress level remained below 100 μm. The lower crack width of ECC link slabs signifies the long-term durability performance of ECC link slabs in bridge deck construction.

5.2.2 Post-Fatigue Monotonic Performance

The exhausted fatigued link slabs tested at different stress levels was subjected to flexural monotonic loading to failure in order to determine the fatigue residual load-deflection response, strength, strain characteristics, energy absorbing capacity and ductility.

5.2.2.1 Load-Deflection/Moment-Rotation Responses and Comparison with Theory

The residual load-deformation and moment-rotation responses of the fatigued link slabs at different stress levels were compared to those of control non-fatigued link slabs in Figures 5.7 and 5.8. Table 5.5a and 5.5b summarizes ultimate load/moment and ultimate deflection/rotation of both SCC and ECC link slabs. Experimental moment capacity of SCC and ECC link slab specimens are compared with those obtained theoretically from Equation 2.15 (described in Chapter 2) in Table 5.5a. The experimental moment capacity of ECC link slab is found to be

1.79 times higher than theoretical because of the contribution of fiber in strength enhancement. This is attributed to the fact that the PVA fiber contribution to the strength enhancement is taken into account conservatively in the theoretical Equation 2.15. On the other hand, theoretically predicted moment capacity of SCC link slab is found to be very close to the experimental value. Equation 2.15 should be modified for the prediction of residual moment capacity of both SCC and ECC link slab subjected fatigue loading by taking into account strength degradation.

Table 5.5a: Summary of Post Fatigue Load-Deflection and Moment-Rotation Responses of the Link Slabs at different Stress Level

Designation	Fatigue Mean Stress Level (%)	Fatigue Stress Range (%)	Ultimate Load (kN)	Ultimate Deflection (mm)	Ultimate Rotation (θ_{ult}) (Radian)	Ratio $\theta_{ult}/\theta_{Allow}$	Expt. Ultimate Moment (M_{ult}) (kN.m)	Ratio M_{ult}/M^{*}_{des}
LS28-ECC-CI-1.2-MS	0	0	12.16	7.59	0.020594	5.49	2.31	1.79
LS29-ECC-CI-1.2-MS	40%	±20%	9.60 (-21%)	3.48 (54%)	0.009425	2.51	1.82	1.45
LS30-ECC-CI-1.2-MS	55%	±20%	5.12 (-58%)	2.31 (69%)	0.006256	1.69	0.97	0.75
LS32-SCC	0	0	5.93	6.74	0.022226	5.92	1.27	1.02
LS33-SCC	40%	±5%	2.57 (-57%)	2.01 (70%)	0.006376	1.7	0.48	0.38

θ_{Allow} represents the maximum allowable AASHTO's rotation of 0.00375 radian
* M_{des} represents design moment calculated based on Eq. 2.15
Value in the brackets represent % strength/deflection reduction compared to control non-fatigued specimens

Table 5.6b: Load levels at Allowable Rotation Limit at different Stress Level

Designation	Fatigue Mean Stress Level (%)	Fatigue Stress Range (%)	Ultimate Load (kN)	Ultimate Rotation (θ_{ult}) (Radian)	Expt. Ultimate Moment (M_{ult}) (kN.m)	M_{exp} at θ_{Allow} (kN.m)	Load level at θ_{Allow}
LS28-ECC-CI-1.2-MS	0	0	12.16	0.020594	2.31	0.65	28%
LS29-ECC-CI-1.2-MS	40%	±20%	9.60	0.009425	1.82	0.75	41%
LS30-ECC-CI-1.2-MS	55%	±20%	5.12	0.006256	0.97	0.85	87%
LS32-SCC	0	0	5.93	0.022226	1.27	1.02	80%
LS33-SCC	40%	±5%	2.57	0.006376	0.48	0.38	80%
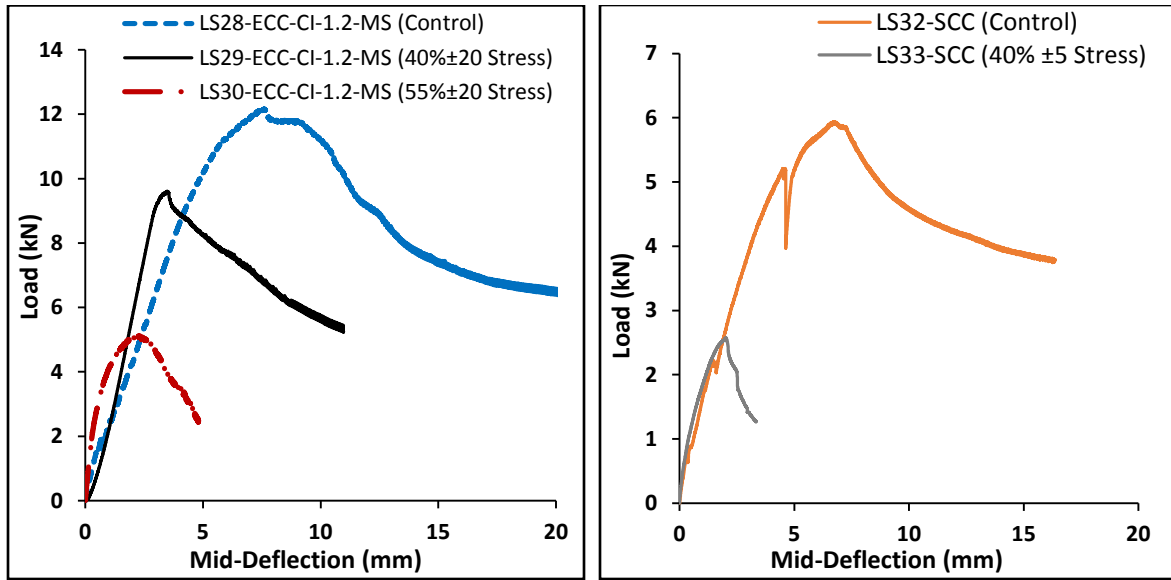
(a) ECC Link Slabs

(b) SCC Link Slabs
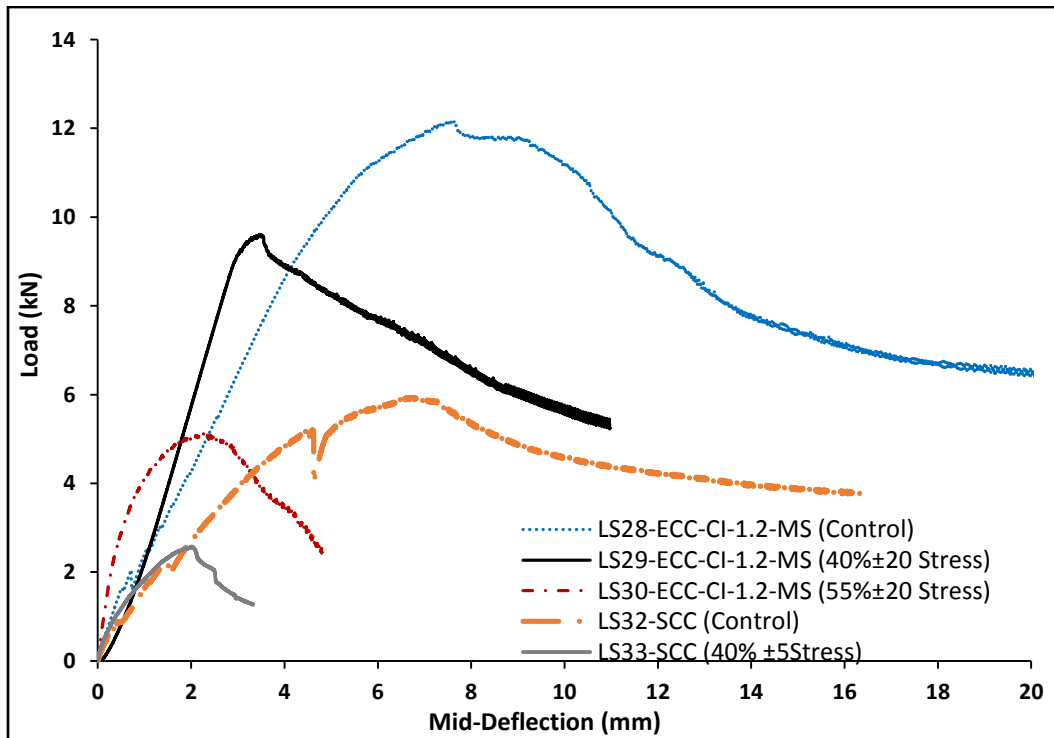
(c) Link Slabs at different fatigue stress level

Figure 5.7: Post Fatigue Load-Deflection Responses of the Link Slabs
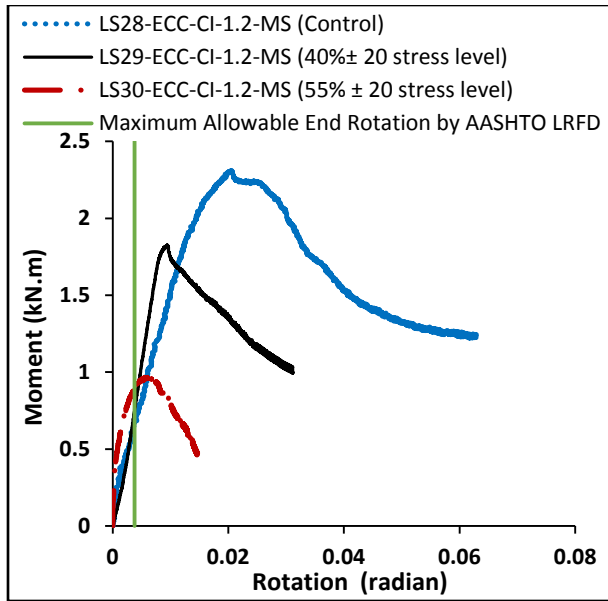
(a) ECC Link Slabs
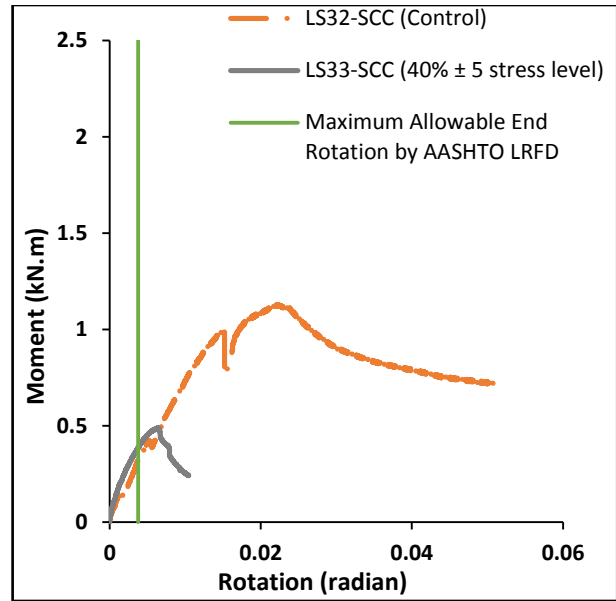
(b) SCC Link Slabs
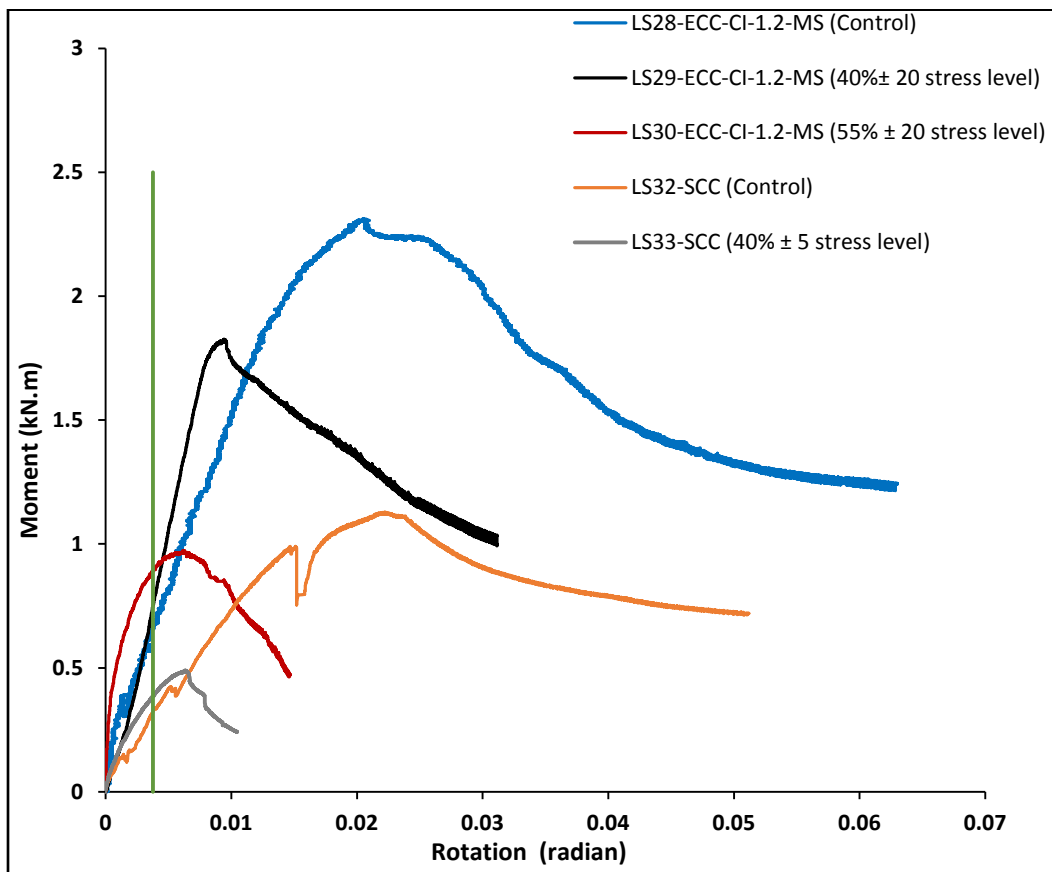
(c) Link Slabs at different fatigue stress level

Figure 5.8: Post Fatigue Moment-Rotation Responses of the Link Slabs

The ultimate load and mid-span deflection envelope of the fatigued link slabs were reduced significantly (showing lower strength and deflection capacities) in compare with their control non-fatigue specimens. The ultimate load and the mid-span deflection for the SCC link slab was reduced by 57% and 70%, respectively in compare to the control specimen (pre-fatigue monotonic specimen) (Table 5.5a). On the other hand, the ultimate load and the mid-span deflection for the ECC link slabs tested at 40%±20% level was reduced by 21% and 54%, respectively – showing significantly better strength and deformation retaining capacity compared to those made with SCC.

This shows that SCC exhibited more damage in compare with the ECC link slabs even though its fatigue stress range was limited to ±5%. The load-deformation response of the SCC link slabs simulates that bending stresses in the post-cracking stages were carried only by the reinforcements. This demonstrates the loss of concrete stiffness under fatigue loading and proves the small residual strength and bending capacity of the SCC link slab was achieved by the reinforcing bar only. In contrast the ECC link slab at the same mean stress level but higher fatigue stress range exhibited greater residual ultimate load and bending capacity (ductility) due to its multiple cracking characteristic and strain hardening behaviour that is attained by the PVA fibers (Suthiwarapirak et al. 2004).

The residual strength and bending capacity for the ECC link slab were reduced significantly at higher stress level (55% ± 20%) by 58% and 69%, respectively (Table 5.5). The steep slope at the post-peak failure of the load-deflection response in Figure 5.7(a) indicates the brittle failure of the ECC link slab at 55% ±20 fatigue stress level. This characteristic demonstrates the loss of the ECC tensile strain hardening, and proves that PVA fibers were ruptured during the fatigue loading. Further, the small increase in residual ultimate load and deflection at the post-monotonic loading was due to the provided minimum steel reinforcing bars. In contrast the strain hardening characteristic of the PVA fibers within the ECC link slab at 40% ± 20% stress levels were maintained since the post-peak failure slope of the load-deflection response was similar to its non-fatigued controlled specimen. Therefore the design fatigue stress level for ECC link slab should be limited to 40% ±20% for satisfying the ultimate and serviceability limit states.

From Figure 5.8, it is evidenced that after fatigue loading, the residual support end-rotations of the damaged link slabs are satisfying the maximum AASHTO LRFD (2012) serviceability limit

of 0.00375 radian at ultimate load. However, the SCC link slab exhibited a since the end-rotation of 0.00375 radian was attained at 80% of the ultimate loading (far above than service load level range of 40%-55%), near the failure point of the specimen (Figure 5.8, Table 5.8b) – hence appeared to be not suitable for link slab applications. In contrast, the ECC link slab at same mean stress level (40%) but higher fatigue stress range (±20%) demonstrated the residual allowable rotation at only 40% of the ultimate load – so even after 400000 fatigue cycles, they satisfy rotation limit). The high residual strength and satisfactory end-rotation retention proved the strain hardening and multiple cracking characteristics of the ECC link slab. The ECC link slab tested at higher fatigue stress level of 55% ±20% showed more damage and attained allowable end-rotation of 0.00375 radian at 87% of the ultimate loading (far above than service load level range of 40%-55%), (Figure 5.8, Table 5.8b). The post-fatigue monotonic tests demonstrated better structural performance of the ECC link slab compared to SCC ones. It should be noted that control ECC link slab (without subjected to fatigue loading) attained allowable end-rotation of 0.00375 radian at only 27% of the ultimate loading (far lower than service load level range of 40%-55%) – this demonstrates superior flexibility of links slab specimens which is essential for such applications).

5.2.2.2 Post-Fatigue Strain Developments

For a comprehensive analysis, the post fatigue residual concrete and rebar strain development are compared with the pre-fatigue and fatigue strain developments for the link slab specimens at different fatigue stress levels. The comparative analysis of concrete and rebar strain development for the ECC and SCC link slab at 40%± 20 and 40%±5 fatigue stress levels are presented in Figures 5.9 and 5.10, respectively. Also the summary of the residual strain development at the ultimate load for the fatigued link slabs at different stress levels are presented in Figure 5.11 and Table 5.6.
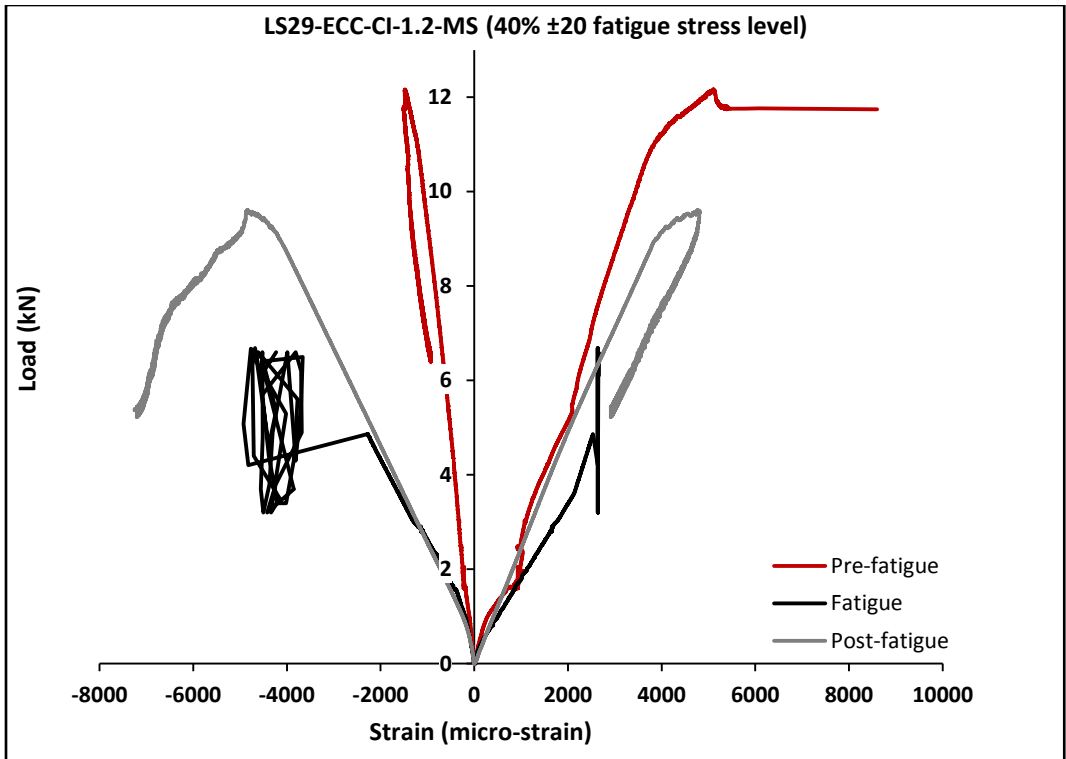
(a) Concrete strain for LS-29-ECC-CI-1.2-MS (40%±20)
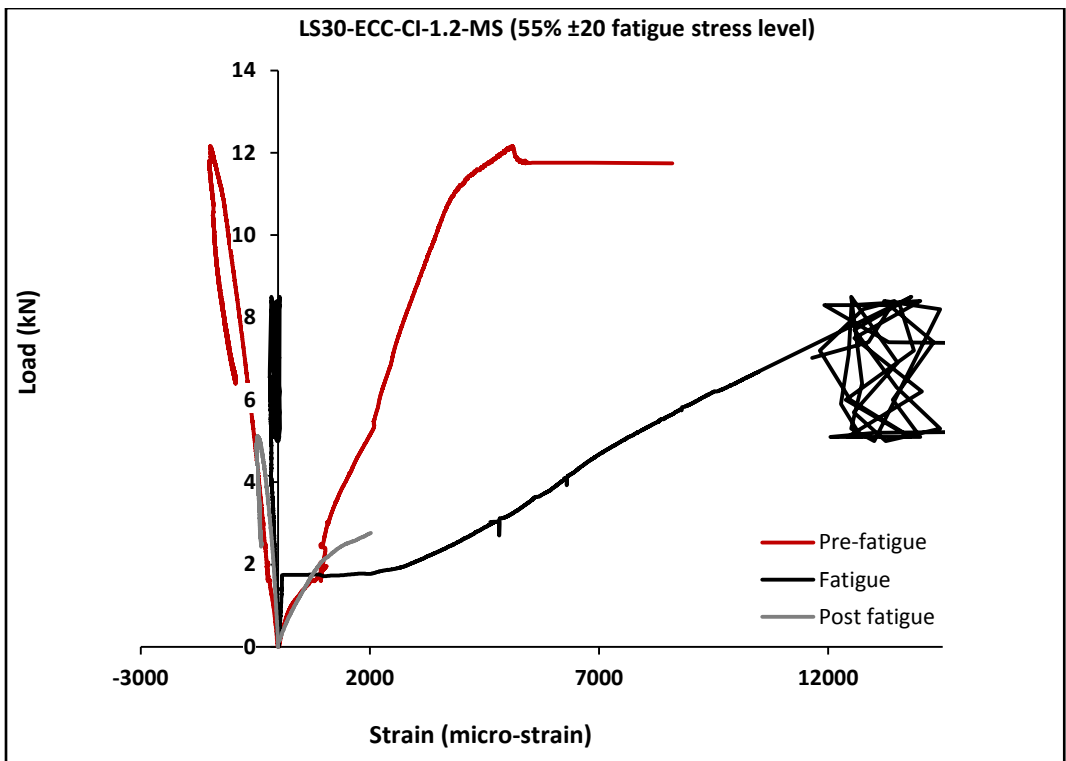
(b) Concrete strain for LS-30-ECC-CI-1.2-MS (55%±20)

94
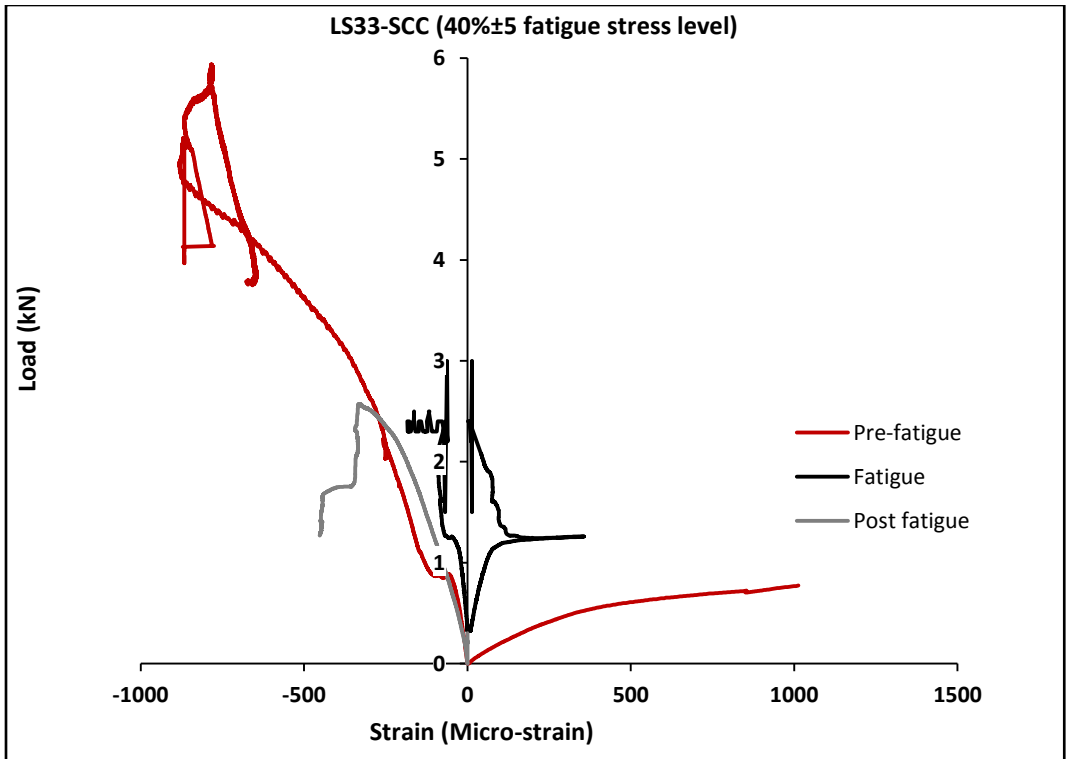
(c) Concrete strain for LS33-SCC (40%±5)

Figure 5.9: Concrete Strain Development at Pre-Fatigue, Fatigue and Post-Fatigue of Link Slabs at Different Fatigue Stress Levels
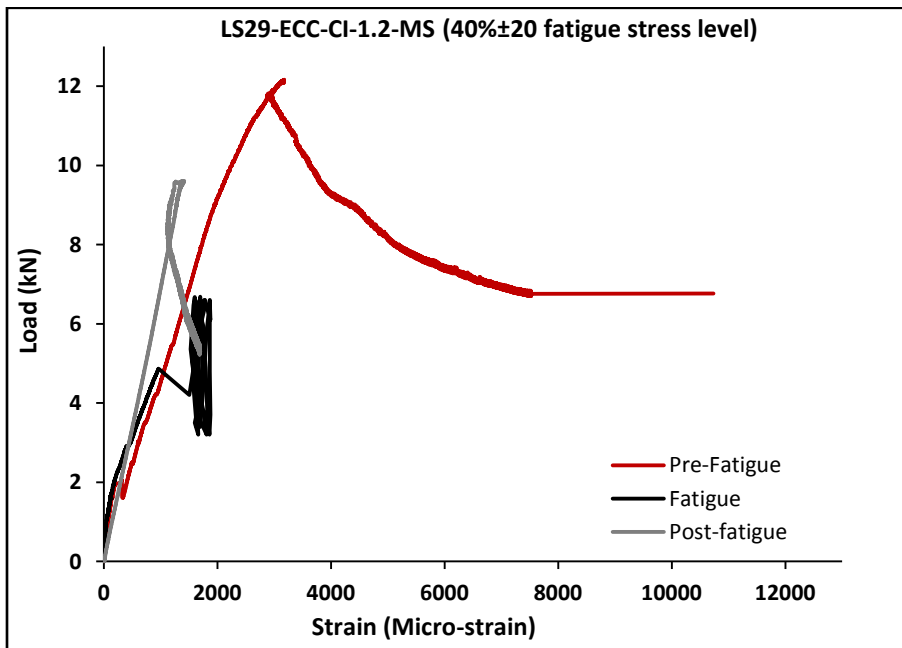
(a) Rebar strain for LS-29-ECC-CI-1.2-MS (40%±20)
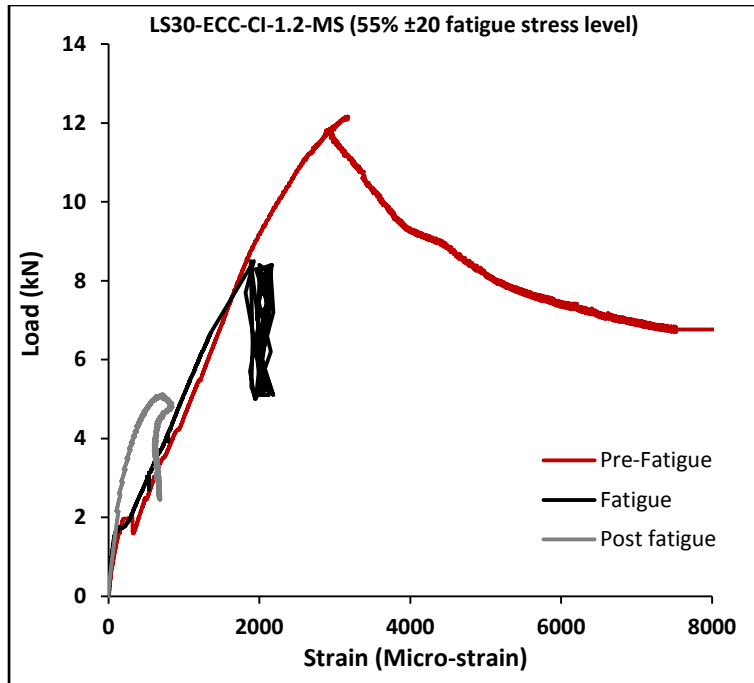
(b) Rebar strain for LS-30-ECC-CI-1.2-MS (55%±20)
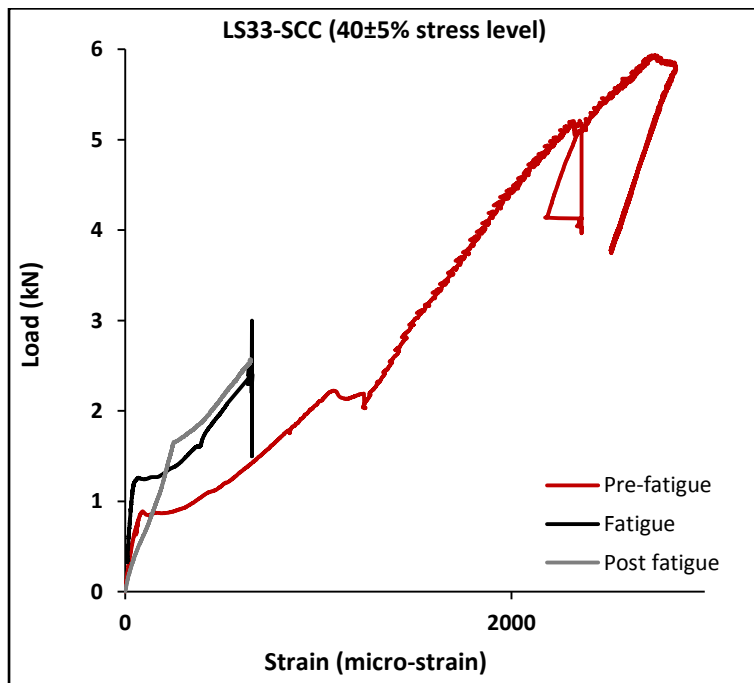
(c) Rebar strain for LS33-SCC (40%±5)

Figure 5.10: Rebar Strain Development at Pre-Fatigue, Fatigue and Post Fatigue of Link Slabs at Different Fatigue Stress Level
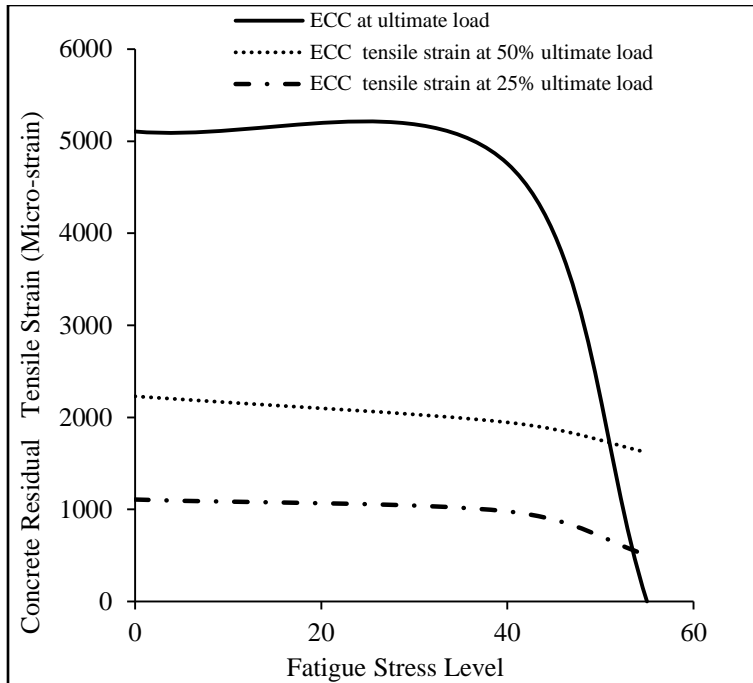
(a) Concrete Tensile Strain
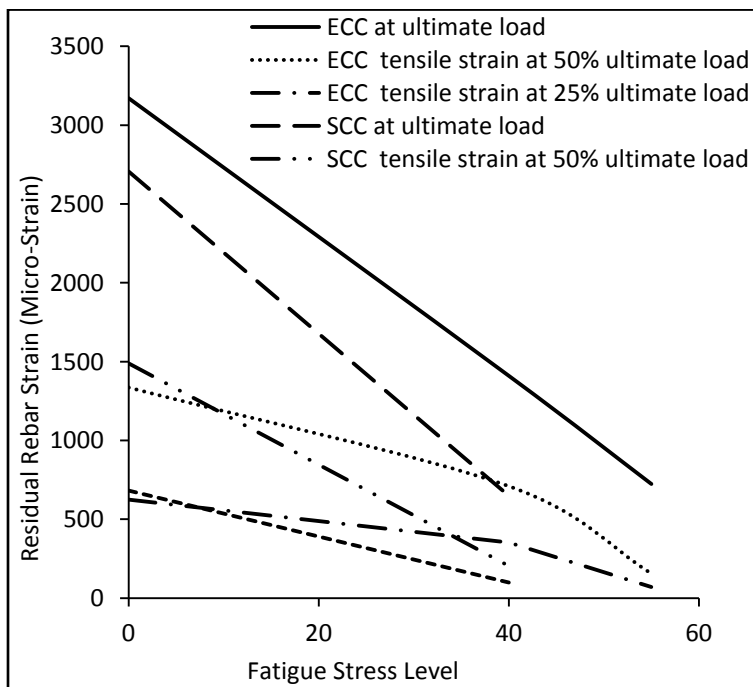
(a) Rebar Strain

Figure 5.11: Summary of Post Fatigue Strain Developments for Link Slabs Subjected to Different Fatigue Stress Level

Table 5.7: Post Fatigue Strain Developments for the Link Slabs at Different Fatigue Stress Level

Designation	Fatigue Mean Stress Level (%)	Fatigue Stress Range (%)	Tensile Strain at Ultimate Load (Micro-Strain)	Rebar Strain at Ultimate Load (Micro-Strain)	Compressive Strain at Ultimate Load (Micro-strain)
LS28-ECC-CI-1.2-MS	0	0	5106	3172	-1481
LS29-ECC-CI-1.2-MS	40	±20	4777 (-6%)	1368 (-57%)	-4855
LS30-ECC-CI-1.2-MS	55	±20	0*	724 (-77%)	-4465
LS32-SCC	0	0	0*	2723	-783
LS33-SCC	40	±5	0*	651 (-76%)	-329

*damaged

The post fatigued strain development (in concrete and steel) for the link slab specimen was significantly lower in compare with the non-fatigued controlled link slabs (pre-fatigued specimens) (Figure 5.9-5.11). In general, strain (both concrete and steel) decreases with the increase of stress level (Figure 5.11). At the onset of concrete cracking in the SCC link slab, the stress is transferred to the steel rebar causing high stress development and subsequent yielding at failure load (as evident from 2723 micro-strain, Table 5.6). During fatigue loading, the loss of concrete tensile strain due to the crack formation for the SCC link slab resulted as a tension stiffening at the end of the first cycle which caused the bond reduction between the concrete and the rebar (Chen et al. 2011; ACI ,1992). The loss of concrete tensile strain and the transferred stresses to the rebar caused the significant plastic deformation for the rebar. From Figure 5.10(c), it is observed that for the same reinforcing ratio, the residual rebar strain for the SCC was significantly lower in compare with the ECC link slab (Figure 5.10a), even though the peak stress range for the ECC was 15% higher than SCC link slab. The small residual rebar strain (651 micro-strain) in compare to the pre-fatigue rebar strain development indicated the bond degradation of steel-SCC due to fatigue loading. Based on the characteristics of the residual rebar strain, it is proved that the failure of the SCC link slab was dependent to the performance and failure of the rebar (Zanuy et al. 2011). In contrast, the high residual rebar strain for the ECC link slab (Figure 5.10a and Table 5.6) in compare with the pre-fatigue monotonic rebar strain development demonstrate the active presence of the concrete tensile strain during the fatigue loading. Although the concrete tensile strain was reduced in compare with the non-fatigued ECC link slab, but the loss of both concrete and rebar strain was not significant. The high residual

strain development of the fatigued ECC link slabs proves ECC's stiffness remains unchanged during the fatigue loading (Li, 2004).

As it is observed from Figure 5.9 (b), the ECC link slab subjected to 55% mean fatigue stress level exhibited a similar residual strain development like SCC. Low residual ECC tensile strain development (Figure 5.9b), and small residual rebar strain (Figure 5.10b) is observed for the ECC link slab at 55% mean fatigue stress level. The high stress fatigued loading ruptured the PVA fiber at early fatigue cycle which caused the stress transfer to the reinforcing bar. The accumulation of the internal defects, such as formation of larger crack width prior to 147000 fatigue cycles resulted in an increased plastic deformation and degradation of the steel rebar. In contrast the residual concrete tensile and rebar strain development for the ECC link slab at 40% mean fatigue stress level was 6% and 57%lower than the non-fatigued control specimens (Table 5.6). Based on the residual strain characteristic it is suggested to limit the design mean fatigue stress level to 40%±20 % in order to increase the service life of the link slab.

5.2.2.3 Energy Absorbing Capacity and Ductility Index
The energy ductility index and the energy absorbing capacity of the non-fatigued and fatigued ECC and SCC link slabs subjected monotonic loading to failure are summarized in Table 5.7.

Table 5.8: Energy Absorption and Ductility Index of Link Slabs at Different Fatigue Stress Levels

Designation	Fatigue Cycle	Fatigue Mean Stress Level	Fatigue Peak Stress Amplitude	Energy (Joules)	Ductility Index
LS28-ECC-CI-1.2-MS	0	0	0	93.125	37.220
LS29-ECC-CI-1.2-MS	400000	40%	±20%	31.372	16.902
LS30-ECC-CI-1.2-MS	400000	55%	±20%	13.293	2.298
LS32-SCC	400000	0	0	35.62	13.477
LS33-SCC	400000	40%	±5%	4.035	2.522

From Table 5.7, it can be noted that the fatigued link slabs had shown lower residual energy absorbing capacity and ductility index than non-fatigued control specimens. Non-fatigued ECC

link slabs showed 2.6 and 2.7 times higher energy absorbing capacity and ductility index than their SCC counterparts. ECC link slabs also exhibited higher post-fatigues residual energy absorbing capacity and ductility than their SCC counterparts at both low and high fatigue stress levels. Even at higher fatigue stress level of 40%±20%, the ECC link slab demonstrated 7.85 and 6.70 times higher energy absorbing capacity and ductility index, respectively compared with the SCC link slab (tested at 40%±5% stress level).

The structural response of the ECC link slabs at 55% ±20% fatigue stress level was similar to the SCC specimen at 40%±5%. The energy absorbing capacity and ductility index of the ECC link slab at 55% ± 20 were 13.3 joules and 2.3, respectively which is 86 lower than the pre-fatigued control specimen and 58% lower than the link slab specimen subjected to t 40%±20% stress level (Table 5.7).

The low residual energy absorbing capacity and ductility of the ECC link slab at 55%±20 fatigue stress level confirmed the brittleness of the specimen due degradation and accumulated damage. The Canadian Highway Bridge Design Code CHBDC (2006) limits the maximum fatigue stress level to 65% for the concrete bridge deck. Therefore based on the observed characteristics, it is recommended to limit the maximum design fatigue stress level of the ECC link slab within the elastic range up to maximum 60% of ultimate capacity of the link slab.

5.3 Behaviour ECC Link Slabs subjected to Different Fatigue Cycles at Constant Fatigue Stress Level

This section presents the results for the structural performance of ECC link slabs subjected to different fatigue cycles of 400000 and 1000000 at the fixed stress level of 40% ± 20%. It was decided to test the ECC specimens only due to the weak response of the SCC link slab subjected to flexural fatigue loading up to 400000 cycles.

5.3.1 Fatigue Performance

5.3.1.1 Load-Deflection Response and Deflection Evolution

The load-deflection response and deflection evolution of ECC link slab specimens subjected to 400000 and 1 million fatigue cycles are illustrated in Figures 5.12 and 5.13. The results of deflection evolution is summarized in Table 5.8.
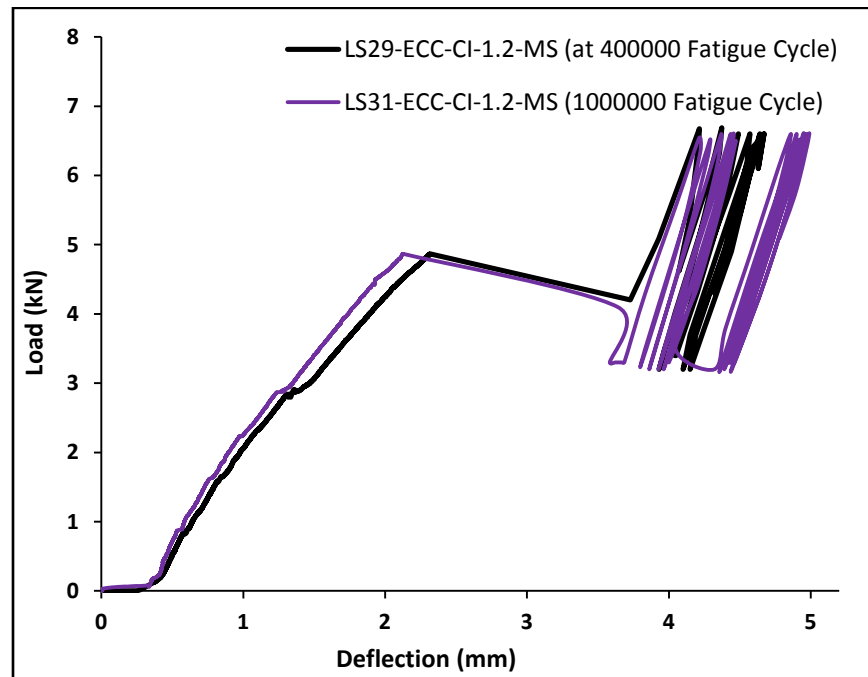
Figure 5.12: Load-Deformation Responses of ECC Link Slabs at Different Fatigue Cycles
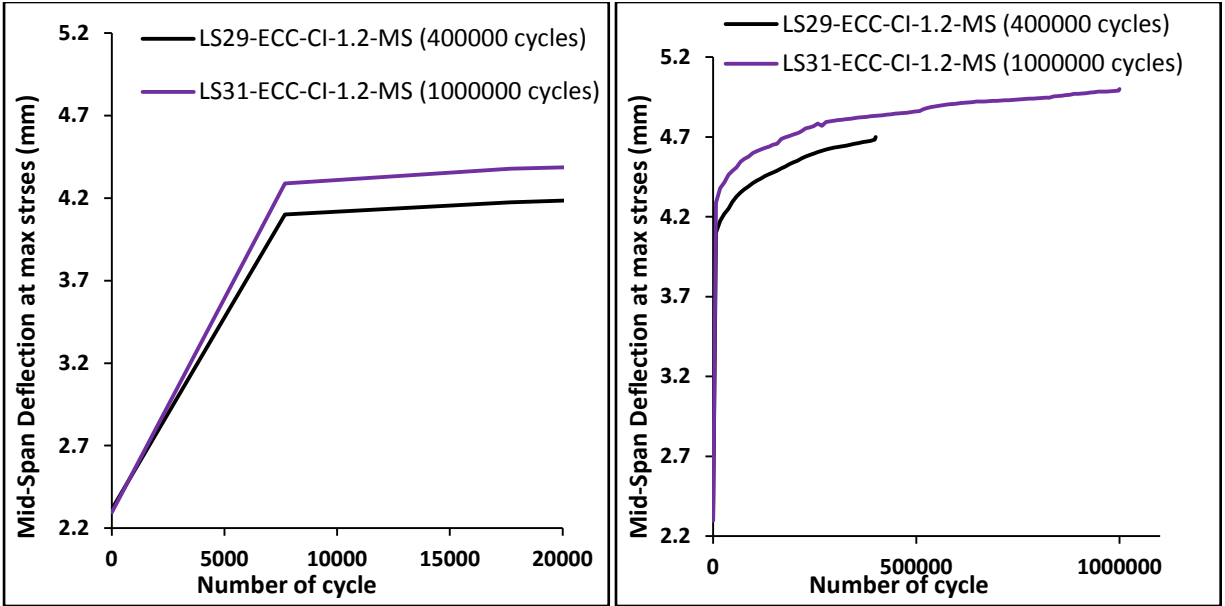
(a) Initial 10000Fatigue Cycle   (b) Full Fatigue Cycle

Figure 5.13: Mid-Span Deflection Evolution of ECC Link Slabs at Different Fatigue Cycles

Table 5.9: Mid-Span Deflection Evolution at Different Fatigue Cycles

Designation	Fatigue Cycle	Difference Between First and Initial 10000Fatigue Cycle Mid-Span Deflection (mm)	Fatigue Cycles	Difference Between First and Last value of Mid-Span Deflection (mm)
LS29-ECC-CI-1.2-MS	10000	1.787	400000	2.39
LS31-ECC-CI-1.2-MS	10000	1.850	1000000	2.87

Figure 5.12 shows the formation of large deflection band width for the ECC link slab subjected to higher number of fatigue cycles. The deflection band width of link slab subjected to the 1 million fatigue cycles increased from 2.1 mm to 5 mm, whereas the band width for the ECC link slab at 400000 cycle varied from 2.2 mm to 4.59 mm. The larger bending capacity is also justified through Figure 5.13 (b) due to increase in mid-span deflection evolution at maximum stress level. Once again the development higher deflection evolution (bending capacity) at higher fatigue cycles (1 million cycle) is attributed to the fiber bridging characteristics of the ECC.

Although the link slab at higher fatigue cycle deflected more, but the change in deflection evolution with respect to 400000 fatigue cycle was not significant; it only deflected 0.41 mm more. It is clearly observed that the increase in deflection evolution was higher for both link slabs at the initial fatigue cycles (Figure 5.13 and Table 5.8) due to the increased stress shift from pre-monotonic to fatigue loading. However with increasing fatigue cycle the mid-span deflection evolution becomes negligible in compare with initial fatigue cycle. The gradual increase in deflection evolution specifically after 700000 fatigue cycle demonstrates the rupture of fibers.

5.3.1.2 Strain Development

The concrete and rebar strain development for the ECC link slabs at different fatigue cycles was recorded during the fatigue loading. The key features of concrete (tensile and compressive) and rebar strain developments for the ECC link slabs at different fatigue cycles of 400000 and 1 million are tabulated in Table 5.9. The concrete and steel strain evolution with load and number of fatigue cycles is illustrated in Figures 5.14 and 5.15.

Table 5.10: Strain Development of Link Slab During Fatigue Performance at Different Fatigue Cycle

Designation	Fatigue Cycle	Initial Concrete Tensile Strain (Micro-Strain)	Final Concrete Tensile Strain (Micro-Strain)	Initial Concrete Compressive Strain (Micro-Strain)	Final Concrete Compressive Strain (Micro-Strain)	Initial Rebar Strain (Micro-Strain)	Final Rebar Strain (Micro-Strain)
LS29-ECC-CI-1.2-MS	400000	2536.1	2647.1	-2281.5	-4227.3	961.3	1782.1
LS31-ECC-CI-1.2-MS	1 million	2643.0	3234.3	-2010.7	-2207.3	1038.5	2093.5
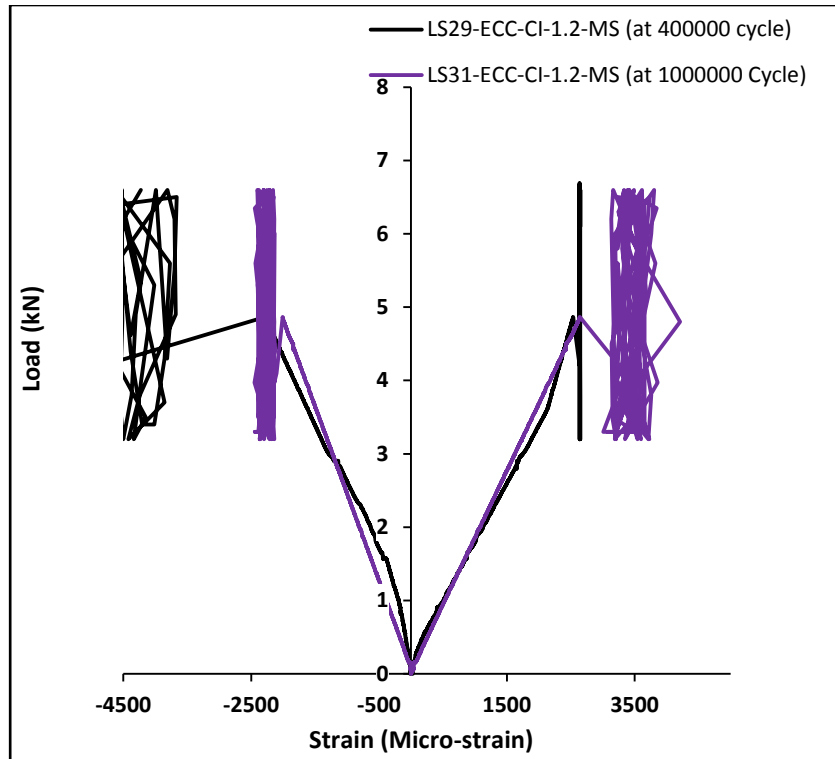
(a) Concrete Tensile/Compressive Strain
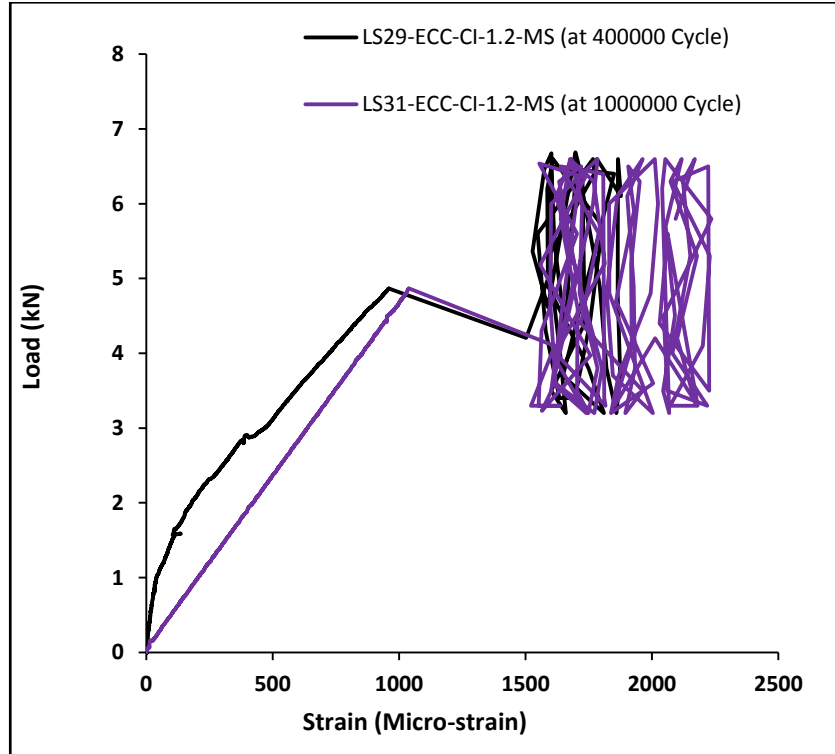
(b) Rebar Strain

Figure 5.14: Strain Development for ECC Link Slabs at Different Fatigue Cycles

(a) Concrete Tensile Strain   (b) Rebar Strain
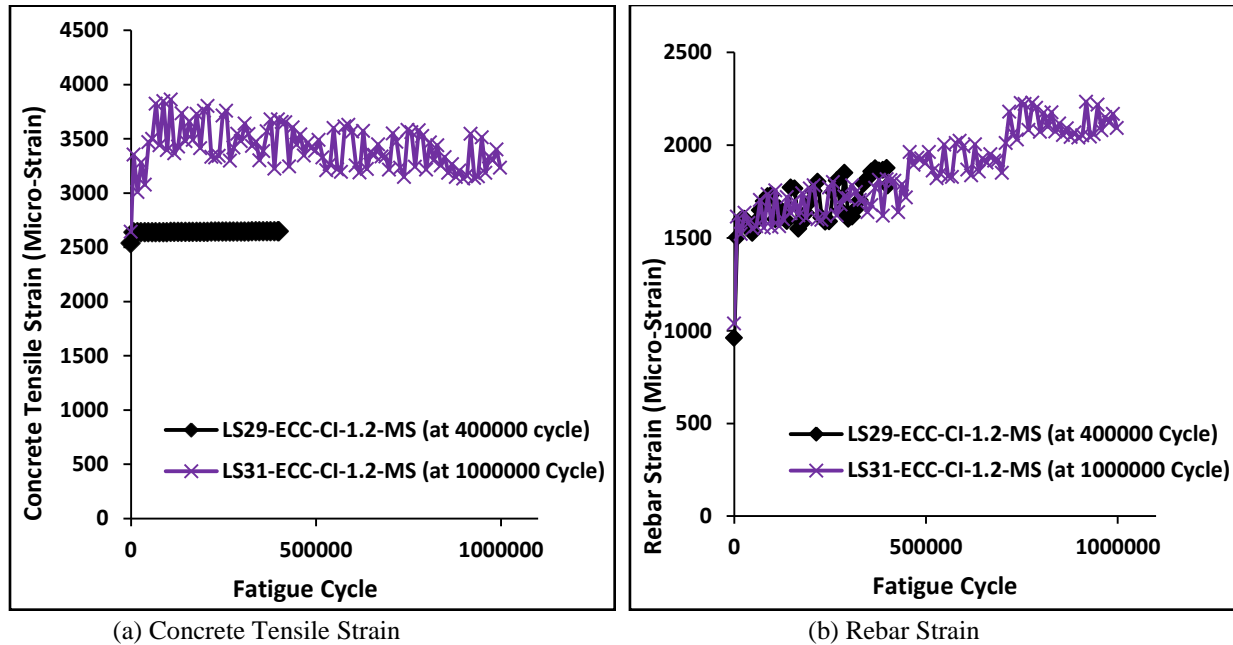
Figure 5.15: Strain Development Evolution of ECC Link Slabs at Different Fatigue Cycle

From Figure 5.14, it is observed that ECC link slab at 400000 fatigue cycles developed lower tensile strain band width (strain development) compared with that subjected to 1million fatigue cycle. The ECC tensile strain band for link slab subjected to 1million fatigue cycle was increased from 2643 micro-strain to 3234 micro-strain during the fatigue loading. On the other hand, the ECC tensile strain band width for the link slab subjected to 400000 fatigue cycles increased from 2536 micro-strain to 2647 micro-strain (Table 5.9). The larger concrete tensile band at 1 million cycles demonstrated higher damage level in compare with the ECC link slab at 400000 fatigue cycles. Although the damage level was increased at 1 million cycles but the tensile strain did not reach ECC's ultimate tensile strain capacity of 0.05 (means ECC can endure more fatigue cycles) and suffered much lower degradation compared to what observed for SCC link slab subjected to 400000 cycles.

Similar pattern was also observed for the rebar strain development for the ECC link slab at 1million fatigue cycles (Figure 5.14b). The rebar strain band width for the ECC link slab at 1million fatigue cycle increased from 1038 micro-strain to 2093 Micro-strain during fatigue loading (Figure 5.14b and Table 5.9). The rebar strain reached the yielding strain of 2000 micro-strain at 700000 fatigue cycle as it is evidenced from Figure 5.15(b). The strain development and

105

deflection evolution characteristics confirmed initiation of rebar yielding at 700000 fatigue cycles – an indicator of degradation of strength and stiffness of ECC link slabs.

5.3.1.3 Stiffness Evolution

The variation of stiffness with number of fatigue cycles up to 1 million is presented in Figure 5.16.
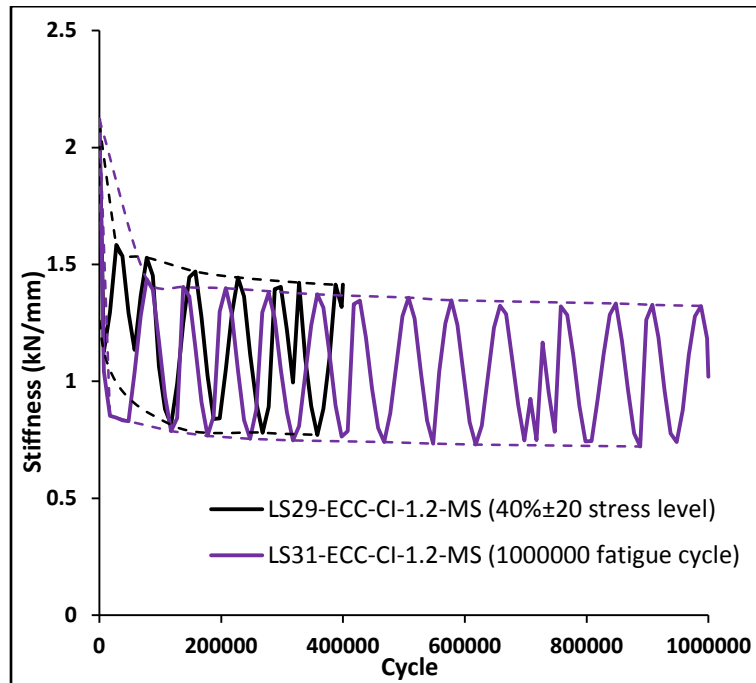
Figure 5.16: Stiffness Degradation of Link Slab Specimens at Different Fatigue Cycles

As previously discussed, the stiffness degraded significantly for the initial fatigue cycle due to concrete crack formation caused by high fatigue stress range (±20%). However with fiber bridging characteristic the stiffness of the link slabs were stabilized and a gradual decrease in stiffness with increasing fatigue cycle is observed (as indicated by the dotted lines connecting the upper and lower peak points) showing the variation of stiffness. The oscillating stiffness pattern was due to the stress level range (±20% from the mean 40%). Table 5.10 summarizes the initial and final stiffness of link slab specimens subjected to different fatigue cycles of 400000 and 1 million.

106

Table 5.11: Stiffness Degradation of Link Slab Specimens at Different Fatigue Cycles

Designation	Fatigue Cycle	Initial Stiffness (kN/mm)	Stiffness at end of fatigue cycle (kN/mm)
LS29-ECC-CI-1.2-MS	400000	2.10	1.42
LS31-ECC-CI-1.2-MS	1000000	2.1	1.01

The initial stiffness for the ECC link slab at 1million fatigue cycle was 2.193 kN/mm and at the end of the fatigue loading (end of 1million fatigue cycle) it was reduced to 1.01 kN/mm showing a decrease of about 54% (Table 5.10). At 700000 fatigue cycle, the stiffness was reduced to 0.7 kN/mm, but it recovers to 1.2 kN/mm (Figure 5.16). This demonstrates that PVA fibers were ruptured at 700000 fatigue cycle and the stiffness recovery was attained by the presence of steel reinforcement (stress transfer mechanism). It can also be derived from Table 5.10 that the stiffness was reduced by 32% at 400000 cycles. Such degradation of stiffness with increased fatigue cycles (as observed in this study) can be used to predict the service life (in terms of cycles needed to degrade the stiffness to zero) of the link slab specimens.

5.3.1.4 Crack Characterization

The cracking information were monitored at the end of every 10000 cycles. The number of cracks and the crack width at mid-span location were recorded at the end of the fatigue performance. The experimental results for the crack characterization are presented in Table 5.11 and the development of cracks in the link slab is shown in Figure 5.17.

Table 5.12: Crack Characterization of the ECC Link Slab at Different Fatigue Cycle

Designation	Fatigue Cycles	Number of cracks after 400 000 fatigue cycle	Crack widths after 400000 fatigue cycle (μm)
LS29-ECC-CI-1.2-MS	400000	17 Micro-Crack	100
LS31-ECC-CI-1.2-MS	1000000	24 Micro-Crack	250
		1 Major Crack	550
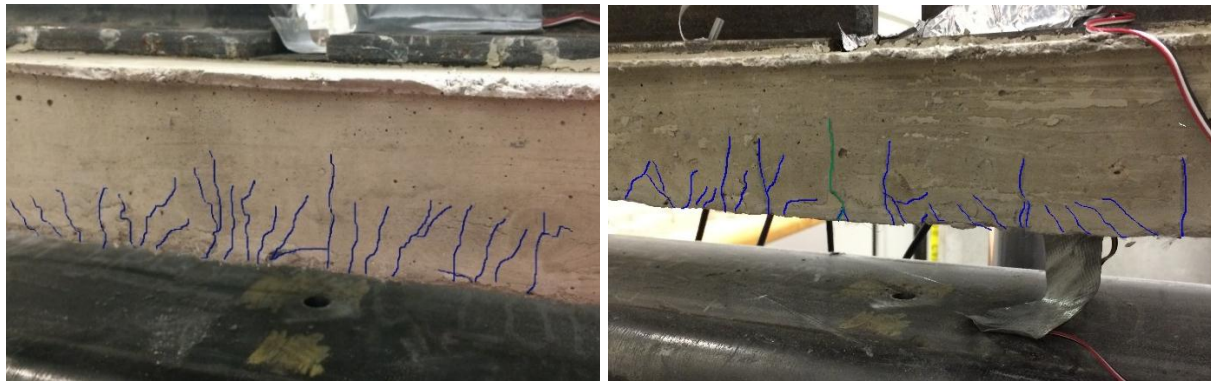
(a) LS29-ECC-CI-1.2-MS (at 400000 fatigue Cycle)   (b) LS31-ECC-CI-1.2-MS (at 1000000 fatigue cycle)

Figure 5.17: Crack Characterization of ECC Link Slabs at Different Fatigue Cycle

At initial fatigue cycle, multiple-micro cracks were initiated due to the stress shift from pre-monotonic to fatigue loading. Additional micro-cracks were propagated at the mid-span location with increasing number of the fatigue cycles. As it is evidenced from Figure 5.17(b), a major crack was developed at the mid-span location of link slab at 500000 fatigue cycle. The crack width increased significantly until the PVA fibers were ruptured at 700000 fatigue cycle. The ruptured PVA fibers through the cracks – a sign of damage in ECC, but ECC link slabs continued to take 1 million cycles. On unloading after 1 million cycles, the crack widths remained below 550 µm. The small crack width demonstrated the combined contribution of aggregate interlocking and crack bridging characteristic of the PVA fibers (Hossain & Anwar, 2014). Although the major crack width for the ECC link slab at 1million fatigue cycle is above the limitation of AASHTO's LRFD (2012) and CHBDC (2006), yet it still can maintain adequate durability requirement.

5.3.2 Post Fatigue Monotonic Performance of ECC Link Slabs at Different Fatigue Cycles
At the end of the fatigue flexural loading, the ECC link slab specimens were tested under monotonic loading to failure for determining the residual strength, deflection, stiffness and failure characteristics compared with the control non-fatigued counterparts.

5.3.2.1 Experimental Load-Deflection/Moment-Rotation Responses and Theoretical-Code Based Analysis

The summary of residual load-deformation and moment rotation responses of the ECC link slabs at different fatigue cycles are compared with those of non-fatigued control specimens Figures 5.18 and 5.19.
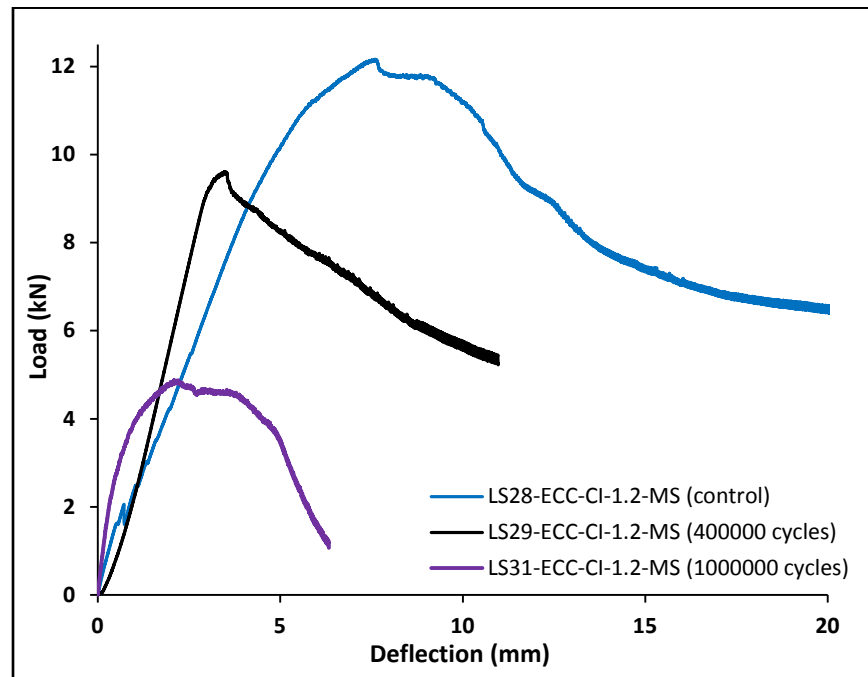
Figure 5.18: Post Fatigue Load-Deformation Response of ECC Link Slabs at Different Fatigue Cycle

The ultimate strength and mid-span deflection reduced significantly with increasing number of the fatigue cycle. The ECC link slab at 400000 fatigue cycle maintained 79% of the ultimate strength and 46% of the bending capacity of non-fatigued control specimen. On the other hand, at 1 million fatigue cycle both strength and mid-span deflection were reduced to 40% and 27% compared with the non-fatigued control specimen, respectively (Table 5.12).   Strength and bending capacity degradation of the fatigued specimens especially at high fatigue cycles were attributed to the lowering of crack bridging ability due to the rupture PVA fiber, stress transfer from ECC to rebar, crack closing and opening during fatigue loading and steel-ECC bond degradation.

Table 5. 13: Residual Load-Deformation and Moment-Rotation Responses of ECC Link Slabs at Different Fatigue Cycles

Designation	Fatigue Cycle	Ultimate Load (kN)	Ultimate Deflection (mm)	Ultimate Rotation θ_{exp} (radian)	Ratio $\theta_{exp}/\theta_{Allow}$	Ultimate Moment (Mex) (kN.m)	Ratio M_{ex}/M^*_{des}	M_{exp} at θ_{Allow} (kN.m)	Ratio M_{exp} at θ_{Allow}/M_{ex}
LS28-ECC-CI-1.2-MS	0	12.16	7.60	0.020594	5.49	2.31	1.79	0.65	0.28
LS29-ECC-CI-1.2-MS	400000	9.61 (-21%)	3.48 (-54%)	0.009425	2.51	1.83	1.45	0.73	0.40
LS31-ECC-CI-1.2-MS	1000000	4.87 (-60%)	2.09 (-73%)	0.006223	1.65	0.925	0.72	0.8	0.86

θ_{Allow} represents the maximum allowable AASHTO's rotation of 0.00375 radian

*M_{des} calculated by Equation 2.15

*values in brackets represents % reduction of ultimate load and deflection compared to non-fatigued specimens
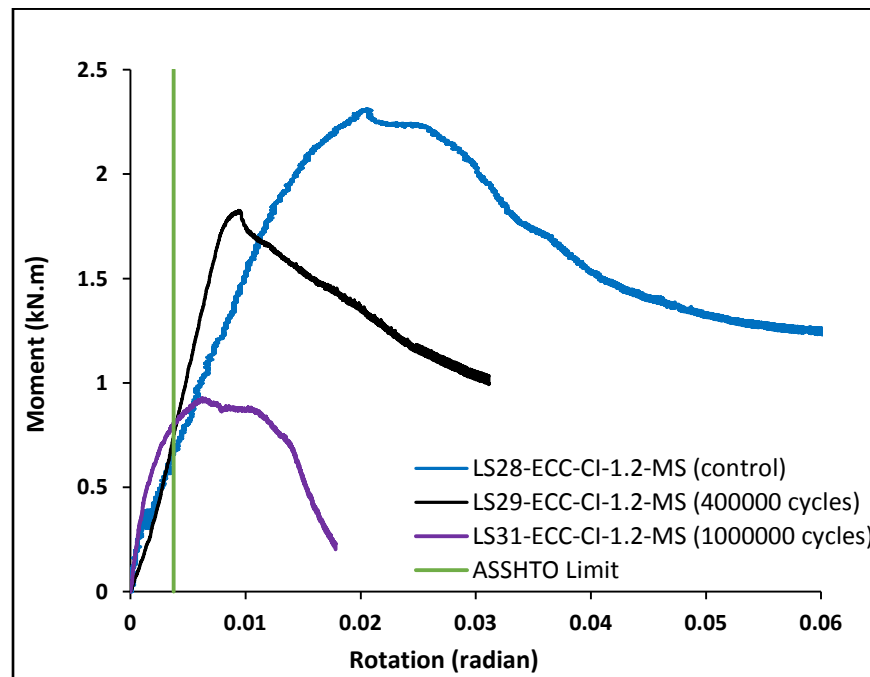
Figure 5 19: Residual Moment-Rotation Responses of ECC Link Slab at Different Fatigue Cycle

Figure 5.19 compares the residual moment-rotation responses fatigued specimens compared with non-fatigued control ones. As expected, at higher fatigue cycles the moment capacity and support rotation decreased due to the development of more fatigue damages. Although for the purpose of the link slab, the moment capacity is not a significant parameter in compare with the end-rotation, but a reasonable factor of safety with respect to the design moment is required for failure prevention. Through the comparison of the experimental to theoretical design moment (based on Equation 2.15), it is observed that at 1 million fatigue cycle, the factor of safety for the ultimate moment was reduced to 0.72 (ratio of experimental to theoretical values) in compare with 1.45 for the link slab specimen subjected to 400000 fatigued cycle (Table 5.12). The factor of safety of below 1 can be used to justify the failure of the link slab at 1million fatigue cycle.

At higher fatigue cycles, the residual support end rotation of the link slab satisfied the maximum allowable AASHTO's LRFD end rotation of 0.00375 radian, but with lower factor of safety of 1.65 (Table 5.12). As it is evidenced from Figure 5.19 and Table 5.12 the AASHTO's design end rotation for the 1 million fatigue cycle link slab was attained at 86% of the ultimate moment, close to the failure. Whereas the end rotation for ECC link slab at 400000 fatigue cycle was achieved at 40% of the ultimate load. Therefore the design fatigue cycle for the ECC link slab at 4 Hz amplitude and 40% ±20% fatigue stress level has to be limited to 700000 cycle (at the initiation of yielding of steel) for satisfying both ultimate and fatigue limit state design.

5.3.2.2 Strain Developments

The concrete and rebar strain development for the ECC link slabs at different fatigue cycles at three stages of non-fatigued, fatigued and post-fatigue are illustrated in Figures 5.20 and 5.21. Table 5.13 summarizes ultimate residual strain developments of the fatigued link slabs at different cycles.
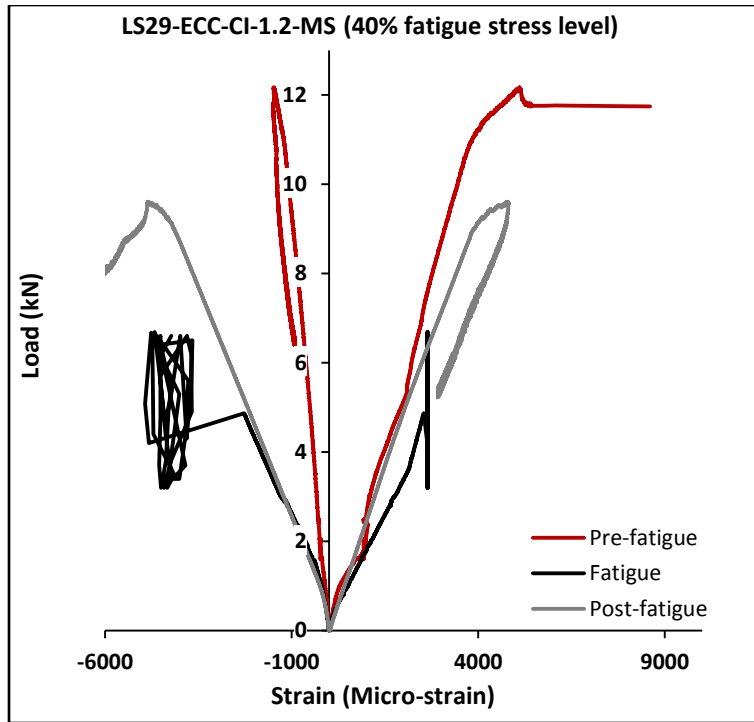
(a) Concrete strain LS-29-ECC-CI-1.2-MS (400000)
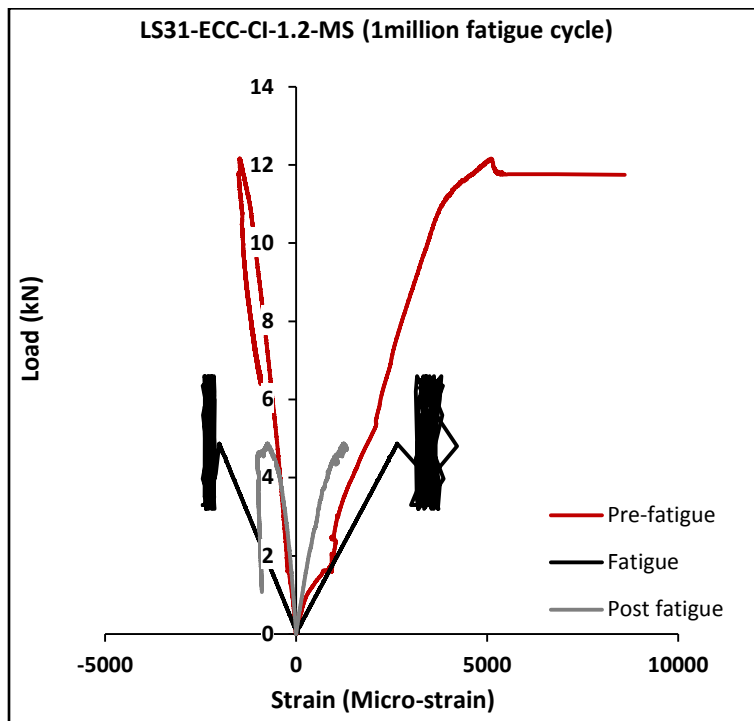
(b) Concrete strain LS31- ECC-CI-1.2-MS (1million)

Figure 5.20: Post Fatigue Concrete Strain Development for the ECC Link Slabs at Different

Fatigue Cycle

112
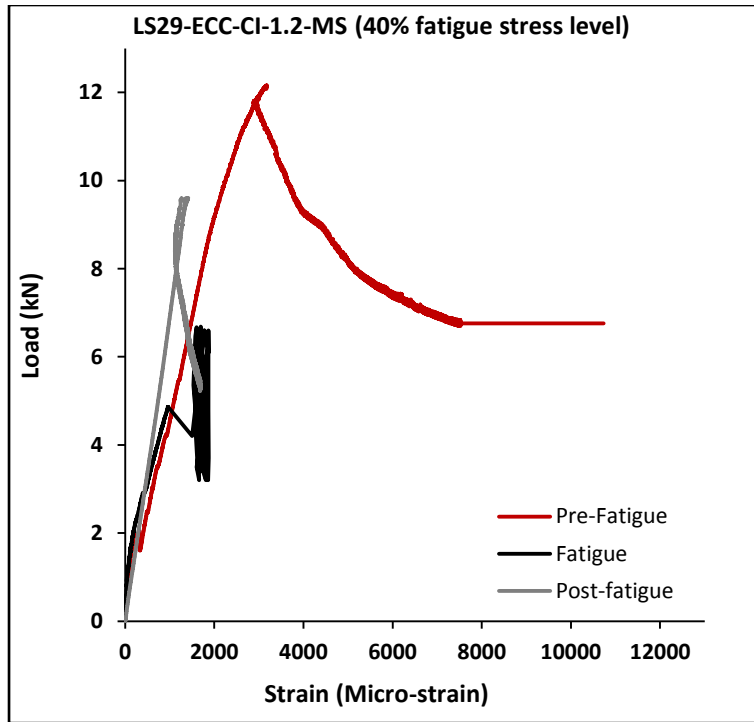
(a) Rebar strain LS-29-ECC-CI-1.2-MS (400000)
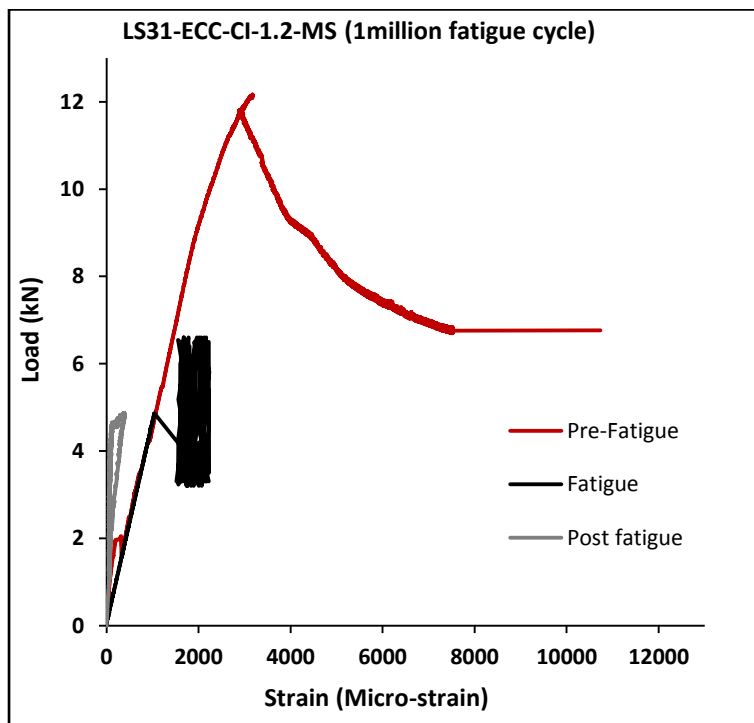
(b) Rebar strain LS31- ECC-CI-1.2-MS (1million)

Figure 5.21: Post Fatigue Rebar Strain Development for the ECC Link Slabs at Different Fatigue Cycle

Table 5.14: Residual Strain Development of the ECC Link Slab at Different Fatigue Cycle

Designation	Fatigue Cycle	Ultimate Load (kN)	Ultimate Tensile Strain (Micro-Strain)	Ultimate Rebar Strain (Micro-Strain)	Ultimate Compressive Strain (Micro-Strain)
LS28-ECC-CI-1.2-MS	0	12.164	5106	3172	-1481
LS29-ECC-CI-1.2-MS	400000	9.609	4777.02	1368.08	-4855.08
LS31-ECC-CI-1.2-MS	1000000	4.873	0*	386.314	-739.581

*Strain gauge damaged

As per Figure 5.20 and 5.21, both concrete and rebar strain development are found to be reduced significantly with increasing number fatigue cycles due to accumulated damage during fatigue loading causing reduction of strength and bending capacity. The rebar strain was reduced to 386micro-strain – a reduction of about 88% compare with the non-fatigued link slab specimen (Table 5.13).

5.3.2.3 Energy Absorbing Capacity and Ductility Responses

The summary of the residual energy absorbing capacity and the ductility index for the fatigued ECC link slab at different cycles are presented in Table 5.14

Table 5.15: Residual Energy Absorbing Capacity and Ductility Index of the ECC Link Slabs at Different Fatigue Cycle

Designation	Fatigue Cycle	Energy Absorbing Capacity (J)	Ductility Index
LS28-ECC-CI-1.2-MS	0	93.13	37.22
LS29-ECC-CI-1.2-MS	400000	31.37	16.90
LS31-ECC-CI-1.2-MS	1000000	16.00	4.08

The energy absorbing capacity and the ductility index reduced with the increase of fatigue cycles. The residual energy absorbing capacity and ductility index of the link slab at 1million fatigue cycle were 16.0 joules and 4.08, respectively - 83% and 89% , respectively lower than the non-fatigued specimen. The small residual energy absorbing capacity and ductility index were attained by the strain hardening characteristic of the steel rebar after excessive plastic

deformation during fatigue loading. These characteristics justified the failure of the link slab specimen subjected to 1 million fatigue cycle.

5.4 Summary

This chapter analyzed and discussed the fatigue performance of the link slab specimens at different stages of pre-fatigue, fatigue and post-fatigue by two different approaches of variable fatigue stress level and fatigue cycles. The ECC link slabs demonstrated a prolonged life in compare with SCC link slabs even though it was subjected to higher fatigue stress range (±20%). Among the ECC link slabs, the failure of specimens at 55%±20% stress level and 1 million fatigue cycle were justified through the fatigue and post fatigue responses.

CHAPTER SIX

CONCLUSIONS

6.1 General

This thesis described the structural performance of reduced scale link slabs subjected to monotonic and fatigue loading. Various concrete materials, including seven different types of engineered cementitious composite (ECC) mixtures and a control self-consolidating concrete (SCC) were used for analyzing their influence on flexural monotonic performance of $1/4^{th}$ scale model link slab specimens. The variables in the ECC mixtures included types of fly ash (Class CI or F), percentage of fly ash as cement replacement (55% and 70%) and types of sand (silica sand or local crushed sand). The variables in the fatigue loading included: stress levels (40%±20% to 55%±20% of peak load and number of cycles up to 1 million. All ECC link slabs showed superior performance in terms of ductility, crack width, crack propagation, and strain hardening behaviour compared with their SCC counterparts. In phase I (flexural performance study under monotonic loading), the mortar sand based ECC with 50% replacement of fly ash CI showed comparatively better performance in terms of higher ultimate strength, energy absorbing capacity and higher ductility index/bending capacity in compare with other ECC mixes. This green and cost-effective ECC mix was selected for the second and third phases of experimental investigation namely fatigue performance (Phase II) under cyclic loading and structural behaviour of a joint-free $1/6^{th}$ scale full bridge model with ECC link slab under static loading (Phase III). High fatigue stress levels (40%±20% and 55%±20% for ECC link slab and 40%±5% for SCC link slab) and cycles (ranging from 400000 to 1 million) were applied to link slab specimens to study effect of stress levels and fatigue cycles on deflection, stress, cracking and stiffness evolutions during fatigue testing as well post-fatigue residual strength, stiffness, ductility, energy absorbing capacity. The same ECC mix was used for the one sixth scale full bridge model (two adjacent simply supported span with connecting ECC link slab) subjected to static monotonic loading (up to service stage – 50% of the design load) to study load-displacement/moment-rotation response and stress development. The experimental results are compared with those obtained from existing theoretical models to verify critical design issues such as location of inflection points (in joint-free bridge deck with ECC link slab), strength of the link slab, support rotation.

6.2 Conclusions

The following conclusions are drawn from experimental and theoretical investigations on link slabs as well as joint-free bridge deck with link slab:

- All seven ECC mixtures have the minimum 28 days compressive strength of 45 MPa and flexural strength of 4.5 MPa which are considered to be adequate for bridge deck application.

- Link slabs with all seven types of ECC mixtures (Phase I-investigation) showed better performance in terms of higher ultimate strength (>8.79 kN), ductility (a ductility index >14.4), support end rotation (satisfying the allowable AASHTO's (2012) rotation of 0.00375 radian at 25% of ultimate load), smaller crack widths (<100μm), and high energy absorption capacity (> 81.6 Joules) in compare with SCC (normal concrete) link slab counterparts. ECC link slabs exhibited superior strain hardening behaviour over SCC link slab can be attributed due to the fiber bridging characteristics in the post-cracking stage. The brittle fracture of the SCC link slab showed no strain hardening capacity while causing high interfacial shear and subsequent steel concrete interfacial bond forces, leading to higher rebar strain development at lower load level. The rebar strain development for all ECC link slabs increased near the ultimate loading (at 85% of ultimate load), rather than first cracking load. All ECC link slab failed under ductile mode where brittle failure was governed for SCC link slab. This proved the fact that the functionality of original simply supported bridges with a continuous deck should be maintained due to high flexibility of ECC link slabs that will allow the adjacent girders to deform freely (in case of joint-free bridge deck), while the deck was restrained.

- ECC link slabs with crushed and mortar sand showed higher ultimate load and energy absorbing capacity compared to their silica sand counterparts. Link slabs with higher fly ash content developed lower ultimate load and energy absorbing capacity, but enhanced bending capacity/ductility. Overall, performance of all ECC based link slabs is comparable and satisfactory, but for maintaining the simply supporting action of the bridge girders in joint-free bridge deck construction, a superior ductility with lower

117

structural stiffness is required. The optimized ECC mix that offers the ductility, lower structural stiffness while economical is crushed/mortar sand based ones at higher (70%) fly ash content.

- Existing Code based/other theoretical specifications underestimated the flexural strength of ECC link slab while predicted strength of SCC link slabs was very close to those obtained from experiments. The existing design equations should be revised to predict reasonably the flexural strength of ECC link slabs.

- The mortar sand based ECC link slab (Phase II: investigation) showed good structural performance subjected to high fatigue stress level (maximum 60% and 75%), in compare with SCC link slab (45%). After intense fatigue stress level, the ultimate strength, rebar and concrete strain developments, ductility and energy absorbing capacity were reduced only by 20% of the non-fatigued specimen whereas the SCC link slab with lower fatigue stress level (maximum 45%) was reduced by 60% of its controlled specimen. While the PVA fibers were mainly responsible for resisting the high fatigue stress levels for the ECC link slabs, the steel rebar resisted the fatigue loading for the SCC link slab. Therefore, with low reinforcing ratio, the SCC link slab demonstrated a poor performance under fatigue loading. Although ECC link slab showed satisfactory fatigue performance, but the maximum fatigue stress level for the ECC link slab should be limited to 60% of its ultimate strength for acceptable ultimate, durability and serviceability limit state.

- At the constant fatigue stress level (maximum 60%), the ECC link slab was considered to have failed at 1million fatigue cycle. The ruptured PVA fibers at high fatigue cycle caused a ductile failure of the ECC link slab. The failure was confirmed with a low residual ultimate strength (75% lower than non-fatigued specimen), low ductility, energy absorbing capacity, large crack width formation (visible rupture fibers) with a fractured steel rebar. For satisfactory ultimate, durability and serviceability limit state, based on these investigation, the maximum fatigue cycle for the ECC link slab should be limited to 500000 fatigue cycles. However, it should be noted that frequency of fatigue load application was much higher in the experimental investigation.

- In Phase III, ECC link slab (with mortar sand and 50% fly ash CI content as used in Phase II) showed satisfactory structural performance in a reduced scale full bridge model at service load stage. The induced moment on the link slab due to applied loading only reached 10% of the ultimate strength capacity (of the ECC link slab). The experimental results with a minor difference (<10%) satisfied the theoretical deflection and support end rotations (as suggested by the existing Codes) for simply supporting bridge structure. The experimental results with less 16% difference also satisfied the existing Code based/ theoretical models for the location of the hinges (inflection points) in a joint free bridge decks with two simply supported adjacent spans connected with a link slab.

The study confirmed the viability of constructing link slabs using higher fly ash content and local crushed/mortar sand based ECCs for a cost-effective sustainable joint-free bridge decks with satisfactory structural performance under monotonic and fatigue loading.

6.3 Recommendations for Future Work

Further experimental and theoretical investigations with varying parameters such as debond zone length, reinforcing ratio, loading types (static and fatigue) and concrete types are to be conducted to understand the link slab behaviour and to develop guidelines/specifications for the design of link slab as well as joint-free bridges with link slab.. The following recommendations are suggested for further research studies:

- Additional fatigue tests are to be conducted on beam specimens with different ECC mixtures for comprehensive understanding of material properties and performance subjected to high fatigue stress level and cycles.

- Comprehensive fatigue tests are to be conducted r on link slabs using different green ECC mixtures to evaluate the performance under high fatigue stress level and cycles to develop design guidelines and to predict service life of link slabs.

- More investigations are to be conducted on joint-free bridge decks with ECC link slabs under fatigue loading to develop design guidelines for joint-free bridges for practical applications.

- Finite element (FE) modeling should be carried out based on experimental investigations. After verification of the FE model with experimental results, extensive numerical modelling with varying structural parameters such as reinforcing ratio, debond zone length, loading cases (monotonic, fatigue and creep) and concrete types is to be conducted for evaluating their influence on structural performance. Aftermath, additional experimental investigations are required for the verification of new numerical/analytical models.

- Field demonstration of green ECC link slab in a real bridge structure is required for complete evaluation of the link slab performance and development of defined design guidelines.

References

AASHTO. (2002). *Standard Specifications for Highway Bridges, 17th Edition*, Washington DC: AASHTO.

AASHTO. (2012). *AASHTO LRFD Bridge Design Specifications, 6th Edition*, Washington DC: AASHTO.

ACI Committee 215. (1992). Considerations for Design of Concrete Structures Subjected to Fatigue Loading (ACI 215R-92), American Concrete Institute, Detroit.

Alampalli, S. and Yannotti, A.P. (1998). In-service Performance of Integral Bridges and Joint less Decks. *Transportation Research Record;* 1624(98) pp. 1-7.

Alexander, M. G. Jaufeerally, H. and Mackechnie, J. R. (2003). Structural and Durability Properties of Concrete Made by Corex Slag. Research Monograph No. 6, Departments of Civil Engineering University of Cape Town, South Africa.

ASTM C39. (2003). Standard Test Method for Compressive Strength of Cylindrical Concrete Specimens. American Society for Testing and Materials, West Conshohocken, PA, USA.

ASTM C78/ C78M. (2010). Standard Test Method for Flexural Strength of Concrete (Using Simple Beam with Third-Point Loading), West Conshohocken, PA, USA.

ASTM C1018. (1997). ASTM C1018-97, Standard Test Method for Flexural Toughness and First-Crack Strength of Fiber-Reinforced Concrete (Using Beam With Third-Point Loading) (Withdrawn 2006), West Conshohocken, PA, USA.

ASTM C 618. (2012). Standard Specifications for Coal Fly Ash and Raw or Calcined Natural Pozzolan For Use In Concrete. American Society for Testing and Materials, West Conshohocken, PA, USA.

Au, A. Lam, C. Au, J. and Tharmabala, B. (2013). Eliminating Deck Joints Using Debonded Link Slab: Research and Field Test in Ontario. *Journal of Bridge Engineering*, 18(8), pp. 768-778.

Au, A. and Lam, C. (2009). Experimental Investigation of Link Slab Performance Using Scaled-Down Models. Ministry of Transportation Highway Standards Branch Report (Bro-041). Ontario Minitistry of Transportation. Ontario. Canada.

Bisaillon, A. Rivest, M. and Malhotra, V. (1994). Performance of High Volume Fly Ash Concrete in Large Experimental Monoliths. *ACI Materials Journal*, 91(2), pp. 178-187.

Caner, A. and Zia, P. (1998). Behavior and Design of Link Slabs with Jointless Bridge Deck. *PCI Journal*. pp. 68-80.

CHBDC. (2006). *Canadian Highway Bridge Design Code, 10th Edition*, Mississauga, Canadian Standard Association.

Chen, H. J. Liu, T. H. Tang, C. W. and Wen, P. T. (2011). Influence of High-Cycle Fatigue on the Tension Stiffening Behavior of Flexural Reinforced Lightweight Aggregate Concrete Beams. *Structural Engineering and Mechanics Journal*, 40(4), pp. 1-20.

CISC. (2010). *Handbook of Steel Construction, 10th edition*, Ontario, Canada: CISC.

Fischer, G. and Li, V.C. (2003). Intrinsic Response Control of Moment Resisting Frames Utilizing Advanced Composite Material and Structural Elements. *ACI Structural Journal,* 100(1), pp.166-176.

Gastal, F. and Zia, P. (1989), Analysis of Bridges Beams with Joint Less Decks, Proceedings of IASBE Symposium, Lisbon.

Gilani, A. (2001). Link slabs for Simply Supported Bridges Incorporating Engineered Cementitious Composites. MDOT SPR-54181. *Structural Research Unit, MDOT*, USA.

Giordano, L. and Mancini, G. (2009). Fatigue Behavior Simulation of Bridge Deck Repaired with Self Compacting Concrete. *Journal of Advanced Concrete Technology*, 7(3), pp. 415-424.

Hossain, K.M.A and Anwar, M.S. (2014). Strength and Deformation Characteristic of ECC Link Slab in Joint-Free Bridge Decks, Istanbul Bridge Conference, August, Istanbul, Turkey.

Hossain, K.M.A. and Sherir, M. (2014). Fracture Energy Characteristics of Engineered Cementitious Composites Incorporating Different Aggregates. CSCE 2014 4th International Structural Specialty Conference, Halifax, Canada.

Hussian, S. E. and Rasheeduzzafar, M. (1994). Corrosion Resistance Performance of Fly Ash Blended Cement Concrete. *ACI Materials Journal*, 91(3), pp. 264-272.

JCI-DFRCC Committee. (2003). DFRCC Terminology and Application Concepts. *Journal of Advanced Concrete Technology*, 1(3), pp. 335-340.

Kanda, T. and Li, V. C. (1998). Multiple Cracking Sequence and Saturation in Fiber Reinforced Cementitious Composites. *Concrete Research and Technology, JCI*, 9(2), pp. 19-33.

Karahan, O. Hossain, K.M.A. Ozbay, E. Lachemi, M. and Sancak, E. (2012). Effect of Metakaolin Content on the Properties Self-consolidating Lightweight Concrete. *Construction and Building Materials,* 31(6), pp. 320-325.

Keoleian, G. Kendall, A. Chandler, R. Helfand, G. Lepech, M. and Li, V.C. (2005). Life Cycle Model for Evaluating the Sustainability of Bridge Decks, *Proc. 4th International Workshop on Life Cycle Cost Analysis and Design of Civil Infrastructure Systems*, Florida, pp. 8-11.

Kim, Y.Y. Fischer, G. and Li, V.C. (2004). Performance of Bridge Deck Link Slabs Designed with Ductile ECC. *ACI Structural Journal*, 1(6), pp. 792-801.

Kosmatka, S. and Panarese, W. (1988). *Design and control of concrete mixtures.* 13th Edition. Skokie, IL: Portland Cement Association, 205.

Kuroda, M. Watanabe, T. and Terashi, N. (2000). Increase of Bond Strength at Interfacial Transition Zone by the Use of Fly Ash. *Cement and Concrete Research*, 30(2), pp. 253-258.

Lam, C. Lai, D. Au, J. Lim, L. Young, W. and Tharmabala, B. (2008). Development of Concrete Link Slabs to Eliminate Bridge Expansion Joints over Piers. Paper prepared for presentation at the Bridges - Links to a Sustainable Future (B) Session of the 2008 Annual Conference of the Transportation Association of Canada Toronto, Ontario.

Lepech, M. and Li, V. (2005b). Durability and Long Term Performance of Engineered Cementitious Composites. Honolulu, Hawaii, In Proceedings of International RILEM Workshop on HPFRCC in Structural Applications, pp. 165-174.

Lepech, M.D. and Li, V.C. (2006). Long Term Durability Performance of Engineered Cementitious Composites, *J Restor Build Monum*, 12(2), pp. 119-132.

Lepech, M.D. and Li, V.C. (2008). Large Scale Processing of Engineered Cementitious Composites, *ACI Material Journal*, 105(4), pp.358-366.

Lepech, M. D. and Li, V. C. (2009). Application of ECC for Bridge Deck Link Slabs. *RILEM* Journal of Materials and Structures, 42(9), pp. 1185-1195.

Li, V. C. (2011). High-Ductility Concrete for Resilient Infrastructures. *Journal of Advanced and High-Performance Materials*, pp. 16-21.

Li, V.C. Wang, S. and Wu, C. (2001). Tensile Strain-Hardening Behavior of Polyvinyl Alcohol Engineered Cementitious Composite (PVA-ECC). *ACI materials journal,* 98(6), pp. 483-492.

Li, V.C. Lepech, M.D. and Li, M. (2005). Field Demonstration of Durable Link Slabs for Jointless Bridge Decks Based on the Strain-Hardening Cementitious Composites, Michigan Department of Transportation Report No. RC-1471, pp. 1-147.

Li, V.C. Fischer, G. Kim, Y.Y. Lepech, M. Qian, S. Weimann, M. and Wang, S. (2003). Durable Link Slabs For Jointless Bridge Decks Based on Strain-Hardening Cementitious Composites, Report for Michigan Department of Transportation RC- 1438.

Li, V.C. (1993). From Micromechanics to Structural Engineering-The Design of Cementitious Composites for Civil Engineering Applications, JSCE J of Structural Mechanics and Earthquake Engineering, 10(2), pp.37-48.

Li, V. Mishra, D. and Wu, H. (1995). Matrix Design for Pseudo Strain-Hardening Fiber Reinforced Cementitious Composites. *RILEM Journal of Materials and Structures*, 28(183), pp. 586-595.

Li, V. C. Wang, S. Ogawa, A. and Saito, T. (2002). Interface tailoring for strain-hardening PVA-ECC. *ACI Materials Journal*; 99(5), pp. 463–472.

Li, V.C. (1998). ECC Tailored Composites through Micromechanical Modeling. Fiber Reinforced Concrete: Present and the Future Edited by Banthia et al., CSCE. Montreal, pp. 64-97.

Li, V.C. and Kanda, T. (1998). Engineered cementitious composites for structural applications. *Journal of Materials in Civil Engineering.* 10(2), pp. 66-69.

Li, V.C. (2003). Engineered cementitious composites (ECC) - A review of the material and its Applications. *Journal of Advanced Concrete Technology,* 1(3), pp. 215–230.

Lin, Z. Kanda, T. and Li, V. C. (1999). On Interface Property Characterization and Performance of Fiber Reinforced Cementitious Composites. Concrete Science and Engineering, RILEM, 1, 173-184.

Matsumoto, T. (1998). Fracture Mechanics Approach to Fatigue Life of Discontinuous Fiber Reinforced Composites. PhD thesis, Dept. of Civil and Environmental Engineering, University of Michigan, Ann Arbor, Michigan, pp. 274.

Maulin, B.M. (2012), *Fresh/Mechanical/Durability Properties and Structural Performance of Engineered Cementitious Composite (ECC).* Published master's thesis, Ryerson University, Toronto Canada.

Mehta, P. K. and Monteiro, P. J. M. (2006). *Concrete: Structure, Properties, and Materials*, Third Edition, New York, McGraw Hill.

Mindess, S. Young, J.F. and Darwin, D. (2003). *Concrete.* 2nd Edition, Pearson Education, Inc.

Nawy, E. (2008). *Concrete Construction and Engineering Handbook*, Second Edition, New York, CRC Press.

Neville, A.M. (2002). *Properties of Concrete.* Fourth and Final Edition, John Wiley & Sons, New York, pp. 884.

Özbay, E. Karahan, O. Lachemi, M. Hossain, K. M. A. and Atis C. D. (2013). Dual Effectiveness of Freezing–Thawing and Sulfate Attack on High-Volume Slag-Incorporated ECC. Composites Part B: Engineering, 45(1), pp. 1384-1390.

Özbay, E. Karahan, O. Lachemi, M. Hossain, K.M.A. and Atis, C.D. (2012). Investigation of Properties of Engineered Cementitious Composites Incorporating High Volumes of Fly Ash and Metakaolin. *ACI materials journal,* 109(5), pp. 565-571.

Peled, A. and Shah, P. S. (2003). Processing Effect in Cementitious Composites: Extrusion and Casting, *Journal of Materials in Civil Engineering*. 15(2), pp. 192-199.

Qian, S. Lepech, M.D. Kim, Y.Y. and Li, V.C. (2009). Introduction of Transition Zone Design for Bridge Deck Link Slabs Using Ductile Concrete. *ACI structural journal*, 106(1), pp. 96-105.

Ranade, R. Zhang, J. Lynch, J. P. and Li, V. C. (2014). Influence of Micro-Cracking on the Composite Resistivity of Engineered Cementitious Composites. *Cement and Concrete Research*, 58(1), pp. 1-12.

Sahmaran, M. Yaman, I.and Tokyay, M. (2008). Transport and Mechanical Properties of Self-Consolidating Concrete with High Volume Fly Ash. *Cement and Concrete Composites,* 31(2), pp. 99-106.

Sahmaran, M. Lachemi, M. Hossain, K. M.A. and Li, V.C. (2009). Influence of Aggregate Type and Size on Ductility and Mechanical Properties of Engineered Cementitious Composites. *ACI Material Journal*, 106(3), pp. 308-316.

Sahmaran, M. Lachemi, M. Hossain K. M.A. Ranade, R. and Li, V.C. (2010). Internal Curing of ECC's for Prevention of Early Age Autogenous Shrinkage Cracking. *Cement and Concrete Research,* 39(10), pp. 893-901

Sherir, M. (2012), *Fracture Energy, Fatigue and Creep Properties of Engineered Cementitious Composites Incorporating Fly Ash/ Slag With Different Aggregates.* Published master's thesis, Ryerson University, Toronto Canada.

Suthiwarapirak, P. Matsumoto, T. and Kanda, T. (2004). Multiple Cracking and Fiber Bridging Characteristic of Engineered Cementitious Composites under Fatigue Flexure. *Journal of Material in Civil Engineering,* 16(5), pp. 433-443.

Wang, S. and Li, V.C. (2003). Tailoring of PVA Fiber/Matrix Interface for Engineered Cementitious Composite (ECC). (Plenary Lecture), Proceeding Fiber Society 2003 Symposium in Advanced Flexible Materials and Structures: Engineering with Fiber, Loughborough, UK, pp.91-92.

Wang, S. and Li, V. C. (2007). Engineered Cementitious Composites with High-Volume Fly Ash. *ACI materials journal*, 104(3), pp. 233-241.

Wang, H. and Belarbi, A. (2011). Ductility Characteristics of Fiber-Reinforced-Concrete Beams Reinforced with FRP Rebars. *Construction and Building Material Journal,* 25(5), pp. 2391-2401.

Weimann, M.B. and Li, V. C. (2003). Hygral Behavior of Engineered Cementitious Composites (ECC). *International Journal for Restoration of Buildings and Monuments*, 9(5), pp. 513-534.

Yang, E. Yang, Y. and Li, V.C. (2007). Use of High Volumes of Fly Ash to Improve ECC Mechanical Properties and Material Greenness. *ACI Materials Journal*, (104-M68), pp.303–311.

Zanuy, C. Maya, L.F. Albajar, L. and Fuente, P.D. (2011). Transverse Fatigue Behavior of Lightly Reinforced Concrete Bridge Decks. *Journal of Engineering Structure*, 33(10), pp. 2839-2849.

Zhang, J. and Li, V. C. (2002). Monotonic and Fatigue Performance in Bending of Fiber Reinforced Engineered Cementitious Composite In Overlay System. *Cement and Concrete Research*, 32, pp. 415-423.

Zia, P. Caner, A. and El-Safte, A. (1995) Jointless bridge decks research project 23241-94-4. *Center for Transportation Engineering Studies*, North Carolina State, pp. 1-117.

Zuk, W. (1981). "Joint less Bridges", Research Report No. FHWA/VA-81/48, Virginia Highway and Transportation Research Council. Charlottesville, Virginia, USA.

Appendix A

Resisting Moment Capacity for 1/4th Scale ECC Link Slab

The moment capacity for the 1/4th scale link slabs is designed in accordance to existing guidelines proposed by Caner & Zia (1998) and Lepech & Li (2009). The reinforcing ratio for the link slab is selected to satisfy the stress criterion ($f_s<0.4f_y$) at an imposed end rotation of 0.0015 radian. This is the expected end rotation angle derived by Caner and Zia (1998). The applied/induced moment in the link slab is calculated by Equation 2.6.

$$M_{ls} = \frac{2E_{ECC}I_{ls}}{L_{dz}}\theta$$

$$M_{ls} = \frac{2*18*1000*3.15*10^6*0.0015}{330} = 0.515 \text{ kN.m}$$

where E_{ECC} is the modulus of elasticity of the ECC, θ is the imposed end rotation angle and I_{ls} represents the uncracked moment of inertia as per Equation 2.7

$$I_{ls} = \frac{B_{ls}t^3}{12}$$

$$I_{ls} = \frac{(175)(60)^3}{12} = 3.15*10^6 \text{ mm}^4$$

where B_{ls} and t denotes the width and thickness of the link slab, respectively.

The use of uncracked moment of inertia results as a higher applied moment in the link slab (as it is evidenced from Equation 2.6). The higher calculation of induced/applied moment introduces additional conservisim and safety for the link slab design, since ECC link slab is intended to function in the micro-crack state (with lower moment of inertia) rather than uncracked state. Iterative design procedure (adopted by Lepech & Li (2009)) is used to determine the adequate reinforcing ratio, starting with the minimum steel ratio (ρ = 1.1 % as per AASHTO (2012) code). Through the analysis, the selected reinforcing ratio is adjusted accordingly to resist the applied moment imposed by the girders end-rotation.

A non-linear sectional analysis is considered (based on the assumption that ECC material remains perfectly elastic-plastic in service) for calculating the resisting moment capacity of the ECC link slab. For safe and conservative design, the strain hardening characteristic of the ECC material is neglected after the first cracking. Therefore the design yield strain and stress of 0.02% and 3.45 MPa respectively was selected for the ECC material (Lepech & Li, 2009).

For calculating the resisting moment capacity, the location of the neutral axis of the section is determined through the forces of equilibrium (Equations 2.10 to 2.13 and Figure A.1). Prior to calculating the neutral axis, the location of the stress 'kink' (n) in the tension region of the section is determined (based on Equation 2.9) due to the elastic-plastic tensile response of ECC material.

$$n = \frac{\varepsilon_{y-ECC}}{0.4\ \varepsilon_{y-Steel}}$$

$$n = \frac{0.02\%}{0.4\ (0.002)} = 0.25$$

where n represents the yield strain ratio, ε_{y-ECC} and $\varepsilon_{y-Steel}$ denote the yield strain of the elastic-plastic behaviour of ECC and steel reinforcement, respectively.
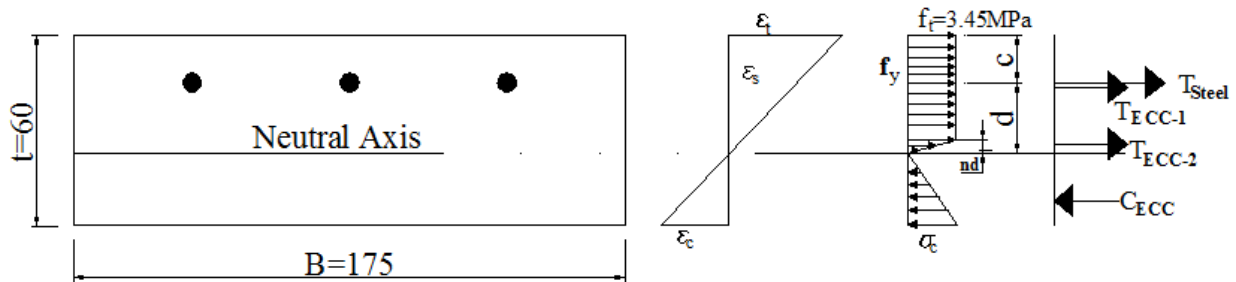

Figure A.1: Stress and Strain Distribution in the ECC Link Slab Cross Section

130

$T_{steel}=(0.4f_{y-steel})As$

$T_{steel}=(0.4(375))\ (3*28.27) = 12.72$ kN

$T_{ECC-1}= f_t\ [(1-n)d+c]b$

$T_{ECC-1}= 3.45[(1-.25)d+20]*175$

$T_{ECC-1} =\ \ 452.8d+12075$

$T_{ECC-2}= 0.5f_t\ ndb$

$T_{ECC-2}= 0.5*3.45*.25*d*175$

$T_{ECC-2}=75.47d$

$C_{ECC}=0.5\ f_t\ (\frac{1}{nd})(t_s-d-c)^2b$

$C_{ECC}=0.5 *3.45\ (\frac{1}{0.25d})(60-d-20)^2 *175$

$C_{ECC} =1932000/d\ -96600+1207.5d$

The location of the neutral axis for the section based on the equilibrium of the forces is determined as per Equation 2.14.

$T_{steel} +T_{ECC1}+T_{ECC2}= C_{ECC}$

$679.2d^2-121395d+1932000=0$

$d=17.65$ mm

After substituting d=17.56 mm back into the (Equations 2.10-2.13), the tensile and compressive forces are equal to:

$T_{steel}= 12.72$ kN

$T_{ECC-1}= 20.06$ kN

$T_{ECC-2}= 1.33$ kN

$C_{ECC}=34.17$ kN

The resisting moment capacity, $M_{r\text{-}ls}$ is calculated by summing the contribution of all forces about the neutral axis as per Equation 2.15 (for provided steel reinforcement ratio of $\rho=0.011$).

$$M_{r-ls} = \left\{ T_{Steel}d + T_{ECC-1}\left(\frac{(1-n)d+c}{2} + nd \right) + T_{ECC-2}\left(\frac{2}{3}\right)nd + C_{ECC}\left(\frac{2}{3}\right)(t_s - d - c) \right\}\left(\frac{1}{1000}\right)$$

$$M_{r-ls} = \left\{ 12.72 * 17.65 + 20.06\left(\frac{(1-0.25)17.65+20}{2} + 0.25*17.65 \right) + 1.33*0.25*17.65 \right.$$

$$\left. + 34.17\left(\frac{2}{3}\right)(60 - 17.65 - 20) \right\}\left(\frac{1}{1000}\right)$$

$$M_{r-ls} = 1.294 \; kN.m$$

M_{r-ls} > $M_{applied}$

The steel reinforcing ratio of $\rho=0.011$ is adequate for resisting the applied/induced moment on the link slab. With the finalized reinforcing ratio, the adequate spacing of the longitudinal rebar is determined by Equation 2.16.

$$S = \frac{A_{bar}}{\rho t_s}$$

$$S = \frac{26.27}{(0.011*60)}$$

S~50 mm

Resisting Moment Capacity for 1/6th Scale Full Bridge Model

The resisting positive moment for the 1/6th scale full bridge model is designed to resist the applied/induced moment at the service load stage for the imposed end rotation of 0.00375 radian (AASHTO, 2012). For validating the simply supporting performance of the girders, the bridge is considered as two simple spans SCC sections, connected by ECC link slab. Due to the symmetry, only one of the SCC spans is considered for determining the resisting positive moment capacity.

The applied load and moment for the SCC simple span composite section is determined based on Equation A1.

$$\theta = \frac{PL^2}{16\ EI}$$
A1

$$0.00375 = \frac{P(1000)^2}{16\ (200000)(0.65x10^7)}$$

P= 75 kN

M$_{Applied}$= 19 kN.m

where P denotes the applied load, E, I and θ symbolize the transformed section modulus of elasticity (considering steel girders modulus), transformed moment of inertia (for transformed steel section) and girders support end rotation respectively.

The SCC composite section is designed to resist the applied moment of 19 kN.m. Prior to calculating the moment capacity for one of the SCC spans the equilibrium of forces is used to locate the plastic neutral axis of the SCC composite section. The location of the plastic neutral axis is determined using Equations A2 to A7 (through iterative calculation). Initially the location of neutral axis is assumed to be within the concrete deck slab. Figure A.2 presents the resisting forces across the depth of the SCC section, assuming that plastic neutral axis is located within the concrete deck slab.
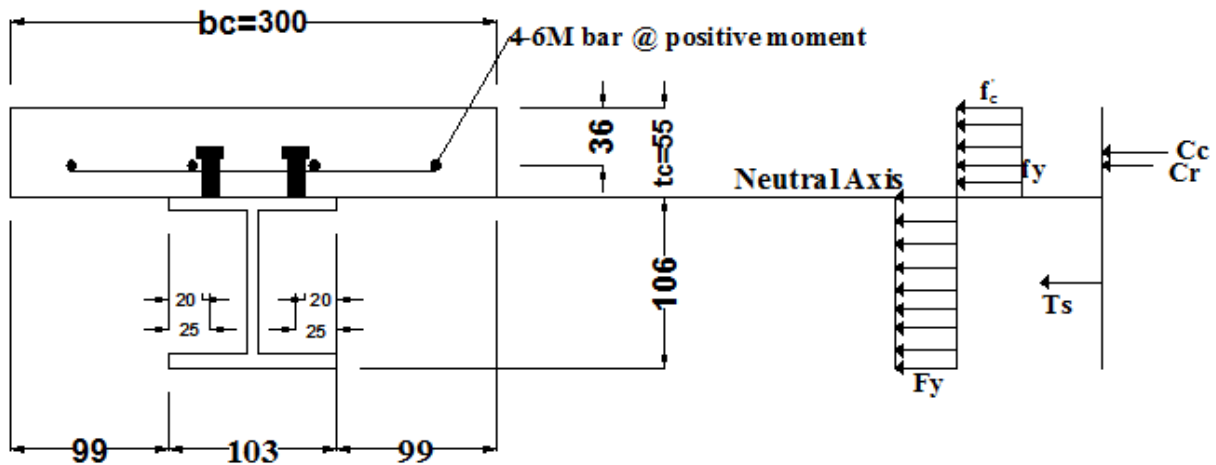
Figure A.2: Resisting Forces along the Depth of the SCC Section

$C_c = 0.85 b_e t_c f'_c$ A2

$C_c = 0.85 (300)(55)(36.4)$

$C_c = 510.5$ kN

where C_c denotes the concrete resisting compressive force (kN), b_e, t_c, f_c are representing width, thickness and compressive strength of concrete deck slab.

$C_r = A_r f_y$ A3

$C_r = (113.08)(375)$

$C_r = 45.2$ kN

where C_r designates the resisting compressive force for the steel rebar, A_r denotes the total area of steel rebar and f_y symbolizes the yielding strength of the steel reinforcement.

$T_s = A_s F_y$ A4

$T_s = (2480)(350)$

$T_s = 868$ kN

where T_s, A_s and F_y denotes the resisting tensile force, area and yield strength of the steel girder.

Based on the equilibrium of the forces ($C_c+C_r<T_s$) it is proven that plastic neutral axis is located within the steel girders top flange (as it is illustrated in Figure A.3). The residual compressive force for the steel girders top flange is calculated per Equation A5.

$C_s=0.5(A_sF_y-C_c-C_r)$ A5

$C_s=0.5[(2480(350)-510510-45200]$

$C_s= 156.5$ kN

where C_s denotes the resisting compressive force for the steel girder and A_s, F_y symbolize the area of the steel and yielding strength of the steel girder, W100x19.
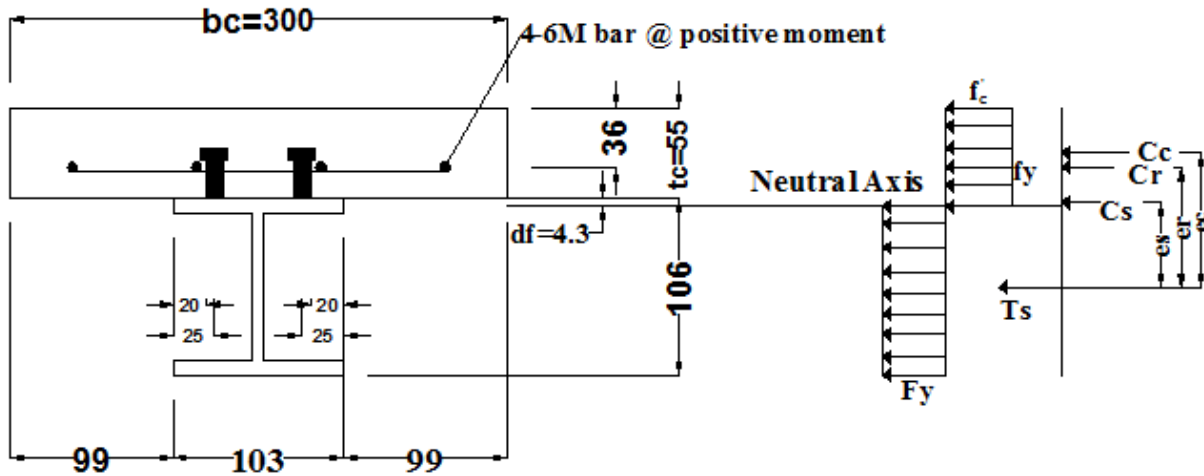

Figure A.3: Resisting Forces along the Depth of the SCC Section for Location of Plastic Neutral Within Steel Girder

Since the plastic neutral axis is located within the steel girder, the resisting tensile force for the steel girder is reduced further for maintaining the equilibrium of forces. The residual tensile force of the steel girder (W100x19) is calculated per Equation A6.

135

$T_s = A_s F_y - C_s$ A6

$T_s = (2480)(350) - 156500$

$T_s = 711.5$ kN

The location/total depth of the compressive force (d_f) for the steel girder is calculated per Equation A7 and illustrated in Figure A.3 by considering the resisting compressive force of the steel girder (C_s).

$C_s = b_f d_f F_y$ A7

$156500 = (103)(d_f)(350)$

$d_f = 4.34$ mm

The plastic neutral axis (as illustrated by Figure A.3) is located within the steel's girder top flange since d_f is less than the thickness of the steel girders flange (4.34 <9.89 mm)

The resisting positive moment for the composite SCC section is determined based on the contributions of the forces about the tensile force in the steel girder T_s (Figure A.3). The resisting moment capacity is determined based on Equation A8.

$M_r = C_c e_c + C_r e_r + C_s e_s$ A8

$M_r = (510.5)(0.161 - 0.0437 - 0.055/2) + (42.41)(0.161 - 0.0437 - 0.036) + (132.3)(0.106 - 0.00434/2 - 0.0437)$

$M_r = 57$ kN.m

where M_r denotes the resisting moment capacity and e_c, e_r, e_s denotes the distance from the resisting tensile force T_s to the concrete, rebar and steel girders compressive forces (Figure A.2).

The resisting moment capacity for the SCC composite section is satisfying the applied moment at the imposed end rotation of 0.00375 radian, since $M_r > M_{Applied}$.

The same procedure adopted in APPENDIX A for Resisting Moment capacity of the $1/4^{th}$ Scale ECC Link Slab is used to determine the resisting moment capacity for the ECC link slab of the $1/6^{th}$ scale full bridge model with a small modification. The applied moment in the ECC link slab for the $1/6^{th}$ scale full bridge model is considered at imposed serviceable end rotation of 0.00375 radian. Using Equation 2.6, the applied moment in the ECC link slab for imposed end rotation of 0.00375 radian is 2.3 kN.m. The resisting moment capacity for the ECC link slab (Equation 2.15) is 2.89 kN.m.